Electronic and Physical Characterization of Hydrothermally Grown Single Crystal ThO_2

DISSERTATION

Tony D. Kelly II, Air Force Civilian, USA

AFIT-ENP-DS-13-D-02

DEPARTMENT OF THE AIR FORCE
AIR UNIVERSITY

AIR FORCE INSTITUTE OF TECHNOLOGY

Wright-Patterson Air Force Base, Ohio

AFIT-ENP-DS-13-D-02

ELECTRONIC AND PHYSICAL CHARACTERIZATION OF HYDROTHERMALLY GROWN SINGLE CRYSTAL THO_2

DISSERTATION

Presented to the Faculty

Graduate School of Engineering and Management

Air Force Institute of Technology

Air University

Air Education and Training Command

in Partial Fulfillment of the Requirements for the

Degree of Doctor of Philosophy

Tony D. Kelly II, BS, MS

Air Force Civilian, USA

December 2013

AFIT-ENP-DS-13-D-02

ELECTRONIC AND PHYSICAL CHARACTERIZATION OF HYDROTHERMALLY GROWN SINGLE CRYSTAL THO_2

Tony D. Kelly II, BS, MS
Air Force Civilian, USA

Approved:

//signed//	December 2013
James C. Petrosky, Ph.D. Dissertation Advisor	Date
//signed//	December 2013
John W. McClory, Ph.D. Committee Member	Date
//signed//	December 2013
Robert L. Hengehold, Ph.D. Committee Member	Date
//signed//	December 2013
Larry W. Burggraf, Ph.D. Committee Member	Date
//signed//	December 2013
William P. Baker, Ph.D. Committee Member	Date

Accepted:

//signed//	December 2013
Adedeji B. Badiru, Ph.D. Dean, Graduate School of Engineering and Management	Date

AFIT-ENP-DS-13-D-02

Abstract

This dissertation focused on extracting the geometric and electronic structure of hydrothermally synthesized ThO_2 single crystals. Not only do these results allow for future crystal growth to be pursued in an informed and purposeful direction, but they provide insight into the nature of ThO_2 in single crystal form and the manner in which the properties differ when compared to the other forms found in literature (powders, colloids, etc).

The valence and conduction bands were studied with ultraviolet photoemission, inverse photoemission, and x-ray absorption near edge structure in order to ascertain the band gap and investigate the $5f$ band behavior. The experimental techniques were compared to the results of real space Green's function calculations.

Long range order was measured with x-ray diffraction and compared to the local order structure from extended x-ray absorption fine structure. The average fluorite structure was confirmed and an O-shell splitting was analyzed. In order to remove experimenter bias from the extended x-ray absorption fine structure analysis, a Latin hypercube sampling code was written. This software increased both speed and efficiency in searching for local minima in the parameters' space as well as selecting out the true minimum.

A depth resolved x-ray photoemission experiment extracted shake-up satellites representative of additional final states. The results provided information concerning the valence and conduction bands. A surface to core-level shift was observed. Two new satellites were discovered and their results interpreted. Finally, a Debye temperature coefficient was extracted for the crystals using the Th $4f$ core levels.

To my parents

Acknowledgements

An extensive number of people and organizations were essential to this research's successful completion. First, this research was financially supported by the Defense Threat Reduction Agency. Without their support, none of this would have been possible.

It was my privilege to work with scientists and researchers at the Center for Advanced Microstructures and Devices and at the University of Nebraska-Lincoln. In particular, the many conversations with Dr. Dowben have been insightful and always full of lessons within lessons. His insights are and were akin to surface-core level shifts for often times they revealed information beyond the surface of the conversations. As a mentor, Dr. Dowben has influenced my own final state condition in research, so that I now find myself looking for those strange peaks that pop up in the data. As I once told him, he makes science sound like poetry.

Next, I want to acknowledge and thank my research committee for bringing all their expertise to bear upon my research topic. My external committee member, Dr. Baker brought fresh insight from a fundamental mathematics perspective. His comments and suggestions have always forced me to push myself further and deeper beyond what many texts and journal articles have addressed. With his expertise in electronic structure and solid state materials, Dr. Hengehold has been of immense importance in critiquing my analyses and conclusions. Dr. Burggraf with his vast knowledge of not only chemical processes but of actinide behavior overall has been able to look upon my own research and cut as a knife, straight to the heart of my actinide problems and has spurred fruitful and insightful discussions. Dr. McClory has been absolutely essential in forcing me to reach the lofty tasks that were set before me. Often, he would see immediately any topics I would attempt to avoid and force me to address them. His guidance both in my research and my ability to

communicate my research was essential to the conclusion of this work.

Words are difficult to come by in order to thank my research advisor, Dr. Petrosky. Dr. Petrosky has been both a mentor in my research work and in my life in general. Ever since I arrived at AFIT to interview for my research position, his farseeing ability has astounded me. I will miss the conversations which stemmed anywhere from horses and farm life to renewable energy sources and grand inventions. I hope I too am able to retain the vigor and insight that Dr. Petrosky has shown me in pursuing both my own life goals and research objectives.

Lastly, I would like to thank my parents and family for their unwavering belief and support. It has been a grand adventure. One I would not have been able to pursue without the many sacrifices made for me so that I might make it this far.

Tony D. Kelly II

Table of Contents

Page

Page

List of Figures

Figure Page

List of Tables

List of Abbreviations

Abbreviation		Page
AFRL	Air Force Research Laboratory	3
AFIT	Air Force Institute of Technology	3
CU	Clemson University	3
Ln	lanthanides	4
An	actinides	4
FCC	face-centered cubic	8
BCC	body-centered cubic	8
PES	photoemission spectroscopy	13
XPS	x-ray photoemission spectroscopy	13
UPS	ultraviolet photoemission spectroscopy	13
IPES	inverse photoemission spectroscopy	13
XANES	x-ray aborption near edge structure	13
EXAFS	extended x-ray absorption fine fine structure	13
XAFS	X-ray absorption fine structure	35
BNL	Brookhaven National Laboratories	39
VBM	valence band maximum	51
XRD	x-ray diffraction	52
LEED	low energy electron diffraction	52
DOS	density of states	52
GM	Geiger-Müller	52
UHV	ultrahigh vacuum	53
AVS	American Vacuum Society	54

Abbreviation Page

BIS Bremsstrahlung isochromat spectroscopy 56

CAMD Center for Advanced Microstructures and Devices 57

WDCM wiggler double crystal monochromator 57

DCM double crystal monochromator 57

DFT density functional theory 58

HWHM half-width at half-maximum 62

FWHM full width at half-maximum 74

List of Symbols

Symbol		Page
m_0	Rest mass	7
H	Hamiltonian	13
$U(\vec{r})$	Periodic atomic potential	13
E	Energy or eigenenergy	13
Ψ	State wavefunction	13
$\vec{k}$	Wave vector	13
E_{kin}	Kinetic energy	15
$\hbar\omega$	Photon energy	15
E_B	Electronic binding energy	15
$\vec{E}(\vec{r},t)$	Electric field	16
$\vec{B}(\vec{r},t)$	Magnetic field	16
$\vec{A}$	Vector potential	16
H_I	Perturbing Hamiltonian	16
I_{PES}	Photoelectric current	16
$\vec{p}$	Momentum operator	16
M_{fi}	Transition matrix	17
E_F	Fermi energy	19
$k_{\|\|}$	Parallel component of electron momentum	20
$k_\perp$	Perpendicular electron momentum	20
$\mathrm{V}_{\mathrm{interface}}$	Interface potential	20
$\chi(k)$	Extended x-ray absorption fine structure	28
S_0^2	Amplitude reduction factor	28

Symbol Page

Symbol Page

ELECTRONIC AND PHYSICAL CHARACTERIZATION OF HYDROTHERMALLY GROWN SINGLE CRYSTAL ThO_2

I. Introduction

1.1 Overview

The ultimate goal for this dissertation research is to measure the geometric and electronic characteristics of hydrothermally synthesized ThO_2. The project's desired outcome is an understanding of the techniques required to fabricate uranium (U_xO_y) semiconductors. The difficulty in growing large, pure, single crystals of U_xO_y is partly due to the very rapid oxidation of uranium oxide surfaces. The $5f$ electron activity within U compounds allows for the rapid formation of solid solutions, occurring within minutes under atmospheric conditions [1]. These hyperstoichiometric conditions generally evolve at a rate faster than the growth techniques used to synthesize the crystals.

One particularly favored form of U_xO_y is UO_2. UO_2 adopts the fluorite structure (space group $Fm\bar{3}m$) and is often used in nuclear fuel pellets, being ideal for retaining fission products [3]. However, the fluorite structure easily forms crystalline defects. In the case of UO_2, O atoms tend to occupy octahedral interstitial sites and result in UO_{2+x} [4]. The ease with which U_xO_y forms these solid solutions may be demonstrated by a phase diagram. In Figure 1, an U-O binary phase diagram is reconstructed with data from [2]. What is significant are the many regions where UO_2, U_3O_8, and UO_3 strictly do not exist. Instead, overlapping regions persist and form solid solutions.

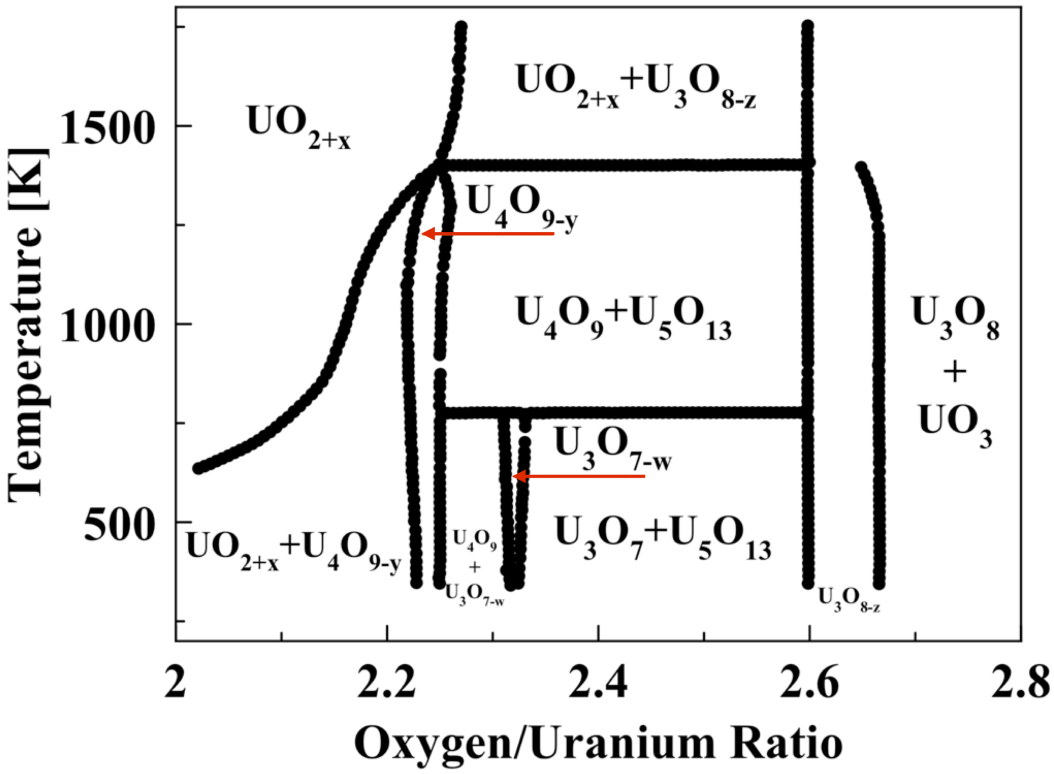

Figure 1. Binary phase diagram for U_xO_y from O_2 to $O_{2.72}$. The data has been obtained from [2] with permission.

Barring any appreciable phase changes, these shifts in stoichiometry are not a major problem for nuclear fuel. However, the U_xO_y oxidation and stoichiometry do influence important device characteristics such as conductivity (Figure 2). Changes in these electronic and geometric structures will have a profound influence on any semiconductor's properties. Thus, a means of obtaining large, single crystals of UO_2 needs to be established in order to determine baseline device characteristics and to perform parameterization experiments.

Recently, the hydrothermal growth technique has been applied to growing refractory oxide single crystals [6,7]. While this growth technique is not new, the application to synthesizing actinide single crystals is novel. In particular, ThO_2 single crystals are obtainable. This growth technique has been moved to the Air Force Research

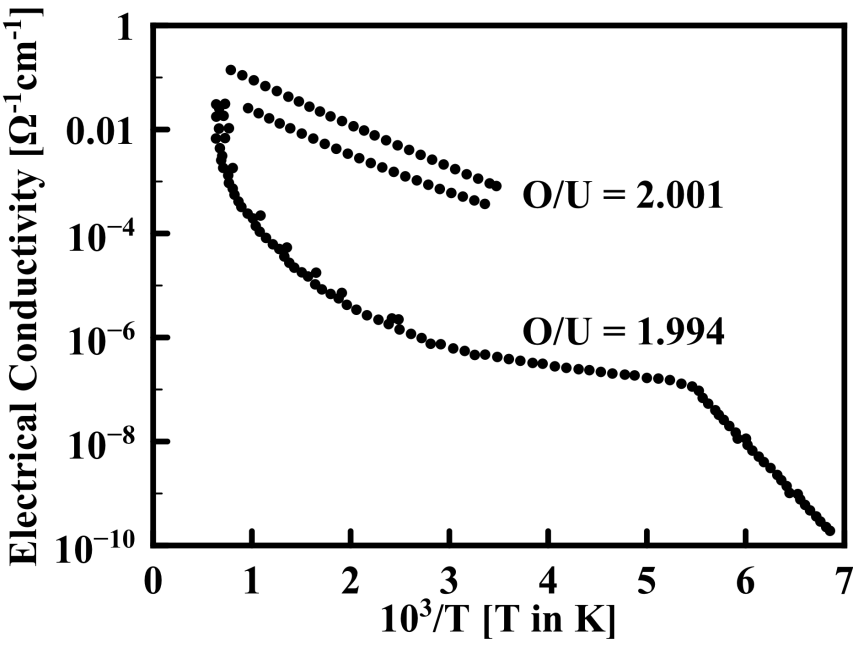

Figure 2. U_xO_y conductivity for O/U = 2.001 and 1.994. The data has been obtained from [5], open access.

Laboratory (AFRL) in a collaborative research focus established with the Air Force Institute of Technology (AFIT). Samples of the original ThO_2 single crystals grown at Clemson University (CU) have been obtained for this dissertation. The single crystals were studied for their intrinsic properties, acknowledging extrinsic characteristics (impurities, defects, etc) as they appear in the data.

Of utmost importance is the local geometric structure and the valence/conduction band structure. Knowledge of the local geometric structure is essential to understanding how U dopants will modify the coordinating O and Th environment. Whereas, knowledge of the electronic structure is necessary for extracting the band gap and identifying the role of defects which influence the electronic properties. These studies on hydrothermally grown ThO_2 single crystals lay a foundation for understanding U:ThO_2 alloy and UO_2 crystalline properties, including the source of differences that appear in the structures.

While the ultimate motivation is fabrication of U_xO_y electronic devices, understanding the geometric and electronic characteristics of ThO_2 plays an important role in laying the basis for UO_2 studies that are crucial in establishing material characteristics for civilian and military applications. The research importance includes: continued development of smaller integrated circuits, design of radiation hardened electronics, advancement of nuclear fuel design, management of nuclear waste production, reduction of the depleted uranium stockpile, increased understanding of actinide metal aging, and development of next generation neutron detectors [5, 8–10].

1.2 Lanthanides and Actinides

This research determines ThO_2's single crystalline geometric and electronic structure. In particular, electronic properties are examined, with a focus on the central theme of f-orbital electrons. It is demonstrated that the difficulty in understanding the actinide compounds revolves around the f-orbitals' behavior. The lanthanides (Ln) and the actinides (An) are characterized by the filling of f-shell electronic orbitals. With respect to the ground state configuration, the Ln form $4f^x5d^y$ and the An form $5f^x6d^y7s^2$. The extent to which the Ln and An are comparable depends upon the manner in which the $4f$ and $5f$ electrons behave. Some features are similar (e.g. orbital contraction), while others are distinctive between the two series (e.g. chemical valence), resulting in different chemical and physical properties [11].

The Ln will be briefly discussed, giving insight into the electronic orbital structure. The Ln possess unusual uniformity across the series. This uniformity is not a remark that all Ln behave identically, but a statement of how unusually similar they are compared to the previous d-filling transition metal series. After the Ln, the An will be discussed, demonstrating their deviation from the Ln norm.

Edited and reproduced from [12], Figure 3 lists the Ln elements' ground and

Ln	Z	Ground	+2	+3	+4
La	57	$6s^2 5d^1$		Xe	
Ce	58	$4f^1 6s^2 5d^1$		$4f^1$	Xe
Pr	59	$4f^3 6s^2$		$4f^2$	$4f^1$
Nd	60	$4f^4 6s^2$	$4f^4$	$4f^3$	$4f^2$
Pm	61	$4f^5 6s^2$		$4f^4$	
Sm	62	$4f^6 6s^2$	$4f^6$	$4f^5$	
Eu	63	$4f^7 6s^2$	$4f^7$	$4f^6$	
Gd	64	$4f^7 6s^2 5d^1$		$4f^7$	
Tb	65	$4f^9 6s^2$		$4f^8$	$4f^7$
Dy	66	$4f^{10} 6s^2$	$4f^{10}$	$4f^9$	$4f^8$
Ho	67	$4f^{11} 6s^2$		$4f^{10}$	
Er	68	$4f^{12} 6s^2$		$4f^{11}$	
Tm	69	$4f^{13} 6s^2$	$4f^{13}$	$4f^{12}$	
Yb	70	$4f^{14} 6s^2$	$4f^{14}$	$4f^{13}$	
Lu	71	$4f^{14} 6s^2 5d^1$		$4f^{14}$	

Figure 3. Tabulated electronic states for Ln atoms.

valence configurations. From the figure, it may be deduced that the +3 valence state is the most stable across the series. With increasing atomic number, the $4f$ electrons contract and become more stable than the $6s$ electrons [11, 12]. This results in the $4f$ electrons being in a lower energy configuration than the $5d$ and $6s$ electrons. Particularly, the outer electrons become destabilized, while the $4f$ electrons remain tightly bound [11, 12].

The $4f$ radial probability distribution for the Ln valence shells [12,13] is influenced by orbital contraction. The tightly bound $4f$ electronic radial function overlaps into the closed Xe shell. Of additional note is the emergence of the $5d$ shell at three key points: an empty f-shell, a half filled f-shell, and a fully filled f-shell. In these situations, the electronic energy is not enough to place the $4f$ orbital below the $5d$ [12], lending particular stability to these configurations and to stable valencies other than

+3 (e.g. Ce^{+4} and Eu^{+2} in Figure 3).

Due to the contraction of the $4f$-orbitals, they do not usually participate in bonding. Consequently, the orbitals do not experience significant crystal field splitting when forming compounds. Thus, the expected electronic and magnetic spectra of the $4f$ electrons are not overly influenced by the coordinating environments. The Ln further differ from the transition metals and some actinides due to their lack of π-bond hybridization, as the $4f$ electrons remain inert, ruling out many O- and N-bonding situations [12].

In contrast with the Ln, nearly all An are man-made except the first few (Ac, Th, Pa, and U). While the Ln are mostly uniform with the filling of the $4f$ orbitals, the An series is roughly divided into two groups. The early An have transition metal-like behavior with the filling of the $5f$ orbitals and a variety of accessible valence states. The later An (Bk and higher) are noted for being more Ln-like, adopting a systematic +3 valence configuration [12, 14].

The first two actinides An and Th have their $6d$ shell filled before the $5f$ shell, as it lies lower in energy. However, for most other An, the $5f$ shell has some occupancy. The $5f$ electrons are not shielded by the $6s$ and $6d$ levels, as the $4f$ electrons were shielded in the Ln. In [14], Nd (a Ln) is compared U (an An) for similar valence states of +3. It is found that while the $4f$ orbital is shielded by the the $5s$ and $5p$ orbitals, the $5f$ shell extends beyond the $6s$ and $6d$, making it available to participate in compound formation [12]. The participation of the $5f$ electrons in bond formation is a striking difference in An compared to the Ln counterparts.

Due to the accessible valence states of the early An, they may be considered transition metal-like. Plotting the minimum volume cells of the transition metals, Ln, and An as in [15] demonstrates that the An minimum cell volume decreases with increasing Z, similar to the transition metals. However, the Ln remain relatively the

same size. Despite the similarity to transition metal trends, the An do not form close packed structures when the f-orbitals are chemically active [16]. As the f-orbitals are being filled and the cell volume shrinks, the crystal structure tends to become more disordered.

The f-electrons are key to the dynamic physics and chemistry of An compounds, partly due to relativistic effects [12, 15]. A particle's relativistic mass is given by a transformation of its rest mass m_0 [14, 17] as

$$m = \frac{m_0}{\sqrt{1 - \left(\frac{v}{c}\right)^2}}, \tag{1}$$

resulting in an increase of mass as a particle's velocity approaches the speed of light. Additionally, an electron orbiting a nucleus experiences the Coulomb force and for a larger number of protons in the nucleus, this electron experiences a greater centripetal force. However, the electron is still bound to its orbital. Two consequences of the relativistic effect are:

1. Inner $s-$ and $p-$orbital contraction: The electron will increase its orbital velocity due to its smaller orbital radius. From (1), a greater orbital velocity results in an increase in electron mass. Examining the hydrogen-like s and $p_{\frac{1}{2}}$ orbitals, the electron distance from the nucleus is given approximately by the Bohr radius, $a = \hbar^2/mc^2$. As the electron mass increases, the Bohr radius contracts. By decreasing the Bohr radius, the electrons are on average closer to the nucleus and less likely to form bonds with other atoms.

2. Outer $d-$ and $f-$orbital expansion: With the contraction of the inner orbitals, the outer electrons are shielded from the large positive charge at the core, experiencing a reduced Coulomb force. The orbitals expand and become less stable. Additionally, the f-orbitals screen charge poorly [11, 12, 15]. Consequently the

filled $4f$ shell does not assist in screening the outer $5p$ and $6s$ orbitals, allowing them to contract and the $5f$ electrons to expand.

1.3 Thorium and Thorium Oxides

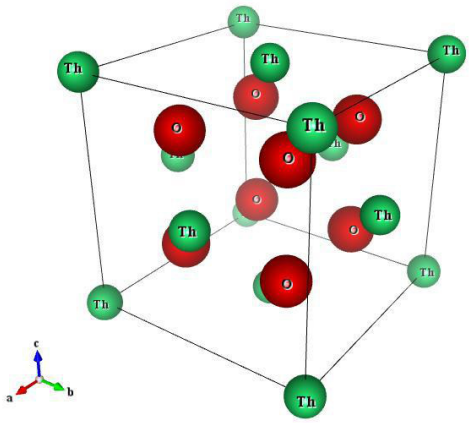

Figure 4. Unit cell of ThO_2 with lattice constant $a = 5.5975$.

Being an An, Th is characterized by having the $5f$ electronic orbitals available. At room temperature, Th is face-centered cubic (FCC) with a lattice constant of 5.0842 Å. At 1633 K, Th goes through a phase change and has a body-centered cubic (BCC) cell with a shorter lattice constant of 4.11 Å. Continued heating will result in reaching the melting point at 2023 K [14]. Furthermore, metallic Th, having delocalized (itinerant) $5f$ electron orbitals, is known to be superconducting at very low temperature (1.368 K). This property becomes less so with An with increasing Z, since the f-electrons become more localized.

When oxidized into the most stable form ThO_2, the Th FCC lattice is filled with O atoms. The O atoms form a simple cubic structure and the result is the fluorite structure as in Figure 4. This unit cell is of the $Fm\bar{3}m$ space group and has a variety of reported lattice constants [18–20], with the most quoted at 5.592 Å [14]. It is

typically clear or white, depending on the structural quality. Various sources report different ionic radii for Th^{4+}. From diffraction studies, Th has been reported to have an ionic radius of 0.94 Å when in 6 atom coordination and 1.05 Å in 8 atom coordination [21]. From Figure 4, a Th atom is surrounded by 8 O atoms. In turn, the O (1.38 Å ionic radius) atom is surrounded by 4 Th atoms. This results in a predicted 1.05+1.38 = 2.43 Å distance between Th and O; close to what is found later in this dissertation research.

1.4 Problem Statement

Starting with knowledge of these fundamental properties of the An and ThO_2, the goal of this research is to use spectroscopic methods to determine electronic and geometric structure for hydrothermally synthesized ThO_2. The research measures the bulk structure with x-ray absorption techniques and identifies possible defect centers. In turn, the electronic structure is extracted with photoemission techniques, using different energy regimes that are sensitive at and below the surface, demonstrating that the electronic structure agrees with the results of the geometric structure. This is confirmed with a third measurement with photoemission spectroscopy that demonstrates a surface-to-core level shift in the electronic structure of the single crystals. While electronic devices are not created, part of the underlying physics is investigated, namely, the geometric and electronic structure of ThO_2. In particular, this dissertation research seeks to answer the questions:

- What is the band gap of ThO_2? What does the band structure predict in terms of ionic and covalent behavior? Are the $5f$ electrons really empty/inactive?
- Is the local environment of the Th atom representative of the fluorite structure? Are there local geometric distortions?

- Is it possible to improve upon the EXAFS analysis methodology?
- Do the Th and O core level binding energies change between the bulk and surface? What is the effective Debye temperature as determined by XPS?

References

[1] G. Rousseau, L. Desgranges, F. Charlot, N. Millot, J. C. Niepce, M. Pijolat, F. Valdivieso, G. Baldinozzi, and J. F. Berar, *Journal of Nuclear Materials*, vol. 355, p. 10, 2006.

[2] Y. S. Kim, "A thermodynamic evaluation of the U–O system from UO_2 to U_3O_8," *Journal of Nuclear Materials*, vol. 279, pp. 173–180, Novemebt 2000.

[3] R. A. Knief, *Nuclear Engineering Theory and Technology of Commerical Nuclear Power*, 2nd ed. Taylor and Francis, 1992.

[4] D. Manara and B. Renker, *Journal of Nuclear Materials*, vol. 321, p. 233, 2003.

[5] T. Meek, "Semiconductive Properties of Uranium Oxides," *Waste Management 2001 Symposium*, 2001.

[6] M. Mann, D. Thompson, K. Serivalsatit, T. M. Tritt, J. Ballato, and J. Kolis, *Crystal Growth and Design*, vol. 10, no. 2146, 2010.

[7] M. Mann and J. Kolis, *Journal of Crystal Growth*, vol. 312, p. 416, 2010.

[8] M. A. Denecke, "Actinide Speciation Using X-ray Absorption Fine Structure Spectroscopy," *Coordination Chemistry Reviews*, vol. 250, pp. 730–754, 2006.

[9] R. Price, "Potential Uses of Depleted Uranium," *American Nuclear Society: 2000 International Winter and Embedded Topical Meetings*, 2000.

[10] G. H. Friedman, "Potential Uses for Depleted Uranium Oxides," U.S. Department of Energy, Tech. Rep., 2009.

[11] D. Shriver and P. Atkins, *Inorganic Chemistry*, 3rd ed. W. H. Freeman and Company, 1999.

[12] S. Cotton, *Lanthanide and Actinide Chemistry*. John Wiley and Sons, 2006.

[13] H. G. Friedman, G. R. Choppin, and D. G. Feuerbacher, "The Shapes of the f Orbitals," *Journal of Chemical Education*, vol. 41, no. 7, pp. 354–358, July 1964.

[14] L. R. Morss, N. M. Edelstein, and J. Fuger, *The Chemistry of the Actinides and Transactinide Elements*, 3rd ed. Springer, 2006, vol. 3.

[15] J. M. Wills and O. Eriksson, "Actinide Ground-State Properties," *Los Alamos Science*, no. 26, 2000.

[16] S. S. Hecker, "Plutonium Science Challenges Future Researchers," *Actinide Research Quarterly*, 2000.

[17] H. D. Young and R. A. Freedman, *University Physics with Modern Physics*, 11th ed. Pearson Addison Wesley, 2004.

[18] F. A. Rough and A. A. Bauer, "Constitution of Uranium and Thoriam Alloys," Battele Memorial Institute, Report, 1958.

[19] C. Hennig, "EXAFS investigation of U(IV) precipitates," Helmholtz-Zentrum Dresden-Rossendorf, Institute of Radiochemistry, Bautzner Landstrasse 400, 01314 Dresden Germany, Tech. Rep., 2009.

[20] S. Hubert, J. Purans, G. Heisbourg, and N. Dacheux, "Local stucture of actinide dioxide and solid solutions $Th_{1-x}U_xO_2$ and $Th_{1-x}Pu_xO_2$," *Inorganic Chemistry*, vol. 45, pp. 3887–3894, 2006.

[21] R. D. Shannon, "Revised Effective Ionic Radii and Systematic Studies of Interatomic Distances in Halides and Chalcogenides," *Acta Crystallograhica*, vol. A32, pp. 751–767, 1976.

II. General Theory

2.1 Overview

There exists a direct relationship between the geometric and electronic structure of a crystal, characterized by the replication of a structural subunit referred to as the unit cell and the corresponding reciprocal lattice. The crystalline electronic density is distorted from the free atom condition due to bonding with neighboring atoms (overlap of the atomic potentials) and the crystal lattice periodicity. The resulting solid state electronic wave functions are the Bloch electrons and solutions to the Schrödinger equation of the form (2), where H is the Hamiltonian, $U(\vec{r})$ is the periodic atomic potential, E is the eigenenergy, and Ψ the wave function describing the Bloch electrons [1]. The one-electron wave function solved from the Schrödinger equation has the form $\left\langle \vec{r} + \vec{R} | \psi \right\rangle$, where this periodicity is satisfied by Bloch electrons possessing wave vectors $\vec{k}$, such that $e^{i\vec{k}\cdot\vec{R}} \langle r|\psi\rangle = \langle r|\psi\rangle$. Hence, changing the crystal lattice changes the atomic potentials $U(\vec{r})$ and results in a different electron density.

$$H|\psi\rangle = \left(-\frac{\hbar^2}{2m}\nabla + U(\vec{r})\right)|\psi\rangle = E|\psi\rangle \tag{2}$$

In this research, a variety of spectroscopic techniques (Figure 5) are used. In this chapter, the theory behind those techniques is presented. To study the electronic structure, the primary measurements are various applications of photoemission spectroscopy (PES), namely: x-ray photoemission spectroscopy (XPS), ultraviolet photoemission spectroscopy (UPS), inverse photoemission spectroscopy (IPES), and x-ray aborption near edge structure (XANES). To study the geometric structure, the primary measurement is extended x-ray absorption fine fine structure (EXAFS).

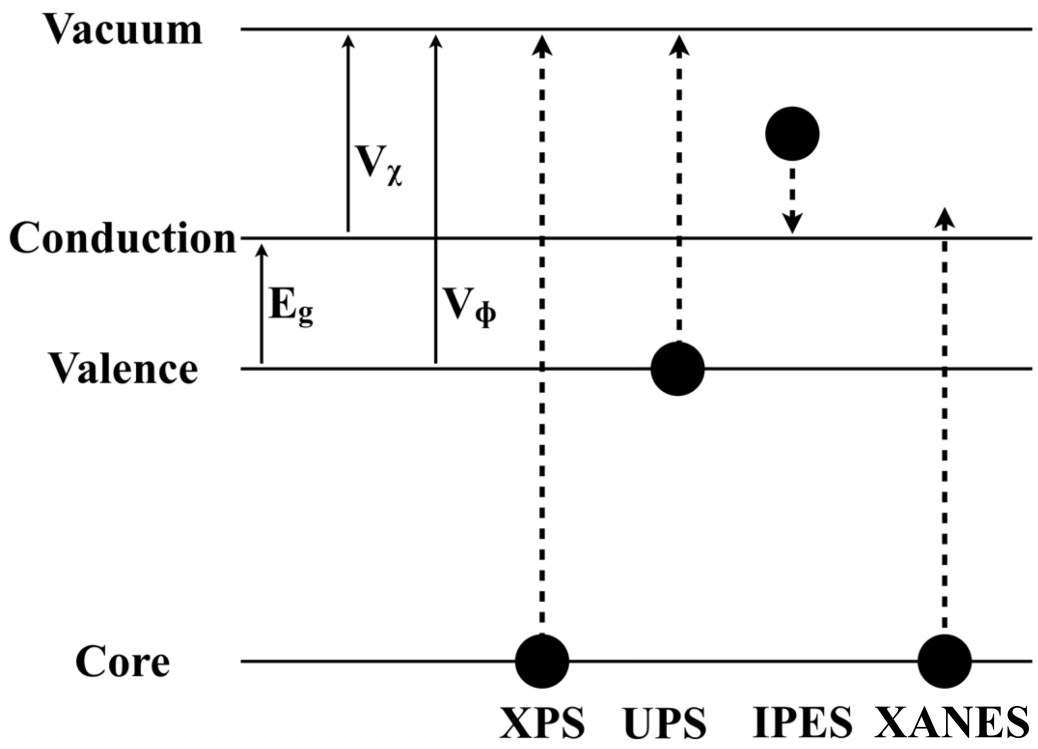

Figure 5. A schematic of the various spectroscopic processes used to investigate the atomic structure. E_g is representative of the band gap, V_χ of the electron affinity, and V_Φ of the work function.

2.2 Spectrographic Methods Applied in this Research

Referring to Figure 5, in XPS an x-ray excites an electron from the innermost atomic electronic level to the vacuum level. The emitted photoelectron's kinetic energy is measured and provides information about the atom's electronic structure. In UPS, the ultraviolet photon frees an electron from the various states within the atom's electronic structure depending upon the photon energy. The emitted electron provides information about the interaction. In IPES, an electron is captured in the conduction band and emits a photon as it loses energy. The emitted photon provides information about the conduction band of the crystal. In XANES, the photoemission processes is used to measure the unoccupied electronic energy states by absorbing a photon of energy less than that required to exceed the vacuum level. The electrons

relax back to a lower energy level and emit a photon. The emitted photon energy is measured providing information about the unoccupied energy states.

2.3 Photoemission Spectroscopy (PES)

Photoemission spectroscopy is an experimental technique which uses photons to probe the atomic electronic structure. In Figure 6, the "photoemission" is due to the measurement of the emitted electron's (photoelectron's) kinetic energy when the impinging photon equals or exceeds the electron's binding energy as

$$E_{kin} = \hbar\omega - (E_B + V_\Phi)\,, \tag{3}$$

where E_{kin} is the photoelectron's kinetic eneregy, $\hbar\omega$ is the photon energy, E_B is the electronic binding energy, and V_Φ is the work function. Many texts [2–5] in the academic community offer historical descriptions and reviews of the technique.

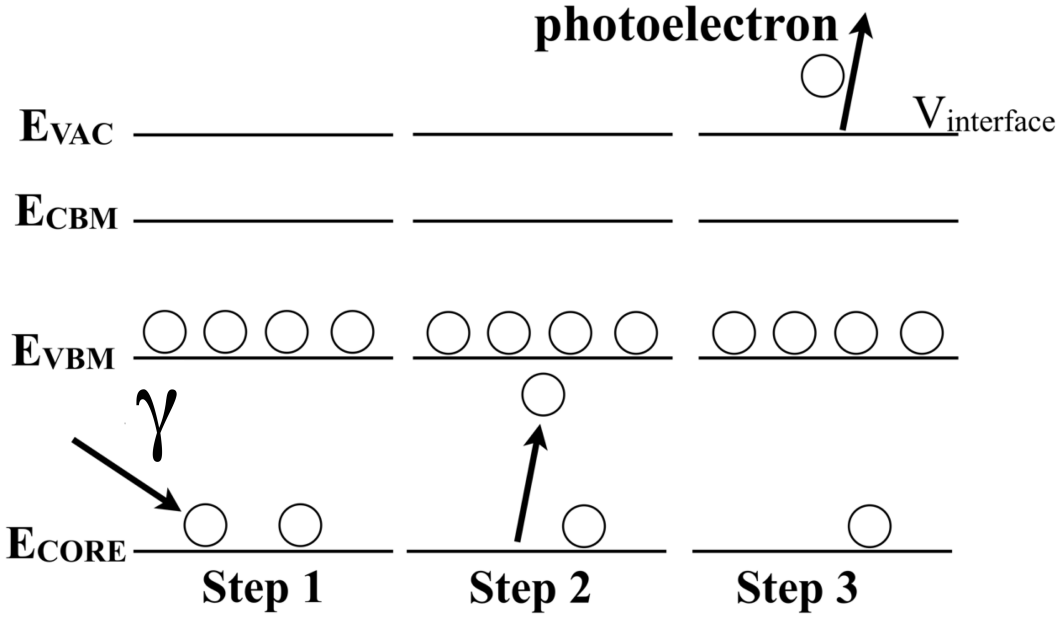

Figure 6. A schematic of the three-step photoelectric process. The open circles represent electrons at the indicated energy levels.

The photoemission process is well-described by a three-step model [3–6], as in Figure 6. Each of the three steps of this model is assumed to be independent. Fermi's Golden Rule governs the first step which concerns photon absorption by an atomic electron transitioning into a photoelectron. The transition probability requires knowledge of a perturbing or interacting potential.

Maxwell's equations for the coupled electric and magnetic fields, $\vec{E}(\vec{r},t)$ and $\vec{B}(\vec{r},t)$, are described by first order partial differential equations. It is generally useful to uncouple the two fields through the introduction of the vector potential $\vec{A}$ [7, 8]. The result is a system Hamiltonian in which the electromagnetic wave (photon) interacting with the electron may be described by (5) as detailed in [9]. Expanding (5) leads to (6) and (7), with the dipole and quadruple terms of (7) represented as the interaction Hamiltonian H_I (8).

$$
\begin{aligned}
H_0 &= \frac{p^2}{2m} + V(r) && (4)\\
\hat{H} &= \frac{1}{2m}\left[\vec{p} - \frac{q}{c}\vec{A}(r)\right]^2 + V(r) && (5)\\
\hat{H} &= \frac{p^2}{2m} - \frac{q}{2mc}\left[\vec{p}\cdot\vec{A} + \vec{A}\cdot\vec{p}\right] + \frac{q^2}{2mc^2}\vec{A}\cdot\vec{A} + V(r) && (6)\\
\hat{H} &= \left[\frac{p^2}{2m} + V(r)\right] + \left[-\frac{q}{2mc}\left[\hat{p}\cdot\vec{A} + \vec{A}\cdot\hat{p}\right] + \frac{q^2}{2mc^2}|\vec{A}|^2\right] && (7)\\
\hat{H} &= H_0 + H_1 && (8)
\end{aligned}
$$

Using Fermi's Golden Rule, the interaction Hamiltonian H_I describes the photoelectron current I_{PES} (9). In the equations that follow after (9), the perturbing Hamiltonian is introduced from (7) and the definition of the momentum operator, $\vec{p}= -i\hbar\vec{\nabla}$, is inserted.

$$
\begin{aligned}
I_{PES} &= \left|\langle f|\, H_1\, |i\rangle\right|^2 && (9)\\
I_{PES} &= \left|\langle f|\, \frac{q}{2mc}\left[i\hbar\vec{\nabla}\cdot\vec{A} + i\hbar\vec{A}\cdot\vec{\nabla}\right]|i\rangle + \langle f|\, \frac{q^2}{2mc^2}|\vec{A}|^2\,|i\rangle\right|^2 && (10)
\end{aligned}
$$

A suitable choice in the vector potential gauge is chosen based upon the commutation of the momentum operator and vector potential $\left[\vec{p},\vec{A}\right]$ (11). Using the divergence relationship in (12), the first term in (13) may be rewritten as (14).

$$\begin{aligned}
\left[\vec{\nabla},\vec{A}\right] &= \vec{\nabla}\cdot\vec{A}-\vec{A}\cdot\vec{\nabla} && (11)\\
\vec{\nabla}\cdot(f\vec{A}) &= f(\vec{\nabla}\cdot\vec{A})+\vec{A}\cdot(\vec{\nabla}f) && (12)\\
\left[\vec{\nabla},\vec{A}\right]\psi &= \vec{\nabla}\cdot(\vec{A}\psi)-\vec{A}\cdot(\vec{\nabla}\psi) && (13)\\
\left[\vec{\nabla},\vec{A}\right]\psi &= \psi(\vec{\nabla}\cdot\vec{A})+\vec{A}\cdot(\vec{\nabla}\psi)-\vec{A}\cdot(\nabla\vec{\psi}) && (14)\\
\left[\vec{\nabla},\vec{A}\right] &= \vec{\nabla}\cdot\vec{A} && (15)\\
\text{Thus...}\ \vec{p}\cdot\vec{A}-\vec{A}\cdot\vec{p} &= i\hbar\vec{\nabla}\cdot\vec{A} && (16)
\end{aligned}$$

By definition, $\vec{A}$ is chosen such that $\vec{B}=\vec{\nabla}\times\vec{A}$ [7,8]. Consequently, the gradient of a scalar field added to $\vec{A}$ will not change $\vec{B}$ (i.e. $\vec{\nabla}\times(\vec{\nabla}f)=0$). The appropriate choice of gauge in this case is the Coulomb gauge so that $i\hbar\vec{\nabla}\cdot\vec{A}=0$ and $\vec{p}\cdot\vec{A}=\vec{A}\cdot\vec{p}$. The interaction Hamiltonian from (7) may be rewritten, and the photoelectron current is determined as

$$I_{PES} = \left|\langle f|\,\frac{q}{mc}\left[\vec{A}\cdot\vec{p}\right]|i\rangle+\langle f|\,\frac{q^2}{2mc^2}|\vec{A}|^2\,|i\rangle\right|^2. \qquad (17)$$

In the first order approximation, terms such as $|\vec{A}|^2$ are neglected and may be ignored. The final result for the photoemission current is the dipole approximation

$$M_{fi} = \frac{i\hbar e}{mc}\langle f|\,\vec{A}\cdot\vec{\nabla}\,|i\rangle^2, \qquad (18)$$

where M_{fi} is the transition matrix between initial and final states. Some texts refer to this as the velocity form of the matrix element [4], due to the presence of the momentum operator, as opposed to the position operator $\vec{r}$ (obtainable by taking

the commutation of $\vec{r}$ and H_0) or the gradient of the potential $V(\vec{r})$ (length and acceleration forms respectively).

The number of observed electrons that transition with some energy E due to a photon with energy $\hbar\omega$ is given as

$$I_{PES} \propto \sum_{if} |M_{if}|^2 \, \delta(E_f - E_i - \hbar\omega), \tag{19}$$

taking advantage of the matrix element previously described. In the first step of the three-step photoemission model photoemission, the probability of transitioning an atomic electron between energy levels or to the vacuum level depends on the result for the matrix elements determined by (19). The additional delta function δ assures energy conservation. The final energy of the electron E_f must be equivalent to the electron's initial energy plus the photon energy contribution.

(19) describes step one of the photoelectron transition process. The overlap between initial and final state wave functions and the dependence upon the energies involved explain the dependence of photoemission peak resolution and intensity of a given excitation energy $\hbar\omega$.

The second step of the three-step model is transport of the photoelectron through the solid material. Photoelectrons which propagate through a crystal without scattering appear as photoemission peaks in experimental data. However, a large number of electrons may instead scatter and lose some energy to the matrix through which they transport. These scattered electrons will appear as decaying shoulders on photoemission peaks and as a growing secondary background. This secondary background is a result of the second step of the three-step model.

Experimental spectra are often shown in energy with respect to the Fermi level, although it is the photoelectrons' kinetic energy which is measured. Referencing the energy conservation of (19), the closer E_i is to zero, the more kinetic energy the

photoelectron will have up to the point $E_f = \hbar\omega$. This results in the secondary electron cutoff. When the binding energy is great enough that the excitation photons $\hbar\omega$ have just enough energy to free the electron, then these will have negligible kinetic energy. In the photoemission spectra, these photoelectrons appear at the highest binding energy and there is an abrupt drop to zero in the photoelectron intensity.

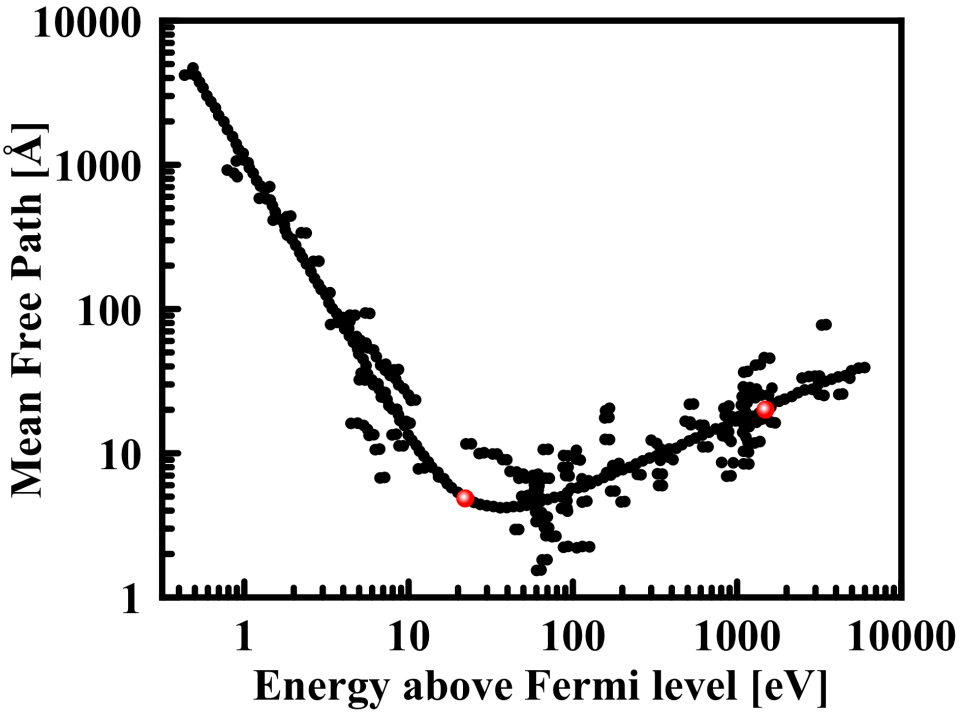

Figure 7. Mean free path of electrons as a function of energy referenced to the Fermi level. Data obtained from [5]. This figure has been created with permission from originating journal. Y-axis has been converted to Å. Red markers indicate the excitation energies for He(I) (21.2 eV) and Al (1486.6 eV) sources, which were used in this research.

In Figure 7, the electron mean free path (Å) is plotted as a function of energy (eV) for a variety of materials. The solid black line is the trend line demonstrating the average mean free path for an electron transporting through a material with energy greater than the Fermi energy E_F. The figure's minimum occurs between 4–5 Å. The electrons with kinetic energy to the left of the minimum have an increased range through the material because their kinetic energy (on average) is too low to excite

electronic excitations with the bound electrons in the material. In Chapter 5, the TPP-2M equation (60) is discussed which describes the electron mean free path in more detail. Most fixed x-ray sources are on the order of 1000 eV which is greater than the approximate minimum at 40 eV of Figure 7. Many electrons are expected to have a mean free path great enough to escape the material without scattering and be able to contribute to a measurable photoemission peak [3].

In the final step of the three-step model, a photoelectron which reaches the surface will have some well-defined energy E and momentum $\hbar\vec{k}$. Hence, a photoelectron which reaches the surface must now escape into the vacuum with kinetic energy as

$$E_{\text{kin}} = \hbar\omega - (E_B + V_\Phi) = \frac{p^2}{2m_e} \quad = \quad \frac{2\hbar^2}{m_e}\left(k_{||}^2 + k_\perp^2\right), \tag{20}$$

where $k_{||}$ is the electron momentum parallel to the surface and $k_\perp$ is the electron momentum perpendicular to the surface.

There is an abrupt change of potential at the surface of the crystal represented by $\text{V}_{\text{interface}}$ in Figure 6. While the potential along the surface is still periodic, the potential in the direction normal to the surface results from the interface of the crystal surface and vacuum. The fraction of the photoelectron's momentum perpendicular to the surface must result in a kinetic energy great enough to overcome this interface potential as in (21).

$$E_\perp = \frac{\hbar^2 k_\perp^2}{2m_e} \quad \geq \quad V_{\text{interface}} \tag{21}$$

In the limiting case, the lowest energy electron which may be detected in step three depends on (22). In this equation, the momentum $k_\perp$ in the perpendicular direction belongs to the photoelectron that reached the surface from step two with

energy E and had just enough energy to overcome the interface potential:

$$k_{\perp} = \frac{\sqrt{2m_e(E + V_{\text{interface}})}}{\hbar}. \tag{22}$$

The parallel component of the photoelectron as it reaches the surface continues to interact with the crystal's periodic potential and must remained conserved. The parallel component of the momentum may be expressed as in (23). The angle is taken with respect to the surface normal.

$$k_{||} = \frac{\sqrt{2m_e E_{\text{kin}}}}{\hbar} \sin\theta \tag{23}$$

2.4 X-ray Photoemission Spectroscopy (XPS)

X-ray photoemission spectroscopy is a subset of the photoemission technique in which the excitation photons consist of x-rays with a tentative range on the order of 1–10 keV, allowing for the removal of core level atomic electrons as demonstrated by the XPS line in Figure 5. Reasons for investigating the core level binding energies include studying chemical charge shifts due to a changing bonding environment, the difference between surface and bulk environments, the band gap through shake-up and shake-down events, the relative elemental concentrations within a sample, and the effective Debye temperature coefficient [3].

2.5 Ultraviolet Photoemission Spectroscopy (UPS)

Ultraviolet photoemission is similar to x-ray photoemission, however it uses ultraviolet photons as the excitation source. The tentative photon range for a UV source is 0.01 to 1.0 keV. Referring to Figure 7, the mean free path of the photoelectrons is much smaller than for the x-ray excitation, approximately 5 Å for the He(I) lamp

used in this research (21.2 eV excitation). This is contrasted against the 20 Å for the Al x-ray source. Both approximate mean free paths are marked in red in Figure 7.

The mean free path measurements are very sensitive since the particle must traverse the bulk, the surface, and the surrounding air (high vacuum) in order to be detected. Photoelectrons which escape the material through XPS and UPS processes are then able to transport through ultrahigh vacuum environments to be detected as discussed in Chapter 3.

2.6 Inverse Photoemission Spectroscopy (IPES)

Inverse photoemission spectroscopy follows the same theory but in the reverse process; the initial and final states are reversed. The initial state for this spectroscopic technique is a low energy electron. The electron is captured in the unoccupied states. The electron transitions to a lower energy level and emits a photon. The photon's energy is measured, providing information concerning the energy levels of the unoccupied states.

2.7 X-ray Absorption Fine Structure (XAFS)

Figure 8 is a schematic of a circular pond containing two other open circles which represent rocks. A small rock (shaded outside pond) is thrown into the pond and hits a second rock (shaded inside pond) causing it to vibrate and create outward rippling waves. These waves encounter the larger rocks in the pond, resulting in backscattered waves that move out in all directions. Some of the backscattered waves move back toward the original source of the ripples and interfere with the forward moving waves. The degree of constructive or destructive interference depends on a few conditions:

1. the original energy of the thrown rock.

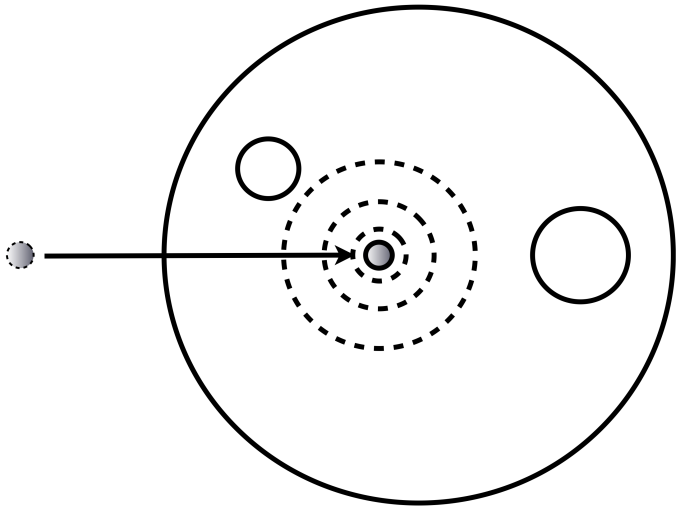

Figure 8. Schematic of the ripples from a rock thrown into a large circular pond populated with two other rock.

2. the placement of the struck rock in the pond.

3. the placement of the other rocks within the pond.

4. the shapes and numbers of rocks within the pond.

Given enough information about the pond, its contents, the thrown rock, and the struck rock, an observer could take multiple snapshots of the wave interference phenomenon and reconstruct how many rocks were in the pond and the placement of those rocks. The process of analyzing this signal for underlying geometric content is very similar to how an extended x-ray absorption fine structure (EXAFS) experiment is conducted.

In an EXAFS experiment, a signal is analyzed in order to determine the structure of a material. In particular, the "struck/rippling rock" is a specific element that exists within the material. For example, in a sample of Al_2O_3, an observer would use either the Al or the O as the source. The electrons within either the Al or O are excited by x-rays in order to create photoelectrons. The thrown rock represents the x-ray photons impinging upon the material in order to excite the photoelectrons (ripples).

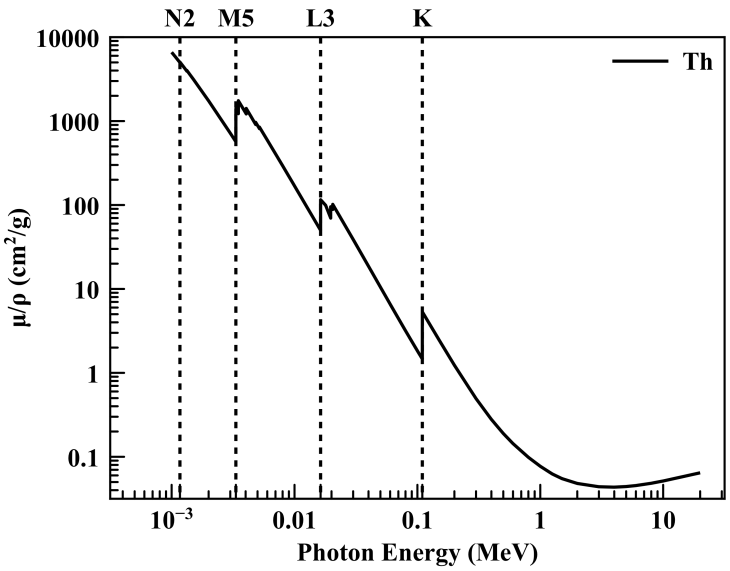

Figure 9. The mass attenuation coefficient for Th as a function of x-ray photon energy. Some of the notable photoelectric cross-section edges are marked by vertical lines.

The electronic binding energies of every element are different (e.g. Th in Figure 9). It is possible to choose which element to use as the "rippling rock" by using an x-ray energy (thrown rock) corresponding to the electronic binding energy of choice. The emitted photoelectron is akin to the forward scattering waves in the pond analogy. These photoelectrons have a wave-like nature which can backscatter off the electronic shells of the neighboring atoms. In turn, the backscattered photoelectric waves interfere with the forward scattering waves. The degree of the constructive or deconstructive interference may be compared to the pond analogy, where the resulting interference depends upon:

1. the energy of the photoelectron emitted (and hence the incident x-ray energy).
2. the central atom chosen according to the excited photoelectric energy.
3. the geometry of the coordination shells surrounding the central atom.
4. the identities and coordination of the atoms surrounding the central atom.

In an ideal EXAFS experiment, the incident x-ray energy is varied from below the binding energy to approximately 1000 eV above the binding energy. This results in a oscillation pattern which appears after the photoelectric edge. It is this modulation which can be extracted from an EXAFS experiment, analyzed using Fourier transformations, and then used to identify the local geometry of a material.

2.8 Application of EXAFS to a simple model

In Figure 10, a basic sinusoidal function $\sin(2kR)$ is plotted. The function was generated with steps in k-space of 0.1 Å^{-1} increments and the R-parameter fixed to 1.0 Å. The basic functional form given in (24) can be readily determined by noting that the amplitude A is 1.0 and the period T of the harmonic function is given by $T = 2\pi/B$. From Figure 10, the period is π, with no phase shift or vertical translation ($C = 0$, $D = 0$). Thus, $T = \pi$ implies that if $B = 2R$, then $R = 1$ Å. Combining all the information together into (24) gives the functional form of $\sin(2k)$.

$$A\sin(Bx + C) + D \tag{24}$$

In the simple example of Figure 10, it is fairly straight forward to isolate the parameter R. However, the Fourier transform is another method that could be used to extract the R component. Letting $\Psi(k)$ represent the data, the Fourier transform from momentum to coordination space is given by:

$$\Psi(R) \;=\; \frac{1}{\sqrt{2\pi}}\int_{-\infty}^{\infty}\Psi(k)e^{ikR}dk. \tag{25}$$

The Fourier transform in (25) is the idealized situation in which there is an infinite amount of data $\Psi(k)$. In reality, the Fourier transform is finite. In Figure 10, the

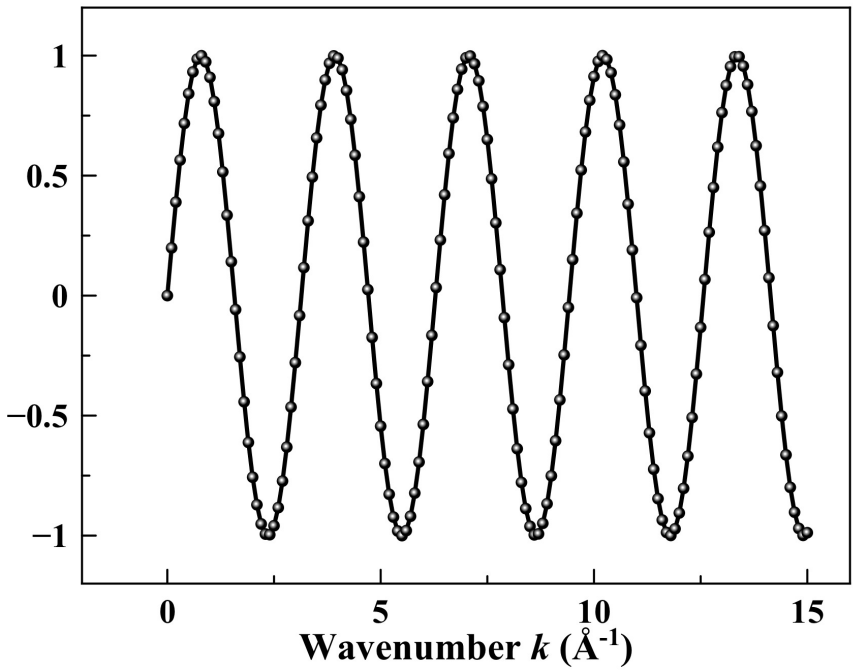

Figure 10. A sine function generated by taking $\Delta k = 0.1$ Å^{-1} steps and fixing $R = 1$ Å.

data are known only for $k \in (0, 15)$ Å^{-1}. Thus, (25) is more appropriately written as (26), where the finite range is (a, b).

$$\Psi(R) \;=\; \frac{1}{\sqrt{2\pi}} \int_a^b \Psi(k) e^{ikR} dk \tag{26}$$

Considering the finite integration of just the exponential term over symmetric bounds results in (27) [10]. This is related to the "sinc" function which has the form $\sin(x)/x$. In fact, numerically computing the Fourier transform of Figure 10 gives the result plotted in Figure 11, where the sinc function is centered around $R = 1$. If the bounds extend to infinity, the sinc function approaches the delta peak and the result is $2\pi\delta(R-1)$, a delta function at $R = 1$.

$$\int_{-a/2}^{a/2} e^{ikR} dk \;=\; \frac{2\pi \sin(aR/2)}{R} \tag{27}$$

For ease of viewing, Figure 11 is plotted from $R = 0$ to 3 Å, while an inset shows the transform up to 10 Å. The Fourier magnitude has been plotted in black as an envelope curve to assist in displaying the real and imaginary contributions to the peak. The Fourier transform identifies the primary contribution to be at $R = 1.0$ Å.

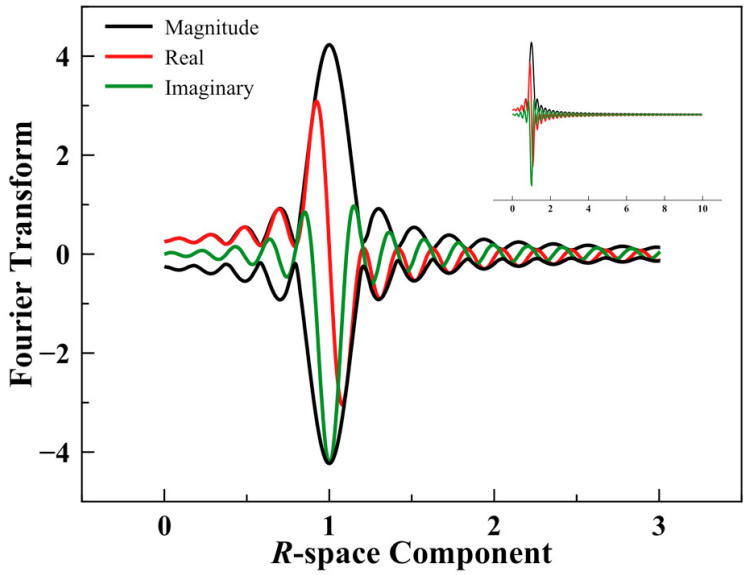

Figure 11. Fourier transform of Figure 10. The inset shows the transform up to 10 Å.

The width of the peaks is determined by the extent of the k-space used in the transform, related to the knowledge of the data limits in the Fourier transform. This is very similar to the Heisenberg Uncertainty Principle as presented in (28). Knowing more about the signal in one space will restrict the knowledge in another. For EXAFS, this is not a large problem, as a researcher is usually attempting to establish clear peaks in R-space and consequently will use as much of the k-space as possible.

$$\Delta R \Delta k >= 1 \tag{28}$$

In Figure 12 the Fourier transform for Figure 10 is plotted for different Δk. The ΔR peak increases as the length of Δk becomes smaller. In order to distinguish

two more peaks in R-space that are close to one another, it is important to include sufficient k-space.

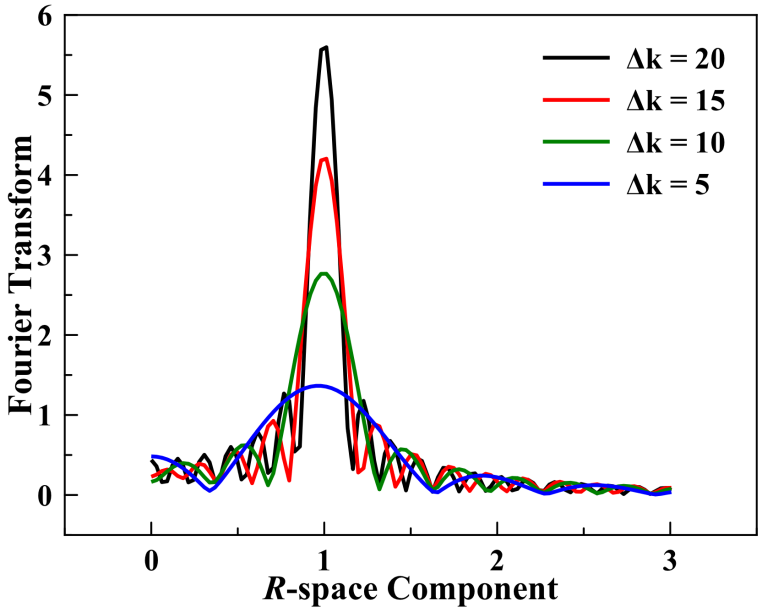

Figure 12. The magnitude of the Fourier transform for Figure 10 taken for different extents in k-space.

2.9 The EXAFS equation for quantitative analysis

The full extended x-ray absorption fine structure equation is shown as (29) [10,11], where $\chi(k)$ is the EXAFS, S_0^2 is the amplitude reduction factor, N_j is the coordination number of the j-th shell, $f_j(k)$ is the effective scattering amplitude, R_j is the coordination distance to the j-th shell, $\lambda(k)$ is the electron mean free path, σ^2 is the EXAFS Debye-Waller factor, and $\delta(k)$ is the phase shift. Ideal for studying amorphous materials, reaction chemistry, and crystalline distortions, EXAFS is a local structure probe and does not require long range order to extract geometric and electronic information. The concepts behind the parameters of (29) are discussed in this

section, following [10].

$$\chi(k) \quad = \quad S_0^2 \sum_j \frac{N_j f_j(k)}{kR_j^2} e^{-\frac{2R_j}{\lambda(k)}} e^{-2k^2\sigma^2} \sin(2kR_j + \delta(k)) \tag{29}$$

X-ray absorption spectroscopy (XAS) uses photons as the atomic excitation probe. A photoelectron is emitted, according to the same theory as presented on photoemission spectroscopy. The momentum p of the photoelectron is related to its wavelength λ by de Broglie's relation. Using this relation and considering the wave nature of the photoelectron through the wave-particle duality, the outgoing wave has a probability of scattering off of neighboring atoms, as in step two of the three-step photoemission model. From a wave form perspective, a photoelectric wave which is backscattered will interfere with the forward scattering wave, resulting in constructive and destructive interference patterns.

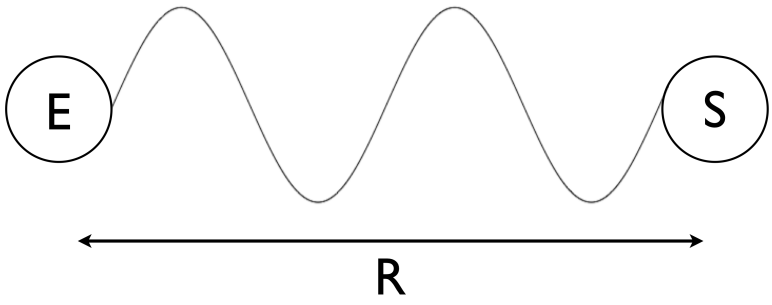

Figure 13. An atom (E) emits a photoelectric wave that scatters off a neighboring atom (S) from a given distance (R).

The constructive or deconstructive interference condition depends upon the photoelectron's wavelength and the distance between the emitting atom and the scattering atom as in Figure 13. The constructive interference condition is stated in (30), where R is the distance between the emitting and scattering atoms, λ is the photoelectric

wavelength, and n is an integer. Constructive interference occurs when the distance between the scattering atom and the emitting atom are a whole integer of the photoelectric wavelength as:

$$2R = n\lambda. \tag{30}$$

In a material, the atomic positions are assumed fixed for most practical applications, hence by varying the photoelectric wavelength a means of probing the distance R is introduced. The constructive and deconstructive interferences appear as oscillations in the absorption spectrum. These modulations χ of the absorption coefficient represent the fine structure.

The fine structure of the neutral atom absorption spectrum may be represented as a harmonic function as in (31), where the sine is used, as opposed to the cosine, for historical reasons. Satisfying the constructive interference of (30) will result in the maximum value for (31). Using the relationship between the wavenumber and the wavelength, (31) is rewritten as (32).

$$\chi \propto \sin\left(2\pi\frac{2R}{\lambda} + \frac{\pi}{2}\right) \tag{31}$$

$$\chi \propto \sin\left(2kR + \frac{\pi}{2}\right) \tag{32}$$

The proportionality symbol has been used in (31) and (32) under the assumption of elastic scattering. However, the photoelectron could scatter inelastically or not scatter at all. It is the elastic scattering that is necessary for the EXAFS interference, thus an effective scattering term is added to (32) to form (33).

$$\chi(k) = f_{\text{eff}}(k)\sin\left(2kR + \frac{\pi}{2}\right) \tag{33}$$

This effective scattering factor accounts for the various elastic and inelastic scattering probabilities off of the neighboring atoms. It is a function of the wavenumber since the scattering itself will be a function of the photoelectron momentum. This term also accounts for the geometry of the scattering mechanism. In Figure 13, the distance between the neighboring atom and the source of the photoelectron is a straight path, however in a crystal there may be scattering mechanisms that include more complicated geometries. These scattering probabilities need to be considered separately.

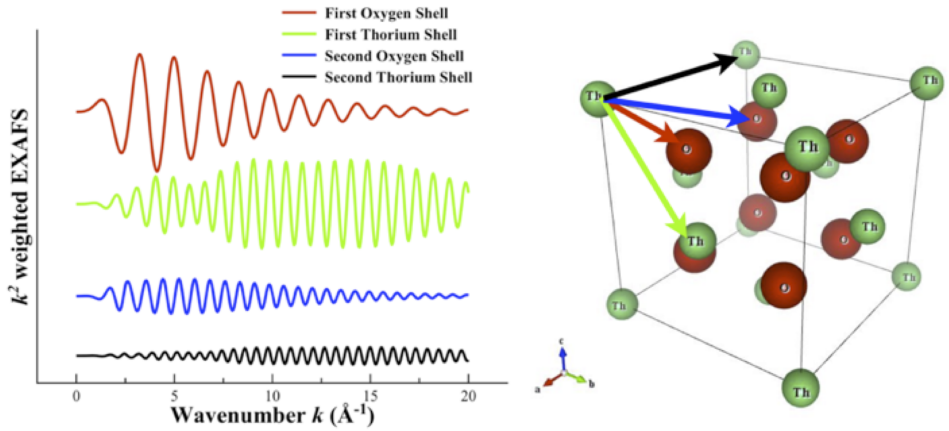

Figure 14. Theoretical EXAFS contributions from the nearest neighboring O and Th atoms in a fluorite ThO_2 unit cell.

In Figure 14 theoretical EXAFS modulations are plotted for the nearest neighboring O and Th atoms in a fluorite ThO_2 unit cell. The unit cell is shown on the right of the figure with colored arrows originating from the source of the photoelectron, a Th atom. Each of the colored arrows corresponds to the theoretical EXAFS modulation contribution shown on the lefthand side of the figure. The EXAFS paths are plotted as a function of the photoelectric wavenumber. From this figure, the influence of the effective scattering factor $f_{\text{eff}}(k)$ is observed. The O atoms have a scattering factor that is larger at low wavenumber while the Th atoms tend to have a greater amplitude at high wavenumber.

Additionally, the duration of the Th oscillations extends longer than the O contribution. If an atom has a large number of electrons, then the probability of scatter is greater. Consequently, low Z atoms such as B, C, and O, have a lower scattering probability than high Z atoms such as Pb, Th, and U. An example of using EXAFS to study the geometric structure of materials with low Z atoms may be found in sources such as [12]. The importance of the effective scattering term is paramount such that entire codes have been written to address calculating the effective scattering paths and mechanisms of spherically outgoing photoelectric waves as a function of energy. One such code used in this dissertation research is FEFF [13] named after the very term of the EXAFS equation $f_{\text{eff}}(k)$.

A further adjustment to (33) results in (34). The new addition is the summation over j. This summation is the result of propagating the wave to all nearest neighbors as in Figure 14. In this figure, a Th atom is surrounded by 8 O atoms as the first coordination shell. In the most simplistic consideration, only scattering from a nearest neighbor and back to the source atom is considered. The summation simplifies to scattering over coordination shells with N_j representing the degeneracy of the coordination shell.

$$\chi(k) \;=\; \sum_j N_j f_{\text{eff}}(k) \sin\left(2kR_j + \frac{\pi}{2}\right) \tag{34}$$

The most simple case of scattering is generally referred to as "single scattering." However, the summation in (34) is more general when considering multiple scattering paths. In this case, j is the j-th scattering path with N_j denoting the degeneracy in the scattering paths and R is no longer the coordination shell distance but the total distance of the elastic scatter. As an example of this concept, consider again Figure 14. A red arrow indicates the nearest neighboring coordination shell composed of 8 O atoms. The second coordination shell consisted of 12 Th atoms. An example of

a multiple scattering path would consist of a photoelectric wave elastically scattering off of the O atom then off of the Th atom before returning to the source Th atom. This is considered a multiple scattering path with 3 legs. Contrarily, all single scattering paths consist of 2 legs.

Figure 13 is simplistic, and the outgoing wave is more appropriately considered as a spherical wave [14, 15]. The result of the spherical wave approximation is the photoelectron wave will decay as $1/R^2$. This $1/R^2$ divergence is one reason EXAFS is a probe of the local structure. The resulting equation including the spherical divergence of the wave is:

$$\chi(k) = \sum_j N_j \frac{f_{\text{eff}}(k)}{kR_j^2} \sin\left(2kR_j + \frac{\pi}{2}\right). \tag{35}$$

The inclusion of the wavenumber is accompanied by a redefining of the effective scattering potential in units of Angstroms. This has the benefit of becoming dimensionless if the entire equation is later multiplied by k to weight the EXAFS modulations, as is customary and was done in this dissertation research.

While (35) accounts for the probability of scattering with the electronic density of an atom through the $f_{\text{eff}}(k)$ term, there is no accountability for interacting with the atomic potentials. Different atoms will have different atomic potentials. Whether they are considered from a crude quantum mechanical square well potential or a more refined muffin tin, these differing atomic wells will influence the photoelectron's phase. The photoelectron will be phase shifted before and after entering a region with an atomic potential. The atomic potential is an attractive, deep well and energy conservation requires an increase in kinetic energy in the region of the attractive potential. This phase shift is accounted for in (36) as $\delta(k)$ (not to be confused with

the Dirac delta).

$$\chi(k) \;=\; \sum_j N_j \frac{f_{\text{eff}}(k)}{kR_j^2} \sin\left(2kR_j + \delta(k)\right) \tag{36}$$

The initial and final state wave functions are not identical for the forward and backward scattering processes. The initial state consists of an atomic bound electron. After absorbing a photon and releasing a photoelectron, the atom is left in an excited state with a "core hole." The remaining atomic bound electrons are not as well shielded and respond to the more positive charge. This incomplete overlap between the initial and final state electronic wave functions is accounted for in the amplitude reduction factor S_0^2 of (37) and has a value usually between 0.7 and 1.0 [10].

$$\chi(k) \;=\; S_0^2 \sum_j N_j \frac{f_{\text{eff}}(k)}{kR_j^2} \sin\left(2kR_j + \delta(k)\right) \tag{37}$$

In this dissertation research, S_0^2 is calculated using the FEFF code. Experimentally, it is sometimes estimated by using a standard that has a well-known coordination number such as a pure metal. The concept of chemical transferability is then used to assign the same S_0^2 to another compound. However, the lack of reliable standards, particularly in actinides makes this difficult and even unreliable considering that the actinides exhibit a variety of chemical and electronic properties depending upon the coordination environment.

The final two parameters in the EXAFS equation include two exponential terms that account for phonon and static disorder effects in a sample. The first exponential term accounts for the photoelectron's mean free path $\lambda(k)$. The photoelectron's elastic scattering cross-section will compete with inelastic scattering processes such as phonon interaction. Additionally, the atomic core hole will not exist indefinitely before decaying by fluorescence or Auger electron emission. These loss mechanisms

become more likely as the photoelectron scatters farther from the source atom. The exponential decay of the EXAFS signal based upon the mean free path solidifies the local order physics of the spectroscopic technique as:

$$\chi(k) \quad = \quad S_0^2 \sum_j N_j \frac{f_{\text{eff}}(k)}{kR_j^2} e^{-\frac{2R_j}{\lambda(k)}} \sin\left(2kR_j + \delta(k)\right). \tag{38}$$

The second exponential term accounts for the changing coordination environment. X-ray absorption fine structure (XAFS) (both XANES and EXAFS) is a bulk measurement. Thus, unless the material is a perfect crystal free of any structural disorder, (38) does not account for signal loss by averaging the varying coordination environments. This varying coordination environment is not only a result of the static disorder, but also temperature dependent and a result of thermal disorder. The atomic vibrations influencing the EXAFS technique will change the scattering of the photoelectronic wave. These effects are accounted for in the EXAFS *Debye-Waller* factor σ^2 as:

$$\chi(k) \quad = \quad S_0^2 \sum_j N_j \frac{f_{\text{eff}}(k)}{kR_j^2} e^{-\frac{2R_j}{\lambda(k)}} e^{-2k^2\sigma^2} \sin\left(2kR_j + \delta(k)\right). \tag{39}$$

The EXAFS equation is restated in (39). The terms which are calculated in this research are S_0^2, f_{eff}, $\lambda(k)$, and $\delta(k)$ using the FEFF code. Terms which are fit to experimental data to exact structural information are N, σ^2, and most importantly R.

2.10 Latin Hypercube Sampling Methodology

The EXAFS data collection process is relatively quick. However, the data analysis is intensive, taking weeks or even months for a single data set. The primary difficulty is in finding the correct starting model (Figure 15.) Assuming that a structural model is known, the next difficulty is in determining the correct parameters that

provide an appropriate fit to the data. Often, only some general information about the parameters is known *a priori*.

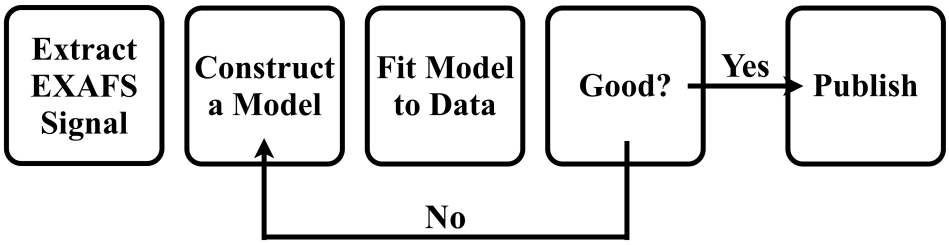

Figure 15. The general methodology for analyzing EXAFS.

A researcher often uses a variety of techniques to find the"best fit" parameters. The techniques range from fitting multiple data sets to combining parameters across coordination shells in clever, mathematical ways. In almost all cases, the methodology extends the number of data points as compared to the number of variables in the fitting routine. In general, this is constrained by the Nyquist criterion (40), where the number of independent points is constrained by the information present in the experimental data (k-space) and what is being extracted (R-space) [10] .

$$N_{\text{points}} = \frac{2\Delta k \Delta R}{\pi} \tag{40}$$

In the pursuit of this dissertation research, a code was developed to address some of the difficulties of: (1) shortening the EXAFS analysis time, (2) extracting parameters representative of the true data and not a false minimum, and (3) removing experimenter bias during the EXAFS analysis. This code used a Latin hypercube sampling approach to measure the fitting parameter space. The code not only addressed all the difficulties mentioned, but it also allowed for the exploration of very large parameter spaces in a time period much faster than would be feasible by a traditional non-linear-fitting guess and check methodology.

Figure 16 is a schematic of a three dimensional Latin hypercube. In a true Monte Carlo process, the number of divisions N is equivalent to 1. A value for each parameter is randomly chosen within a specified parameter space. The Latin hypercube process is a mixture of stratified random and Monte Carlo sampling. For example, if a parameter is bounded in the interval (P_i, P_f), then it is divided into the intervals $(P_i, \frac{1}{N}P_f, \frac{2}{N}P_f, ..., P_f)$. A random value for each parameter is chosen from the subintervals. Thus, if $N = 3$, then a random value will be chosen from the subintervals $(P_i, \frac{1}{3}P_f)$, $(\frac{1}{3}P_f, \frac{2}{3}P_f)$, and $(\frac{2}{3}P_f, P_f)$.

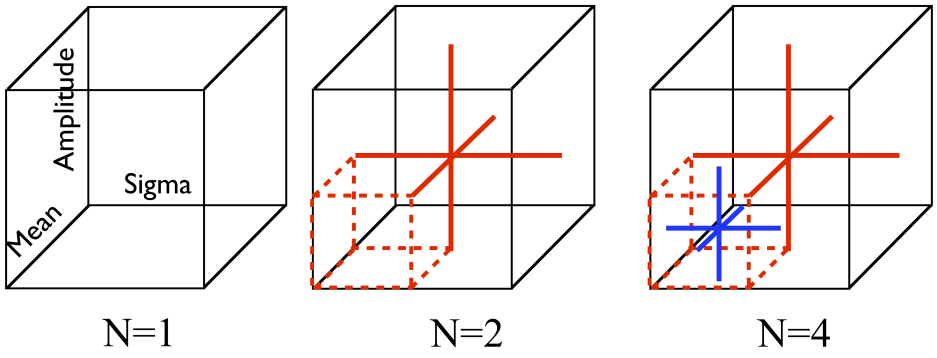

Figure 16. Schematic of a three dimensional Latin hypercube sampling.

This process is completed for each parameter that is in the hypercube. These random numbers differ from a pure Monte Carlo sampling in that they represent some linearly distributed sampling from the entirety of the hyperspace, where the resolution of the hyperspace depends upon the number of uniform divisions. After sets of random numbers are determined for each of the parameters, they are randomly matched into sets. This is when the Latin hypercube process differs from a direct stratified random sampling. In a stratified random sample, the entire hypercube will be sampled going from sub-cube to sub-cube. While this methodology is exhaustive, it can also be time consuming if the number of parameters and divisions is large. Conversely, after multiple iterations of a Latin hypercube sampling, the parameter

space can often be reduced to regions of possible minimums at finer resolution with much less time and memory.

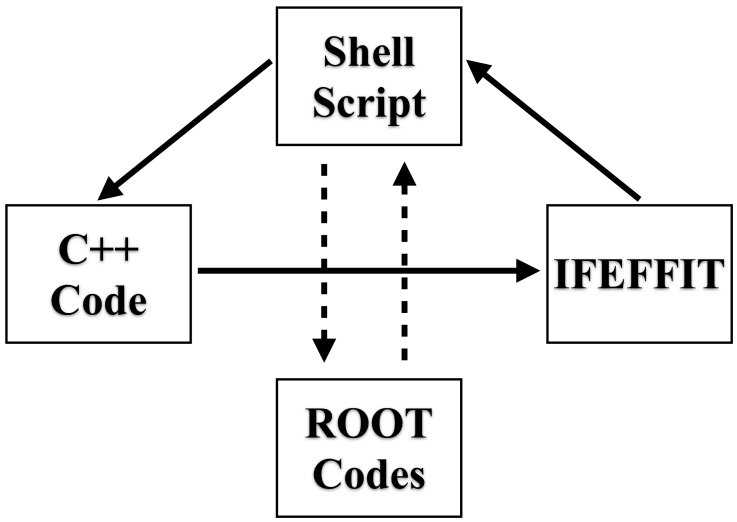

Figure 17. Software overview for Latin hypercube sampling procedure.

A series of codes were written in order to implement the Latin hypercube approach and analyze the EXAFS data. The general schematic for how these codes and languages interfaced is displayed in Figure 17. The shell script was the master program which called most of the other software and controlled most of the computational handshaking. The C++ code was the primary engine which formed the Latin hypercube sample sets. Pseudo-random number generation was accomplished by interfacing the C++ code with the well-established BOOST libraries (version 1.53.0), popularly used in linear algebra, random number, and regular expression applications. Since the actual physical distribution of the EXAFS parameters is unknown, the "worst" type of distribution was initially assumed as uniform, and then a normal distribution was extracted from the uniform over a series of iterations.

Once the Latin hypercube sample sets were generated, they were passed to the FEFFIT code [16]. The FEFFIT code was used in 1 of 2 ways. Either the parameters were fixed to their generated values, an EXAFS model was formed, and then the R-

factor was determined by comparing the model to the experimental data (Equation 56 in Chapter 4); or, the parameters in the model were free, and a non-linear least squares fit was made. The former was more useful in determining the actual physical distributions of parameters and to give a direct sampling of the correlation between different parameter dimensions. The latter was useful to observe the gradient of a parameter space and how different starting points ended with different minima.

This Latin hypercube sampling process was repeated, where each "run" was investigated with a narrowing of the bounds for each parameter. The narrowing of the boundaries was made by first making a cut against the R-factor and forming a parameter histogram resulting from the statistical cut. If the parameter distribution was still uniform, then new boundaries were established with a derivative on the lefthand and righthand side, essentially an application of Newton's method.

As an example, EXAFS data from Brookhaven National Laboratories (BNL) is analyzed. The data is from a thin metal Cu foil. A reasonable starting point for the physical structure is FCC. The Latin hypercube code is used to analyze the EXAFS data for two neighboring shells. For the analysis, the fitting parameters are: (1) the uncertainty in the photoelectric edge origin ΔE_0, (2) the *Debye-Waller* factors for the first two coordination shells σ_1 and σ_2, and (3) the uncertainty in the nearest neighbor distances $\Delta \mathrm{R}_1$ and $\Delta \mathrm{R}_2$. Assuming the FCC model is correct, the two nearest neighbor shells are combined into one parameter by introducing the lattice constant a as a fitting parameter and then adjusting R_1 and R_2 according to the relationship with the unit cell.

In Figure 18, a "first pass" is shown for the Cu lattice constant. The lattice constant is sampled 5000 times using a hypercube of 100 divisions uniformly from 3 to 4 Å. From the sampled space, theoretical EXAFS models are formed using (39) for each set of parameters and compared to the experimental data by the R-factor (56).

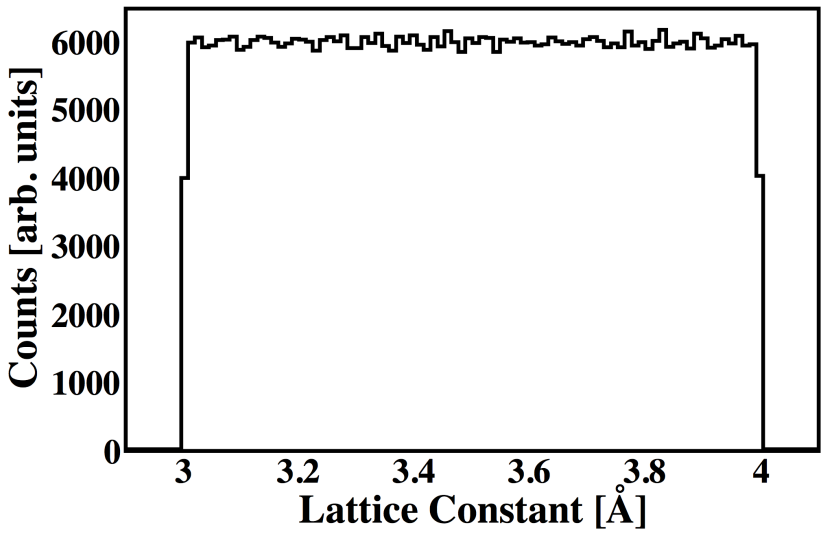

Figure 18. Cu lattice constant sampling space with 5000 runs and 100 divisions.

A cut on the R-factor of 0.5 is shown in Figure 19. The purpose of the Latin hypercube code becomes apparent in this figure as two approximately normal distributions may be observed at approximately 3.35 and 3.65 Å. This demonstrates one of the dangers of blindly fitting the EXAFS equation to experimental data, as in the case of the Cu data there is a smaller lattice constant which may result in "close" fitting parameters. Two methods of selecting the correct normal distribution at this point are to either (1) require a more rigorous statistical cut or (2) create two-dimensional parameter plots and search for mathematically stable, but physically unrealistic solutions.

The first option may result in poor resolution of the underlying distribution by removing too many sampling events. For example, making a cut on the R-factor of 0.8 at such an early stage of the Latin hypercube analysis results in only approximately 200 events out of the 500,000. In Figure 20, the second option is demonstrated by plotting the Cu lattice constant against the choice of the photoelectric edge origin. The two peaks in Figure 19 correspond to two peaks in the edge shift sampling space, creating two clearly well-confined regions that give reasonable fitting results when

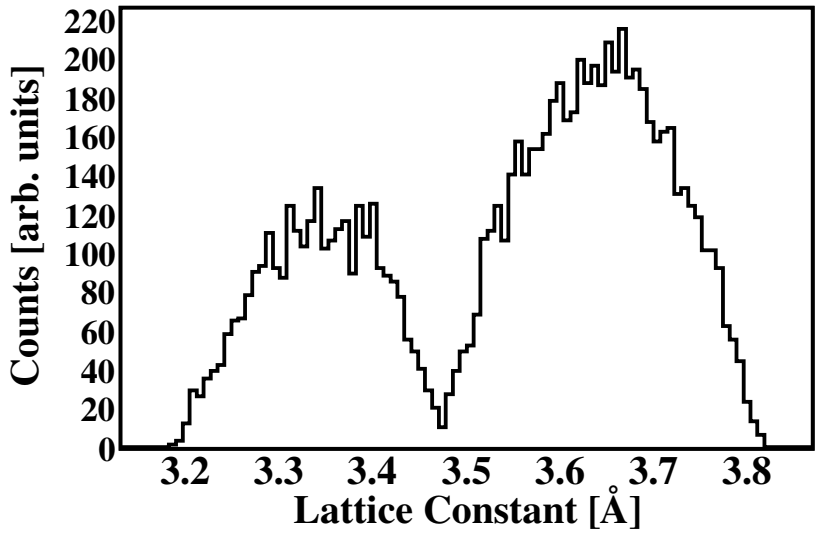

Figure 19. Cu lattice constant sampling space with 5000 runs and 100 divisions and a cut on the R-factor for events greater than 0.5.

compared to the experimental Cu EXAFS signal.

The smaller lattice constant is ruled out due to the unphysical results in the edge shift. The edge shift provides the allowed change in the initial origin guess in order to have the experimental EXAFS align with the theoretical EXAFS. Having an edge shift of nearly -30 eV results in a photoelectric origin well below the rising edge. Thus, this result, while mathematically consistent is not a reasonable physical result. Consequently, a normal curve is fit to the larger lattice constant to define a new sampling space that is no longer uniform, but a normal distribution. A similar procedure is followed for the other fitting parameters to define new sampling spaces.

A first analysis with the Latin hypercube sampling may be sufficient to determine a physical structure. In Figure 21, the best fit parameters found from the first pass are inserted into the EXAFS equation (39). The theoretical model and the experimental data have been Fourier transformed from k-space into R-space from 3.0 Å^{-1} to 10.0 Å^{-1} with a k^2 weighting. The results are surprising for a first iteration of the code, with the experimental data (black solid line) in close agreement with the

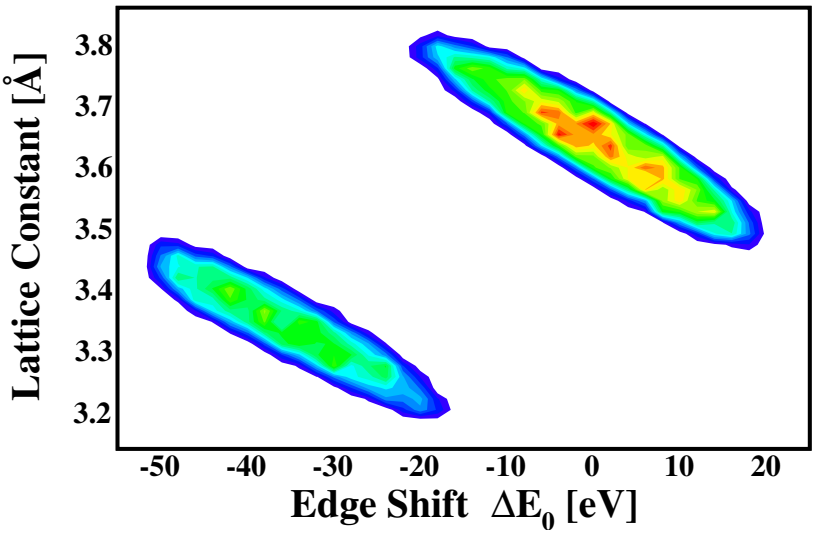

Figure 20. Cu lattice constant constant with respect to the photoelectric edge shift with 5000 runs and 100 divisions and a cut on the R-factor for events greater than 0.5.

modeled signal (dashed blue line). The first coordination shell (solid red line) is well-reproduced and the second coordination shell (solid green line) nearly so.

Some results of a second pass are plotted in Figure 22 with increasingly restrictive statistical cuts. Fitting a Gaussian to the smallest distribution gives a lattice constant of 3.64 ± 0.06 Å, where the uncertainty is the peak's full width at half maximum. The model started with an assumed lattice constant of 3.61 Å [17–19]. The photoelectric edge shift had an initial guess of 8982.56 eV, and the edge shift is determined to be 0.78 eV, resulting in a photoelectric edge origin of 8983.34 ± 6.83 eV.

In a little more than 24 hours of computational analysis (each pass taking approximately 13 hours), a respectable crystal structure has been selected out, confirming an FCC Cu structure while bypassing the days of repeating fit after fit, fixing some parameters, varying others, and attempting not to bias the results while avoiding possible false minima.

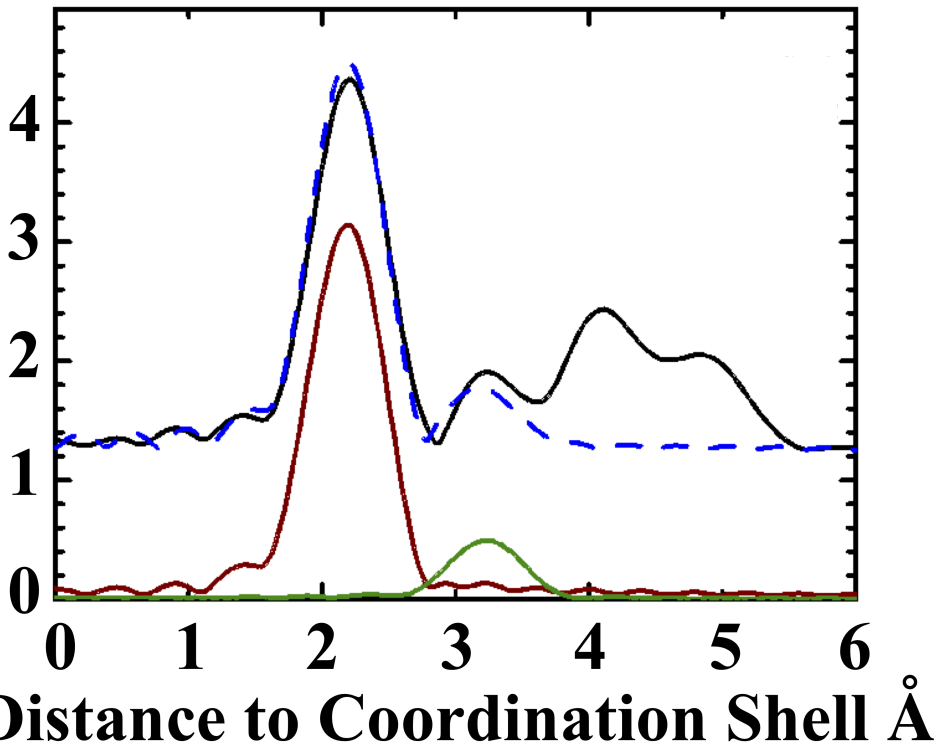

Figure 21. Modeled Cu EXAFS (dotted blue line) compared to experimental signal (black solid line). The solid red line and the solid green line below the EXAFS signals indicate the nearest neighbor and second nearest neighboring coordination shell contributions.

2.11 Green's functions as the scattering description of EXAFS and XANES

X-ray absorption fine structure spectroscopy is divided into two regimes. The x-ray absorption near edge structure and the extended x-ray absorption fine structure. The modulations in the absorption coefficient for large values of the photoelectric wavenumber ($E > 50$ eV) after the photoelectric edge have already been discussed in terms of the EXAFS. For photoelectric energies near the photoelectric edge, the spectral features are dominated more by multiple scattering events and the electronic structure.

The mathematics in this section will require Green's function formalism, of which an excellent discourse is given in the text by Stakgold [20]. Some of the Green's

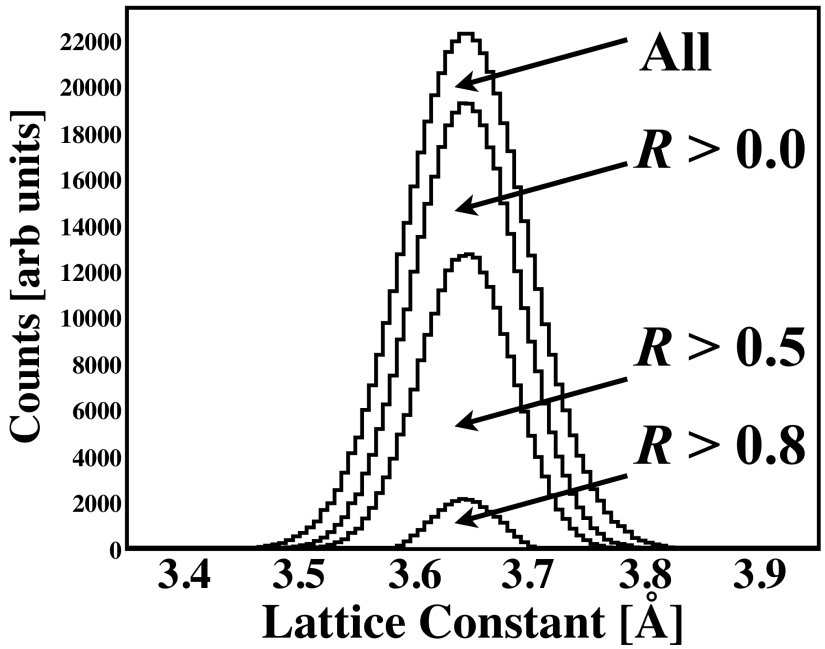

Figure 22. Latin hypercube sampling of the Cu lattice constant starting with a 100 division normal distribution, sampled for 5000 repetitions.

function formalism is discussed so that it may then be used to address Schrödinger's equation and the scattering of the photoelectric wave function described in the previous section on EXAFS. Consider in general a differential equation as given in (41), where $\hat{L}$ is a linear differential operator, $y(x)$ is a function of x for some domain (a, b) and $f(x)$ is a forcing function.

$$\hat{L}y(x) \quad = \quad f(x). \tag{41}$$

The power behind the Green's function machinery is that without directly specifying the form of $f(x)$, given that the form of the Green's function G is known, then $y(x)$ is known and may be expressed as

$$y(x) \quad = \quad \int_a^b f(x')G(x, x')dx'. \tag{42}$$

Usually, the form of $y(x)$ is solved by considering both inhomogenous $\{f(x), 0, 0\}$ and homogeneous $\{0, \alpha, \beta\}$ problems with homogenous and inhomogenous boundary conditions respectively. The solutions are summed through the superposition principle. The Green's function is found through the former with homogeneous boundary conditions, while a particular solution may be acquired from the latter.

Solving for the Green's function for a particular $\hat{L}$ is found by

$$\hat{L}G(x, x') = \delta(x - x'), \tag{43}$$

where δ is the Dirac delta function and has the sifting property [20] in that it is 0 everywhere except at $x = x'$.

The Schrödinger equation,

$$\left[\frac{-\hbar^2\nabla^2}{2m} + U\right]|\psi\rangle = E\,|\psi\rangle\,, \tag{44}$$

has the atomic potential U as a forcing function. It is generally the case that theoretical codes in XAFS solve the stationary Schrödinger equation for atomic muffin tin potentials, so U may be considered as such.

Rearranging (44) results in (45). The Green's function solution is first found for the alternative differential equation given in (46), where H_o is the free electron Hamiltonian and G_o is the free electron Green's function. This solution is then useful for describing what happens to the one-electron wave function when the potential U is introduced as the forcing term [10, 20].

$$\left[\frac{\hbar^2}{2m}\nabla^2 + \frac{k^2}{2m}\right]|\psi\rangle = U\,|\psi\rangle \tag{45}$$

$$H_oG_o = \left[\nabla^2 + k^2\right]G_o(r, r'; E) = \delta(r - r') \tag{46}$$

The Green's function solution may be written as spherically propagating wavefunctions as in (47) [9,21] . In the spatial representation, the $\pm$ superscripts represent the outgoing and incoming wave functions for the potential U. This is ideal, since XAFS concerns the propagation of a spherical wavefunction interacting with external atomic potentials U.

$$G_0^{\pm}(r, r'; k) = -\frac{1}{4\pi}\frac{1}{|r - r'|}e^{\pm ik(r-r')} \tag{47}$$

Returning to the XAFS problem, the initial state consists of a bound atomic electron and a photon with momentum $\vec{K}$ propagating in the direction $\vec{R}$. The absorption coefficient is then related to Fermi's Golden Rule for transitions and may be written as

$$\mu(\hbar\omega) = \sum_f \left| \langle \psi_f | \, \hat{\epsilon} \cdot \vec{R} e^{i\vec{K}\cdot\vec{R}} \, | \psi_{ini} \rangle \right|^2 \delta(E - \hbar\omega). \tag{48}$$

This equation is essentially the first step of the photoemission three-step model which was expressed earlier in (18) and (19). The photon in (48) is described in terms of its polarization ϵ, momentum $\hbar\vec{K}$, and energy $\hbar\omega$ and is propagating in the direction $\vec{R}$ [10].

Expanding the exponential term in a Taylor expansion, (48) can be approximated with the dipole term as

$$\mu(\hbar\omega) \propto \sum_{fin} \langle \psi_i | \, \hat{\epsilon} \cdot \vec{R} \, | \psi_f \rangle \, \delta(E - \hbar\omega) \, \langle \psi_f | \, \hat{\epsilon} \cdot \vec{R} \, | \psi_i \rangle \, . \tag{49}$$

Consequently, the density of states $n(E)$ for the energy E is given in (50) and (51), where the eigenvalues along the diagonal of the operator $\hat{G}$ contain the density of states information. The operator is formed by including completeness over the final

state wavefunctions Ψ_f and then using the identity in (52).

$$-\frac{1}{\pi}\mathrm{Im}\hat{G} = \sum_f |\psi_f\rangle\, \delta(E-\hbar\omega)\, \langle\psi_f| \tag{50}$$

$$n(E) = -\frac{1}{\pi}\mathrm{Im}\ \mathrm{Tr}(\hat{G}) \tag{51}$$

$$\delta(E-\hbar\omega) = -\lim_{\eta\to 0}\frac{1}{\pi}\mathrm{Im}\frac{1}{E-\hbar\omega+i\eta} \tag{52}$$

The absorption coefficient may the be represented in terms of the Green's function as in (53). Further discussion may be found in [10].

$$\mu(\hbar\omega) \propto -\frac{1}{\pi}\mathrm{Im}\,\langle\psi_i|\,\hat{\epsilon}\cdot\vec{R}\,G\,\hat{\epsilon}\cdot\vec{R}\,|\psi_i\rangle \tag{53}$$

The solution of the outgoing wavefunction has been shown to be a free-electron wave combined with a scattering wave due to the atomic potentials around the originating atom. If G_0 represents the freely propagating wave, then the Green's function G describing both the free-electron and the scattered electron is given in (54). The T matrix is the transition operator that describes how the source term $U\,|\psi\rangle$ is related to the solutions of the free-electrons $T\,|\phi\rangle$. T takes into account all the scattering processes off each atom around the origin of the photoelectron's central atom. The equation is a sum of no scattering (free spherical wave), one scatter, two scatters, ... etc. This is the geometric series of (55).

$$G = G_0 + G_0TG_0 + G_0TG_0TG_0 + \cdots \tag{54}$$

$$G = (I - G_0T)^{-1}G_0 \tag{55}$$

These two equations are the core of the EXAFS and XANES processes, especially for calculation. In EXAFS, considering more distant and distant coordination shells, (54) may be used to consider primarily first order scattering (to the neighboring atoms

and back), second order, and so on. Usually, for a structure with few atoms in the unit cell, such as ThO_2 and the fluorite structure, the first two coordination shells may be sufficiently investigated with EXAFS using just first order scattering. Although some of the multiple scattering will weakly contribute to the overall EXAFS modulation. For XANES, the photoelectric wave has less energy and is more sensitive to multiple scattering. In XANES, a cluster of atoms is considered and (55) is used through matrix inversion. Unlike the problem usually pursued in density functional theory, which attempts to map the entire band structure for a large material, XAFS is a local order probe and the photoelectric wave decays with increasing radial distance r from the central atom (47). Consequently, considering cluster sizes of around one hundred atoms is generally enough to attempt to calculate XANES. Such calculations are made possible with software such as FEFF 9, which is under continual development by Rehr et al. at the University of Washington [15].

References

[1] N. Ashcroft and N. Mermin, *Solid State Physics*. Brooks Cole, 1976.

[2] H. P. Bonzel, C. Kleint, M. G. Stepanova, H. Nakanishi, and V. I. Zaporozcenko, *Progress in Surface Science*, vol. 49, 1995.

[3] S. Hüfner, *Photemission Spectroscopy: Principles and Application*, 3rd ed. New York: Springer, 2003.

[4] W. Shattke and M. A. V. Hove, *Solid-State Photoemission and Related Methods*. WILEY-VCH Verlag GmbH and Co. KGaA, 2003.

[5] F. de Groot and A. Kotani, *Core Level Spectroscopy of Solids*. CRC Press Taylor and Francis Group, 2008.

[6] C. N. Berglund and W. E. Spicer, "Photoemission Studies of Copper and Silver: Theory," *Physical Review*, vol. 136, no. 4A, pp. A1030–A1044, November 1964.

[7] D. J. Griffiths, *Introduction to Electrodynamics*, 3rd ed. Prentice Hall, 1999.

[8] J. D. Jackson, *Classical Electrodynamics*. John Wiley and Sons, 1999.

[9] C. Cohen-Tannoudji, B. Diu, and F. Laloe, *Quantum Mechanics*. Hermann, Paris, France: John Wiley and Sons, 1977, vol. 1.

[10] G. Bunker, *Introduction to XAFS: a Practical Guide to X-ray Absorption Fine Structure Spectroscopy*. Cambridge University, 2010.

[11] J. J. Rehr, R. C. Albers, C. R. Natoli, and E. A. Stern, "Spherical Wave Corrections in XAFS," *Journal de Physique*, vol. 47, pp. C8–31, December 1986.

[12] T. D. Kelly, L. Kong, D. A. Buchanan, A. T. Brant, J. C. Petrosky, J. W. McClory, V. T. Adamiv, Y. V. Burak, and P. A. Dowben, *Phys. Status Solidi B*, vol. 250, p. 1376, 2013.

[13] J. J. Rehr, J. J. Kas, F. D. Vila, M. P. Prange, and K. Jorissen, *Phys. Chem. Chem. Phys.*, vol. 12, p. 5503, 2010.

[14] V. Fritzsche, "A New Spherical-Wave Approximation for Photoelectron Diffraction, EXAFS, and MEED," *J. Phys. Condens. Matter*, vol. 2, pp. 1413–1424, 1990.

[15] J. J. Rehr and R. C. Albers, "Theoretical Approaches to X-ray Absorption Fine Structure," *Reviews of Modern Physics*, vol. 72, no. 3, p. 621, July 2000.

[16] M. Newville, "IFEFFIT: interactive EXAFS analysis and FEFF fitting," *J. Synchrotron Rad.*, vol. 8, pp. 322–324, 2001.

[17] S. Grazulis, A. Daskevic, A. Merkys, D. Chateigner, L. Lutterotti, M. Quiros, N. R. Serebryanaya, P. Moeck, R. T. Downs, and A. LeBail, "Crystallography Open Database (COD): an open-access collection of crystal structures and platform for world-wide collaboration," *Nucleic Acids Research*, vol. 40, pp. D420–D427, 2012.

[18] S. Gražulis, D. Chateigner, R. T. Downs, A. F. T. Yokochi, M. Quirós, L. Lutterotti, E. Manakova, J. Butkus, P. Moeck, and A. Le Bail, "Crystallography Open Database – an open-access collection of crystal structures," *Journal of Applied Crystallography*, vol. 42, no. 4, pp. 726–729, Aug 2009. [Online]. Available: http://dx.doi.org/10.1107/S0021889809016690

[19] R. T. Downs and M. Hall-Wallace, "The American Mineralogist Crystal Structure Database," *American Mineralogist*, vol. 88, pp. 247–250, 2003.

[20] I. Stackgold, *Green's Functions and Boundary Value Problems*, 2nd ed. John Wiley and Sons, 1998.

[21] R. Shankar, *Principles of Quantum Mechanics*, 2nd ed. Springer, 1994.

III. Electronic characterization of hydrothermally grown ThO_2 single crystals using UPS, IPES, and XANES

3.1 Introduction

It is often stated that Th has no $5f$ electrons and instead adopts the electronic configuration [Rn]$6d^27s^2$. This is an extension of the consideration when Th is a cation Th^{4+} in a compound such as ThO_2. In this scheme, the valence maximum is dominated by O $2p$ character, as a result of transferring the outer Th $6d^27s^2$ electrons to the O $2p$ band below the valence band maximum (VBM). However, there exists a body of literature that suggests a hybridization between Th and O in ThO_2 with Th $5f$ (and/or $6d$) character mixing with the O $2p$ in the valence bands. This results in a fluorite structure that is not purely ionic and possesses some covalent properties.

Theory does tend to suggest hybridization of Th $5f$ (and/or $6d$) with O $2p$ [2–5]. However, the manner in which the f-band is included does have a profound effect on the theoretical calculations. For example, a fixed f-band model does not result in hybridization [2]. Resonant photoemission experiments support hybridization [6].

Like most f systems, the extent of band itinerancy is central to understanding the degree of hybridization, even in wide band gap insulators like ThO_2. The expectations regarding the ThO_2 band gap are not definitive. Theoretical calculations predict a band gap over an extensive range: 4.43 [7], 4.5 [2], 4.673 [3], 4.7 [2], 4.82 [4], 5.0 [6], and 6.9 eV [3]. Experimental work is difficult to find, and the two frequently reported values are 5.0 and 6.0 eV [5–9]. The band gap literature reports both indirect and direct band gaps. The hydrothermal growth process is capable of producing large ThO_2 single crystals suitable for resolving these electronic structure inconsistencies from spectroscopic measurements of both the occupied and unoccupied band structure.

Obtaining ThO_2 single crystals by the hydrothermal technique is challenging due to difficulties in maintaining differential heat regions necessary for stable crystal growth. However, the work of [10, 11] indicates this growth process to be an excellent means of obtaining large single crystals of refractory oxides on the order of several mm. In this chapter, starting with large single crystals of ThO_2, on the order of 9 mm^2 per face, the occupied and unoccupied band structure is extracted. The valence band is probed with UPS and compared to XANES. The conduction band is probed with IPES, and the band gap is extracted from the combined measurements.

3.2 Methodology

The ThO_2 single crystals were synthesized in supercritical CsF mineralizer solutions. The crystal structure was confirmed by x-ray diffraction (XRD) and then through the rocking curves, oriented in the (200) direction (Figure 32a in Chapter 4). Further details of the growth process and prompt structure characterization may be found in other references [10–13].

The chamber in Figure 23 has three "levels." The bottom level consists of a low energy electron diffraction (LEED) assembly and is not used in this research. Figure 24 provides a top view of the experimental setup used for the photoemission measurements. The middle level (left side of Figure 24) consists of the load lock assembly and the equipment necessary for measuring the core and valence density of states (DOS). While the detector and sources are fixed at 45 degrees with respect to each other, the sample stage may rotate allowing for depth resolved photoemission spectroscopy (Chapter 5). The top level (right side of Figure 24) contains the low-energy electron gun and a Geiger-Müller (GM) tube for the characterization of the unoccupied structure in the conduction band.

Ultraviolet photoemission spectroscopy (UPS) and inverse photoemission spec-

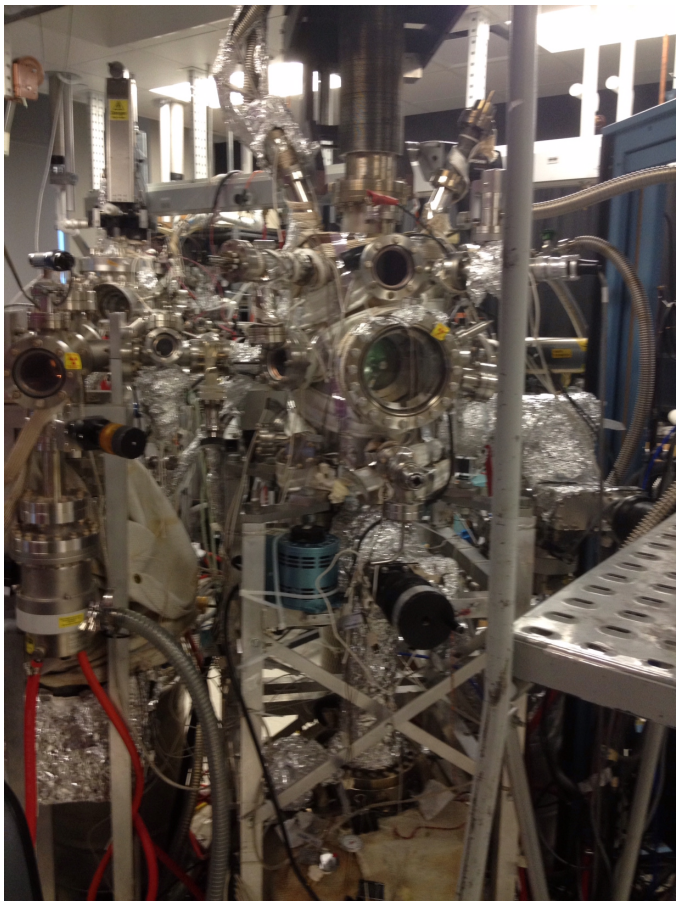

Figure 23. Experimental assembly for the photoemission measurements at the University of Nebraska-Lincoln.

troscopy (IPES) experiments were conducted under ultrahigh vacuum (UHV) conditions (10^{-10} Torr). The UPS technique was conducted using the He(I) emission line through the use of a gas discharge (arc) lamp. Photoelectrons were measured with a hemispherical analyzer with a system resolution of 100 meV. The IPES spectra were obtained using a variable low energy electron gun. A GM tube with I_2(g) was used to detect photon emission; this is typically referred to as the isochromatic measurement mode for IPES, limited by an instrumental line-width of approximately 400 meV [23, 24]. The binding energies were referenced with respect to the Fermi level (E_F) of a Au foil and reported as E-E_F, making occupied state binding energies negative. Both techniques were conducted under UHV conditions, where the American

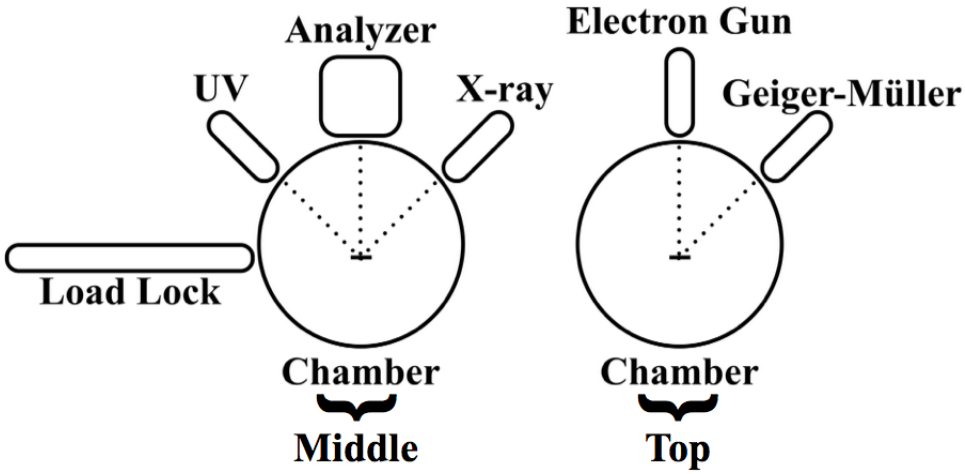

Figure 24. Schematic overhead view of the experimental setup for the photoemission techniques used in this research. The fixed angles between the sources and the detectors are 45 degrees. On the left is the "middle" level of the experimental chamber including the load lock and the devices necessary for conducting XPS and UPS measurements. On the right is the "top" level, with the equipment necessary for conducting IPES measurements.

Vacuum Society (AVS) defines the ultrahigh vacuum condition to be in the region 10^{-9} to 10^{-12} Torr.

The importance of the vacuum condition cannot be understated. Foremost, vacuum requirements ensure that sample contamination and absorption of gaseous molecules in the sample chamber remain at a minimum. Given enough time, even after sputtering to a clean surface, a C $1s$ peak may be found on a sample surface due to atmospheric gases present in the sample chamber even under UHV conditions. In addition to limiting surface absorption, the vacuum condition directly influences the mean free path of both the excitation photons and the photoelectrons. The higher the vacuum, the longer the mean free path of photons and photoelectrons within the chamber.

The vacuum chamber used for these experiments is shown in Figure 23. A crystal is mounted to the sample plate by welding Ta strips to the plate and holding the crystal in place as in Figure 25. The sample is then introduced into the chamber

from a load lock assembly. This allows the central chamber to remain under high vacuum while loading and unloading samples.

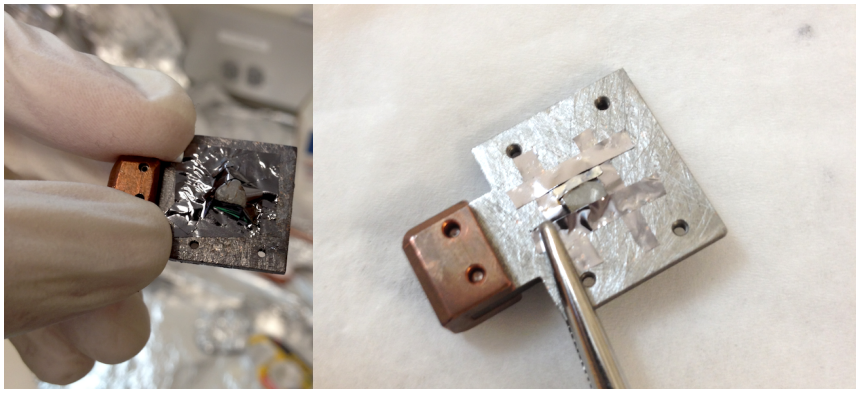

Figure 25. Examples of crystals mounted by Ta foil for photoemission studies.

The source for the UPS emission is a gas discharge lamp. While x-rays may also be used to study the valence band, the ultraviolet photoemission source provides improved energy resolution compared to x-ray photoemission. The improved energy resolution is a result of the narrow excitation line shape for the UPS source. In many cases, the FWHM of a UV source may be as low as 0.005 eV [14, 15].

Additionally, UPS has an improved sensitivity to the valence band compared to x-ray photoemission. This improved sensitivity is a direct result of the photoemission theory presented in Chapter 2. In the first step of the three-step model for photoemission, the transition probability for a bound atomic electron into a photoelectron includes a mixing matrix M_{fi} governed by the physics between an initial and final electronic state due to a perturbing potential.

For the gas discharge lamp used in this experiment, He(I) photons have an energy of 21.2 eV. Energies measured in the valence band vary, however, the first 10-15 eV below the Fermi level is common. This energy regime is closer to the 21.2 eV for UPS than a x-ray source such as Al K_α (1486.6 eV). Consequently, the initial state (bound electron + photon) and the final state (core hole + photoelectron) have comparable

energies when UPS is used over XPS.

The source for the low-energy electrons was an EGPS-1022 electron gun system. An emission current of 1.1 μA was used during the experiment. The particular method used for this measurement was the Bremsstrahlung isochromat spectroscopy (BIS) technique. Low energy electrons were emitted by the electron gun and impinged upon the sample surface. As the electrons were captured in the higher lying bands, they fell to lower conduction bands and emitted photons. These photons were detected at a fixed energy by a GM counter. In this experiment, the GM tube was filled with I_2(g) and with the CaF_2 entrance window had an ionization potential of 9.7 eV.

An example of IPES data for a Ta metal foil is plotted in Figure 26. Ta is a metal and the density of unoccupied states rises immediately after the Fermi level. A clear difference exists between the sputtered and non-sputtered surfaces. However, the rise of the unoccupied DOS still starts at the same energy. In this study, there was no means of sputtering available due to the radioactivity of ThO_2 and concerns of contaminating sample chambers at the institutions where the measurements were conducted. Thus, the spectra in this research appear similar to the "dirty" Ta foil in Figure 26, due to surface contamination. However, the gap after the Fermi edge still provides insight into where the actual unoccupied DOS begins.

In addition to these two techniques, x-ray absorption near edge structure (XANES) was used in conjunction with FEFF 9, a real space Green's function scattering code, to examine the hybridization content and unoccupied DOS. The IPES method does not follow the angular momentum selection rules that govern the photoemission techniques. However, XANES, involving atomic bound electrons, does provide a direct measure of the angular momentum character of the unoccupied bands. By selecting photoelectric edges that are of different initial angular momentum, the character of the conduction band above the band gap may be determined.

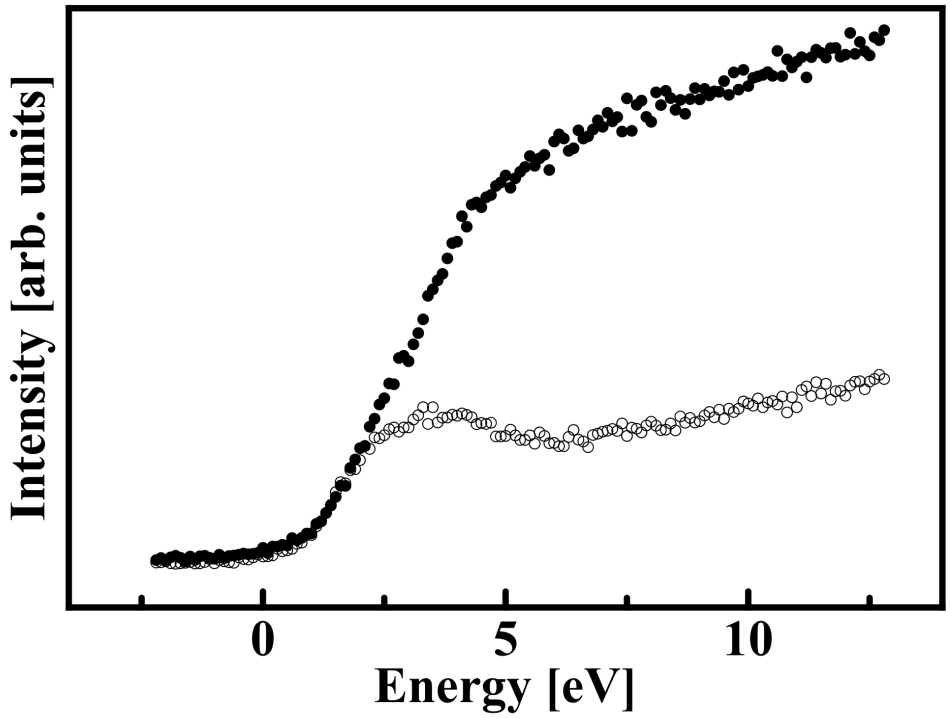

Figure 26. Inverse photoemission spectra for "dirty" Ta foil (closed circles) and sputtered clean Ta foil (open circles).

XANES was measured at the Center for Advanced Microstructures and Devices (CAMD). Thorium L-edge XANES was collected on the wiggler double crystal monochromator (WDCM) beamline in fluorescence mode using a multi-channel high purity Ge detector. Thorium M-edge XANES was collected in fluorescence mode on the double crystal monochromator (DCM) beamline using a single channel Si detector. All data were collected at room temperature. The XANES data were analyzed with the ATHENA software [16], as detailed elsewhere [17, 18].

XANES cannot be quantified in the same manner as extended absorption fine structure spectroscopy (EXAFS). However, an *ab initio* Green's functions analysis can be made via the FEFF 9 code [19, 20], and the spectra can be compared to inverse photoemission, as both probe the unoccupied DOS. The FEFF 9 software uses a relativistic Green's functions formalism and realizes a self-consistent, real-space

multiple scattering mechanism [19–22].

The FEFF 9 code computes the fine structure in the absorption coefficient through a variety of steps. First, the atomic potentials in the "free atom" state are calculated relativistically. This is done by using the relativistic Dirac-Fock formulation and idealizing the atoms as isolated from one another for a given model or cluster. Then the scattering potentials are modeled as muffin tin potentials and are allowed to overlap with neighboring atoms through a mixing term [19].

As in many density functional theory (DFT) codes, the calculations are one-electron calculations. However, the influence of many-body electron correlation effects are not ignored. In the scattering code, this is accounted for through a self-energy term. The muffin tin potentials are initialized according to the Norman radii [1] and the corresponding charge density. The atomic potentials are then calculated self-consistently, with the electronic DOS and the Fermi level calculated iteratively. After the atomic potentials and electronic DOS are calculated, the full multiple scattering calculations are made, and the phase shifts are determined [19].

3.3 X-ray absorption near edge spectroscopy (XANES)

In Figure 27, the experimental Th L_3 XANES spectrum is plotted along with various theoretical XANES spectra. Multiple calculations were made with increasingly larger full multiple scattering spheres until the model XANES converged. The full multiple scattering spheres ranged in size from the smallest sphere containing 8 atoms at a radius 3 Å to the largest full multiple scattering containing 121 atoms at a radius of 7.5 Å (one more than is shown in Figure 27). The starting point, i.e. the bottom spectrum in Figure 27 (μ_0), is the smoothly varying background for a free Th atom. Moving up Figure 27, the right hand side indicates the number of additional atoms and of what species are added into the model cluster, with increasing cluster size.

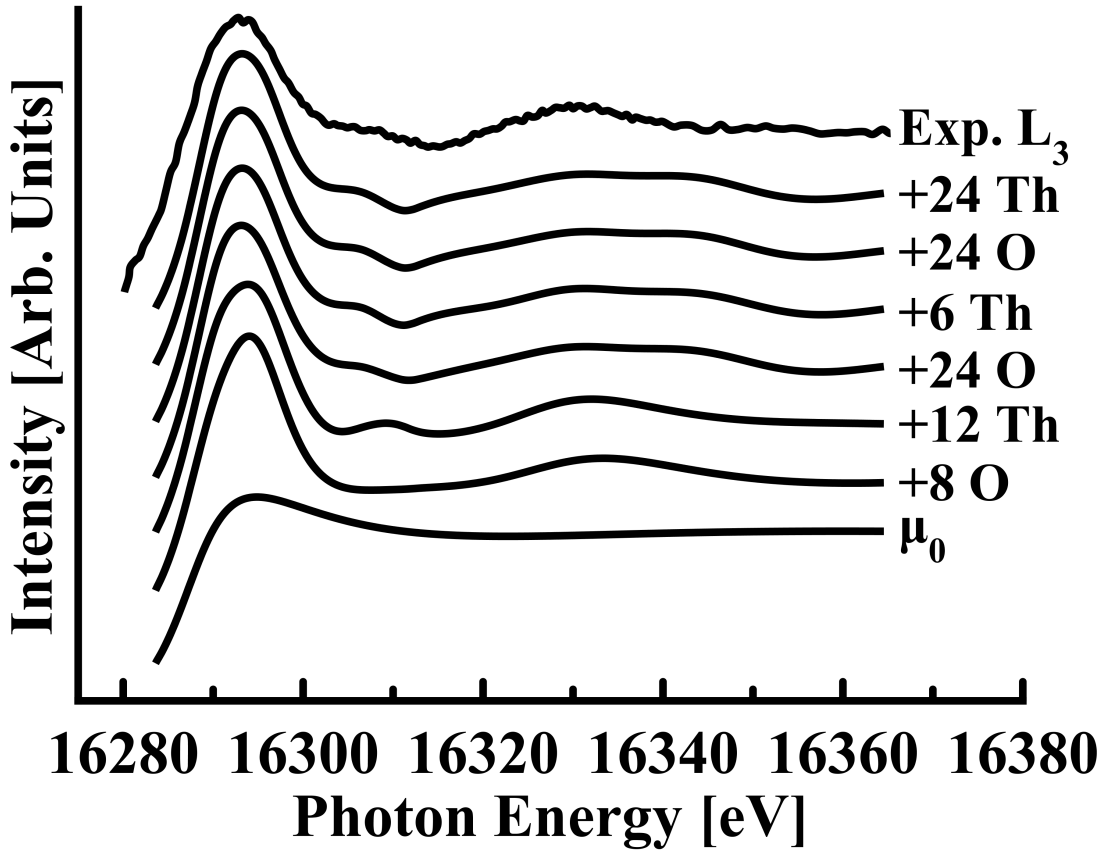

Figure 27. Theoretical Th L_3-edge XANES spectra calculated with increasingly larger full multiple scattering shells, from bottom to top (see text). The top spectrum is the normalized experimental data.

We observe that the XANES calculations converge relatively quickly after adding 32 total oxygen and 12 thorium atoms to the cluster at a full multiple scattering radius of 5.0 Å.

Despite this quick convergence at a relatively small cluster size, all the following calculations are based upon a cluster with a full multiple scattering sphere radius of 7.0 Å. Thus the local electronic DOS are the result of considering cluster sizes of approximately 99 atoms. With nearly 100 atoms in the cluster, the calculations are considered more reliable for the FEFF 9 Green's function formalism. A Hedin-Lundqvist self-energy was used for the energy dependent exchange correlation potential, and the ground state potential was used to calculate the background. Atomic potentials were calculated self-consistently using a cluster radius of 4.1 Å. The f-electrons were unconstrained and allowed to vary from their innate atomic values during the self-consistent atomic potential calculations.

The experimental data obtained at four different Th edges (L_3, M_3, M_4, and M_5) are plotted in Figure 28. The data have been shifted by E_0, the core level binding energy. This has the added benefit of being able to compare to local electronic DOS, associated with unoccupied states, particularly the d states (example [25]). The Th white line (sharp rising edge extending beyond the photoelectric edge) is compared to the Green's function calculations in a similar approach. A similar experiment was performed with amorphous actinide compounds in [26], though without calculations or band assignments.

From the dipole selection rules, the expected transitions at the L_3 and M_3 edges are from states of p character to s and d ($p \rightarrow s$ and $p \rightarrow d$). Likewise, M_4 and M_5 correspond to $d \rightarrow p$ and $d \rightarrow f$ transitions. The differences in the p and d edges are apparent in Figure 28, with the M_4 and M_5 XANES spectra rising sooner and more sharply than the L_3 and M_3 edges. The similarity between the XANES

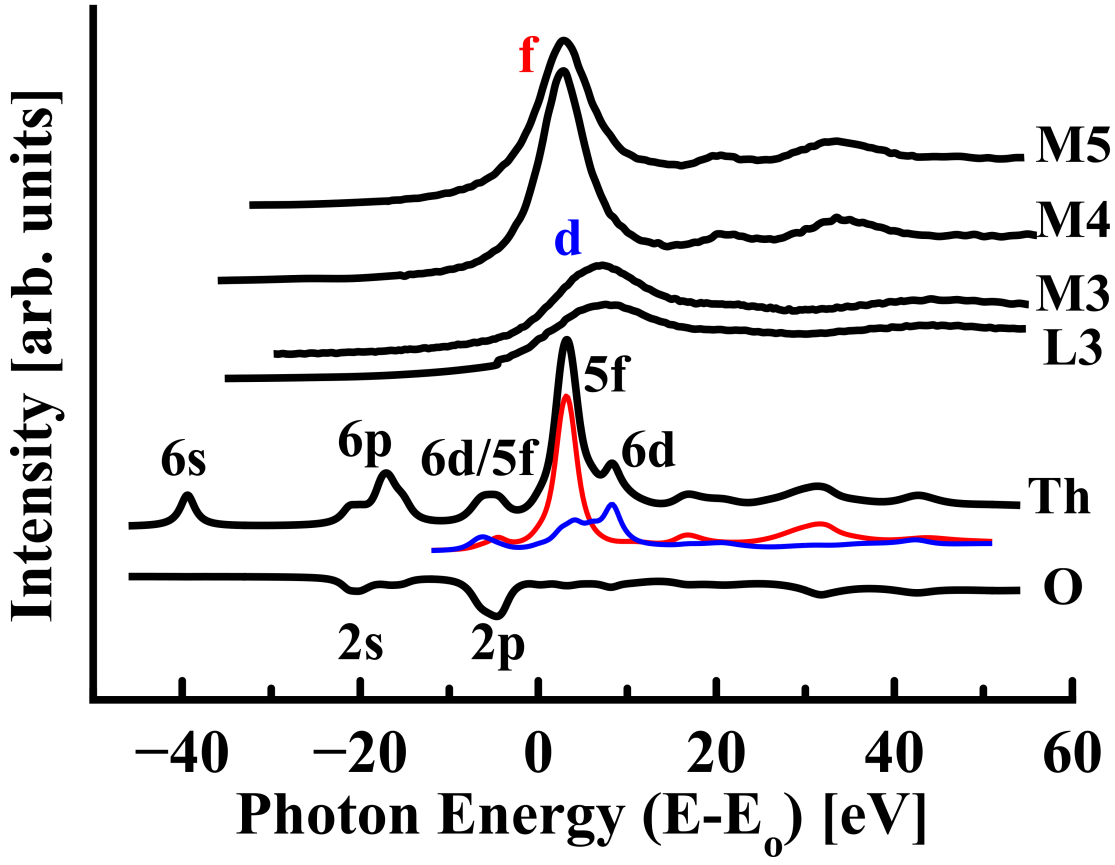

Figure 28. The experimental XANES spectra for the L_3, M_3, M_4, and M_5 edges, as labeled. The calculated total local DOS for both thorium (Th) and oxygen (O) have been plotted (black, as labeled) along with the partial Th local $5f$ (red line) and $6d$ (blue line) DOS. The oxygen DOS has been inverted for ease of identification.

data taken at the M_4 and M_5 edges reflect the dominant $d \rightarrow 5f$ transitions and the placement of the $5f$-type electron states just above the Fermi level or at the bottom of the conduction band. The similarity between the data taken at L_3 and M_3 is also expected and reflects the $2p_{3/2}$ and $3p_{3/2} \rightarrow 6d$ transitions and the placement of the d-type electrons, $2p_{3/2}$ and $3p_{3/2}$ respectively. Comparatively, the M_4 and M_5 edges correspond to $6d$-weighted electron states at binding energies farther above the Fermi level than is the case for the $5f$ states, well above the bottom of the conduction band minimum. This assignment for the unoccupied states is also reflected by our theoretical expectations.

In Figure 28, the calculated total local DOS have been plotted (black line) below the experimental data, broadened with a Lorentzian by 1.0 eV half-width at half-maximum (HWHM). The total local DOS for Th is plotted as the upper black line, whereas the total local DOS for O have been inverted for ease of comparison with the Th DOS. The partial Th local $5f$ (red line) and $6d$ (blue line) DOS have been plotted. This partial angular momentum projected local DOS also indicates that the d-character states sit at higher binding energies that those of f-character, consistent with the experimental results. We find that while there is only a very small amount of unoccupied O $2p$ weight, some Th and O s-character local DOS is unoccupied at higher energies than both Th f and d. Generally, the experimental data are well described by the Green's function calculations.

While the unoccupied band structure is composed primarily of $5f$ and $6d$ bands, with the $5f$ band just above the band gap, consistent with prior theory, hybridization is implicated in the Th $6d$, $5f$ band mixing with the occupied O $2p$ states and Th $6p$ with the O $2s$. This hybridization indicates some covalency in ThO_2 and implies that the pure ionic model is not the correct approach. The *ab initio* total charge transfer calculated is about $0.548e$ on the Th and $-0.293e$ on O, as opposed to purely ionic

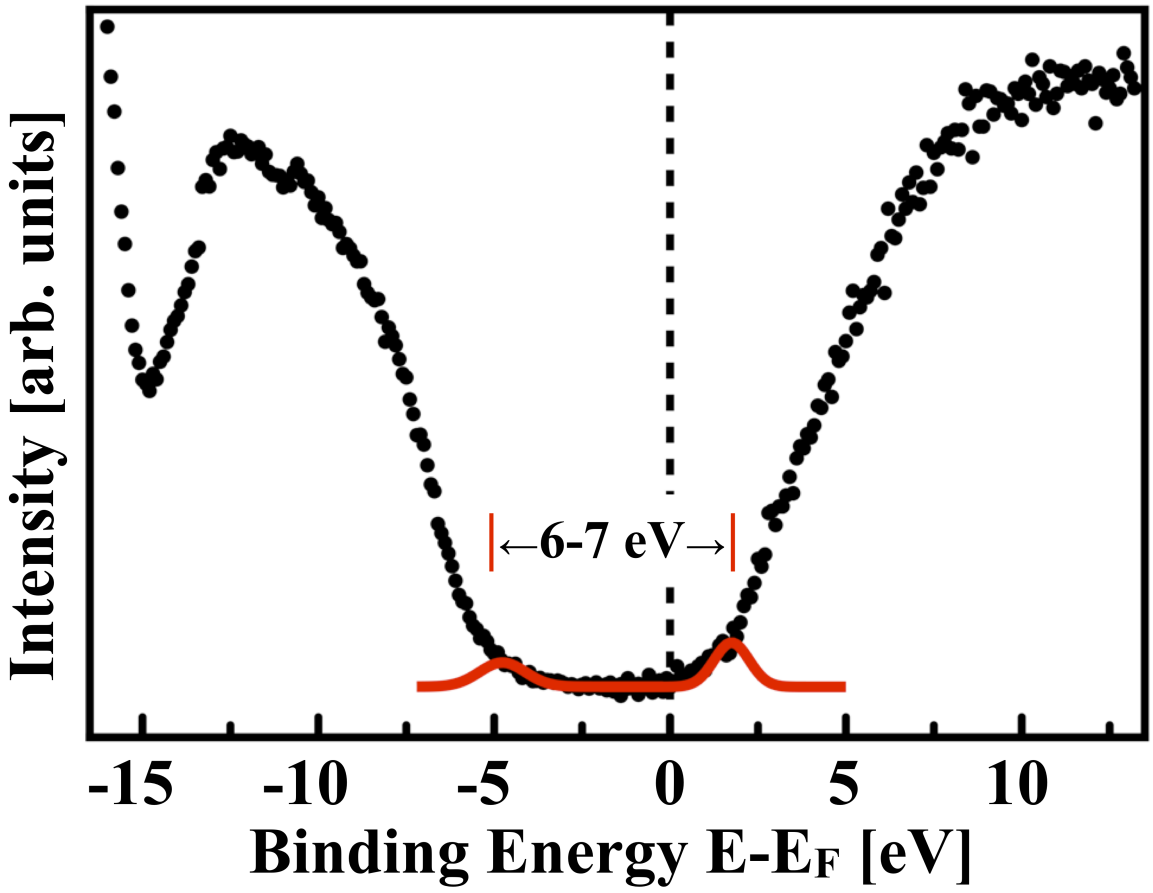

Figure 29. Ultraviolet photoemission (left) and inverse photoemission (right) spectra referenced ThO_2. Binding energies are referenced to the Fermi level as E-E_F.

$+4e$ and $-2e$ respectively. The similarity of the XANES unoccupied Th $6d$ weighted spectra (L_3 and M_3 of Figure 28) with the inverse photoemission spectra support this contention well.

3.4 UPS and IPES characterization

The UPS and IPES spectra have been plotted together in Figure 29 with respect to the Fermi level. The O $2p$ weighted DOS is apparent at approximately 5 eV below the Fermi level, matching up well the DOS plotted in Figure 28. The Fermi level is placed far closer to the conduction band edge, with the vertical $5f/6d$ starting at 1-2 eV above the Fermi level. This places the measured band gap between 6-7 eV,

close to the estimated values of 5.0 [6], and 6.9 eV [3], and in general agreement with the expected prior experimental values of 5.0 to 6.0 eV [5–9]. Given that DFT usually underestimates the band gap, the fact that most theory finds values much less than measured here is not surprising.

The unoccupied conduction band tail DOS, probed by IPES, starts at approximately 0.9 ± 0.4 eV above the Fermi level, while the O $2p$ weighted DOS band tail extends to approximately 3.9 ± 0.2 eV, below the Fermi level, so that the band gap, inclusive of the rather extensive band tail states, is smaller than the previously published band gaps (5 to 6 eV) and is instead 4.8 ± 0.4 eV. This suggests that the optical gap may be quite broad and significantly smaller than the ground state band gap. This narrowing of the band gap is possibly a result of heterogeneous mixing of defects states and surface effects. Otherwise, the inverse photoemission determined DOS (Figure 29) resembles that of the XANES spectra of Figures 27 and 28, again supporting the contention that the $5f/6d$ and O $2p$ states hybridize. Hence the electronic structure, away from the band edge tail states, is dominated by a hybridized band structure rather than localized, narrow width, isolated non-dispersive $5f/6d$ states. The photoemission resembles the fluorite phase Gd:HfO_2 alloys, with a very similar DOS [27], including extensive tail states at the valence band maximum.

As the placement of the Fermi level does not lie in the center of the gap, but rather lies closer to the conduction band edge, the combined photoemission and inverse photoemission indicate that our crystals are strongly n-type. This could occur for a number of reasons, including surface oxygen vacancies, but there are three additional ways for the growth method to lead to n-type doping of the ThO_2: (1) impurities from the growth process have diffused into the ThO_2 acting as donors, (2) Th interstitials and O vacancies in the crystal act as donor sites, (3) or the creation of anti-Frenkel point defects (the O anion moves from a lattice point leaving a hole behind), the latter

condition is expected in these fluorite structure crystals based upon DFT calculations [29, 30]. Further studies, including defect analysis by non-destructive techniques, are needed.

3.5 Conclusions

Large single crystals of ThO_2 have been investigated to characterize the valence and conduction band structure in the vicinity of the band gap. The purely ionic model for ThO_2 is clearly not ideal, but instead there is hybridization between the occupied Th $6d$ and Th $5f$ bands with the O $2p$, resulting in only partial Th-O charge transfer, in spite of the 6 to 7 eV band gap. Similarly, the unoccupied states, just above the Fermi level, are dominated by a hybridized band structure rather than localized narrow width isolated non-dispersive $5f/6d$ states. These crystals appear n-type, suggesting the presence of a small amount of oxygen point defects.

References

[1] S. D. Kelly and B. Ravel, Proc. of the X-ray Absorption Fine Structure - XAFS13 13th International Conference, Standford, July 2006.

[2] P. J. Kelly, and M. S. S. Brooks, J. Chem. Soc., Faraday Trans. 2 **83**, 1189 (1987).

[3] B. Szpunar, and J. A Szpunar, Journal of Nuclear Materials **439**, 243 (2013).

[4] R. Terki, H. Feraoun, G. Bertrand, and H. Aourag, Computational Materials Science **33**, 44 (2005).

[5] B.- T. Wang, H. Shi, W.- D. Li, and P. Zhang, Journal of Nuclear Materials **399**, 181 (2010).

[6] W. P. Ellis, A. M. Boring, J. W. Allen, L. E. Cox, R. D. Cowan, B. B. Pate, A. J. Arko, and I. Lindau, Solid State Communications **72**, 725 (1989).

[7] A. Boudjemline, L. Louail, M. M. Islam, and B. Diawara, Computational Materials Science **50**, 44 (2011).

[8] A. A. Sviridova, and N. V. Suikovskaya, Opt. Spectrosk **22**, 940 (1965).

[9] B. Szpunar, and J. A Szpunar, Journal of Physics and Chemistry of Solids **74**, 1632 (2013).

[10] M. Mann, D. Thompson, K. Serivalsatit, T. M. Tritt, J. Ballato, and J. Kolis, Crystal Growth and Design **10**, 2146 (2010).

[11] M. Mann, and J. Kolis, Crystal Growth and Design **312**, 461 (2010).

[12] J. Castilow, T. W. Zens, J. M. Mann, T. Zens, J. W. Kolis, C. D. McMillen and J. C. Petrosky, MRS Online Proceedings Library **156**, 1576 (2013).

[13] T. D. Kelly, J. C. Petrosky, J. W. McClory, T. Zens, D. Turner, J. M. Mann, J. W. Kolis, J. A. C. Santana and P. A. Dowben, MRS Online Proceedings Library **156**, 1576 (2013).

[14] P. van der Heide, X-ray Photoelectron Spectroscopy: An Introduction to Principles and Practices, John Wiley and Sons, Boboken (2003).

[15] S. Hufner, Photoemission Spectroscopy: Principles and Applications, 3rd. Ed., Springer, New York (2003).

[16] B. Ravel, and M. Newville, J. Synchrotron Rad. **12**, 537 (2005).

[17] J. Liu, G. Luo, W.- N. Mej, O. Kizilkava, E. D. Shepherd, J. I. Brand and P. A. Dowben, J. Phys. D: Appl. Phys. **43**, 085403 (2010).

[18] T. D. Kelly, L. Kong, D. A. Buchanan, A. T. Brant, J. C. Petrosky, J. W. McClory, V. T. Adamiv, Y. V. Burak and P. A. Dowben, Status Solidi B **250**, 1376 (2013).

[19] J. J. Rehr, J. J. Kas, M. P. Prange, A. P. Sorini, Y. Takimoto and F. Vila, C. R. Physique **10**, 548 (2009).

[20] J. J. Rehr, J. J. Kas, F. D. Vila, M. P. Prange and K. Jorissen, Phys. Chem. **72**, 621 (2000).

[21] A. L. Ankudinov, B. Ravel, J. J.. Rehr and S. D. Conradson, Physical Review B **58**, 7565 (1998).

[22] J. J. Rehr, and R. C. Albers, Reviews of Modern Physics **72**, 621 (2000).

[23] J. Zhang, D. N. McIlory, P. A. Dowben, H. Zeng, G. Vidali, D. Heskett and M. Onellion, J. Phys. Cond. Matter **7**, 7185 (1995).

[24] D. N. McIlory, J. Zhang, P. A. Dowben and D. Heskett, Mat. Sci. Eng. A **217/218**, 64 (1996).

[25] J. Graetz, C. C. Ahn, H. Ouyang, T. Zens, P. Rez, and B. Fultz, Phys. Rev. B **69**, 235103 (2004).

[26] J. Petiau, G. Calas, D. Petit-Maire, A. Bianconi, M. Benfatto, and A. Macrelli, Journal de Physique **47**, c*-949 (1986).

[27] Ya. B. Losovyj, I. Ketsman, A. Sokolov, K. D. Belashchenko, P. A. Dowben, J. Tang and Z. Wang, Appl. Phys. Lett. **91**, 132908 (2007)

[28] J. Xiao, C. C. Llie, N. Wu, K. Fukutani, and P. A. Dowben, Surface Science **603**, 513 (2009).

[29] Y. Lu, Y. Yang, and P. Zhang, J. Phys: Condens. Matter **24**, 225801 (2012).

[30] R. K. Behera and C. S. Deo, J. Phys: Condens. Matter **24**, 215405 (2012).

IV. ThO_2 Fluorite Structure and Defects Measured by Extended X-ray Absorption Fine Structure Spectroscopy

4.1 Introduction

Studies on the ThO_2 long range structural order have been made for decades. These studies were oriented on nuclear fuel research, high temperature structural application (alloys), solid state electrolytes (ion batteries), and lens manufacturing. The variety of the reported structural and electronic properties in the literature is an indication that the form of ThO_2 studied (e.g. thin films vs. fuel pellets) influences the result. The lattice constants reported in the literature range from 5.595 to 5.60 Å [1–5]. This implies that all forms of ThO_2 have a highly stable stoichiometric structure, unlike the behavior observed in compounds with itinerant f-electrons such as UO_2.

Despite the stable ThO_2 stoichiometry, physical properties differ depending on both the crystalline form and the measurement technique. For example, there is variation in measured vibrational parameters such as the experimentally and theoretically derived Debye temperature [5–7]. There are also differences in experimentally and theoretically determined bulk moduli, ranging from 175-290 GPa [4, 8]. It is imperative that structural research be conducted on samples of sufficient size and crystallinity for applications in electronics and optical sensors.

Obtaining single crystals of refractory oxides is difficult due to their high melting points. However, recently Mann et al. [9] have demonstrated that the growth of large single crystals is possible through the hydrothermal growth method. Crystals several mm in size for ThO_2 have been grown [9, 10]. Single crystals of this size are suitable for research and initial device engineering studies. In this chapter, the extended x-ray absorption fine structure spectroscopic technique is used to determine the local

structure around the Th atom in large single crystals of ThO_2 obtained through the hydrothermal growth process. Additionally, a novel approach to analyzing EXAFS data is presented, through the use of a Latin hypercube sampling method.

4.2 Methodology

X-ray absorption fine structure (XAFS) was measured at CAMD (Figure 30) on the WDCM beamline as discussed in Chapter 3 with the XANES technique. The Th L_3 photoelectric edge was measured, and the XAFS collected in fluorescence mode using a multichannel germanium detector. Further details on background extraction, EXAFS $\chi(k)$ data isolation, and fitting analysis may be found in similar papers [11,12] and Appendix A.

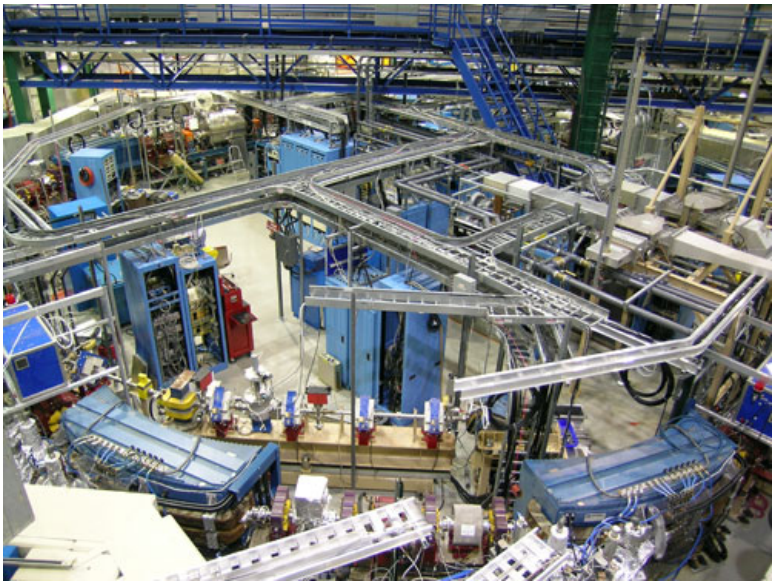

Figure 30. Overview of the Center for Advanced Microstructures and Devices, showing the bending magnets and electron synchrotron.

In most beamlines, x-ray photons are tuned to a particular energy using monochromators. The choice of the monochromator crystal (hence the d-spacing) and the angle of the crystal to the incident photon flux determines the transmitted photon

wavelengths. In this research, a downward reflecting double crystal monochromator assembly was used. Using the double crystal monochromator allowed for the photon energy to be resolved within 0.5-1.0 eV.

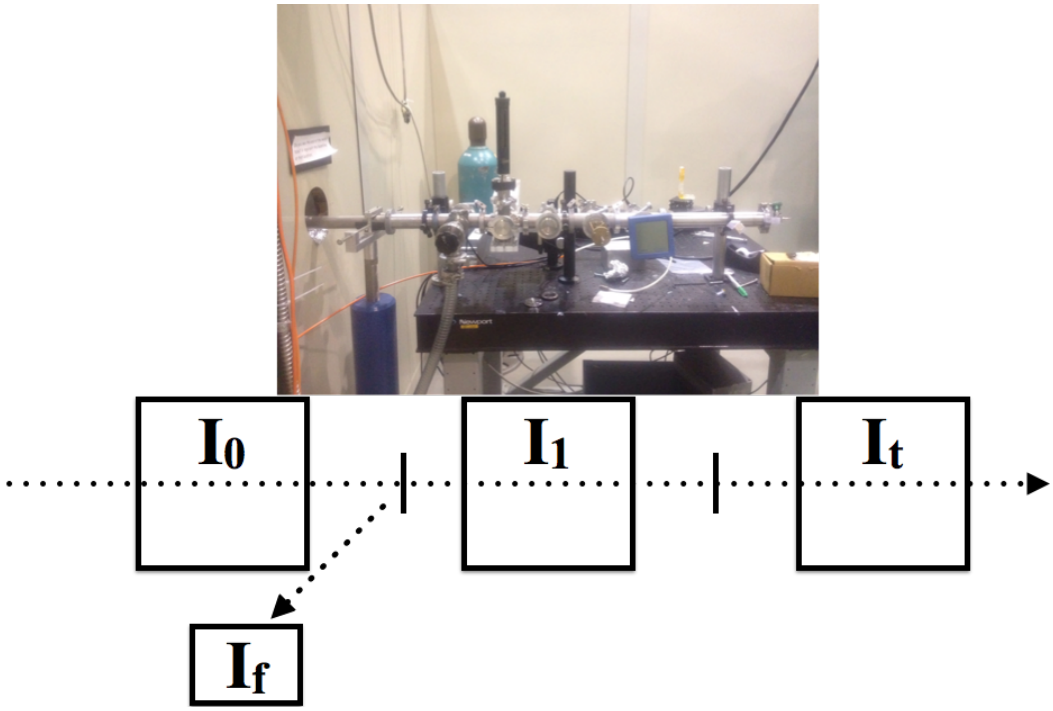

Figure 31. Schematic (bottom) of the experimental setup for the EXAFS experiment (top). The ionization chambers are I_0, I_1, and I_t. The fluorescence detector I_f is set 45 degrees off axis from the sample.

Once the photon beam had been tuned to a particular energy, it impinged on the sample in the experimental setup as in Figure 31. There were three ionization chambers (I_0, I_1, and I_t). The I_0 chamber was used to measure the incident photon flux. This was especially important at CAMD since the electron beam current was continually decaying and had to be replenished every 6-8 hours. The decay of the associated x-ray flux appeared in the experimental data as a diminishing signal intensity over the course of the measurements.

After passing through the first ionization chamber, the x-rays reach the sample. Some x-rays are transmitted through the sample, and enter into the next ioniza-

tion chamber I_1. Simultaneously, a detector placed at a 45^o angle from the sample measures the fluorescence photons emitted by the sample.

In thick samples, such as the ThO_2 crystals of this experiment, the transmitted signal is too weak to analyze. Thus, the fluorescence data is used for the measurement. In some experiments, a transmitted signal may also be used to measure a transmission through another sample which is used as a standard. The transmission for this second sample is measured in the ionization detector I_t.

The photon flux in the ionization chambers is calculated by considering the parameter W. W is the energy required to produce an electron-ion or electron-hole pair in a detector. For ion chambers, the fill gas typically will have a W value between 20-40 eV. For the DCM beamline experiment, the crystals are measured under low vacuum, and He is used as a fill gas in the chambers. He requires 41 eV to create an electron-ion pair. Based on the number of electrons created by the photon flux, the number of photons in the chambers is determined.

The first step of an EXAFS analysis requires extracting the EXAFS modulation from the XAFS signal (Appendix A). After the EXAFS is extracted, a model is developed that corresponds to the assumed underlying geometry. The model is fit to the data and fitting parameters are extracted. If the model fits the data, then the analysis is done. Otherwise, a new model is developed, and the fitting procedure repeated [13–15].

It was found in previous EXAFS analyses that fitting theoretical models to experimental data is a time intensive process, often taking weeks to months. Some difficulties include avoiding or confirming false minima in the fitting parameter spaces and avoiding experimenter bias in parameter fitting parameter adjustments. In order to address these difficulties, a Latin hypercube sampling (LHS) code was written to automatically sample a given parameter space and determine the best fitting results

while navigating mathematically consistent, but physically unrealistic solutions.

The LHS code was written in C++ and served as the means for generating the LHS sample sets. Pseudo-random numbers were generated using the well-established BOOST libraries (version 1.53.0) particularly for uniform and normal distributions. The sample sets were broken into N divisions (100 in this research) and once random numbers were drawn from each division, randomly assorted sets of parameters were assembled.

After assembling the parameter sets, the code interfaced with the iFEFFIT software [16] and compared the experimental data to the assembled theoretical EXAFS. The effective scattering amplitudes, amplitude reduction factor, and phase shifts were determined using FEFF 9 [17] and also interlaced into iFEFFIT. The FEFF calculations considered up to four scattering paths and established self-consistent potentials at a cluster size of 4.1 Å. Coordination numbers remained fixed at the fluorite lattice values of 8 and 12 for first and second coordination shells.

Once the LHS code finished an iteration, statistical cuts were made based on the number of fits against the R-factor in (56) modified from [16], where χ_{exp} and χ_{mod} are the experimental and modeled EXAFS in R-space respectively. This allowed a fitting of a normal distribution to the results, and a new sample space was created. The procedure was then repeated. This was done multiple times until it was clear that the final solution was converging for a set of EXAFS fitting parameters based upon the R-factor approaching 1.0, an idealized perfect fit between model and experiment.

$$R = 1 - \sum_{j=1}^{N} \frac{\left[\mathrm{Im}\left(\chi_{exp} - \chi_{mod}\right)\right]^2 + \left[\mathrm{Re}\left(\chi_{exp} - \chi_{mod}\right)\right]^2}{\mathrm{Im}\left(\chi_{exp}\right)^2 + \mathrm{Re}\left(\chi_{exp}\right)^2} \tag{56}$$

In the early iterations, two or more normal peaks emerged. False minima were avoided by considering 2-D contours between parameter sets and ruling out the unphysical results (such as edge shifts of ± 10 eV or greater). In the case when no normal

distribution could be found, a uniform distribution was maintained, though this was only a result in the first few iterations of the LHS code.

4.3 Fluorite structure results

X-ray diffraction was used to confirm the single crystal structure as a preliminary measurement. In Figure 32a, the XRD intensity is plotted as a function of the double angle. The miller indices for the two sharp diffraction peaks are (200) and (400) (d-spacing of 2.80 Å and 1.40 Å). Consequently, the fluorite unit cell for the single crystals was confirmed and used as the starting structural model for the EXAFS fitting.

The Latin hypercube sampling results for the lattice constant are plotted in Figure 32b. The iteration 0 is an indication of the starting conditions, a uniform distribution sampling space from 4 to 6 Å. Although the lattice constant had already been confirmed from XRD, this wider sampling space was used in order to demonstrate proof of concept and explore possible false minima in the sampling space. The subsequent iterations (1-4) in Figure 32b have error bars that represent the full width at half-maximum (FWHM) of the normal distribution. The data shown correspond to approximately 52 hours of calculation time, a very quick convergence to a solution considering the usual fitting time for EXAFS analysis.

After 4 iterations of the LHS code, the results converged for an R-factor greater than 0.90. The best fitting results in the narrowed parameter space had an R-factor of 0.95. The results for the lattice constant are plotted in Figure 32c, corresponding to the final iteration in Figure 32b. In Figure 32c, vertical dashed lines indicate the lattice constant for other ThO_2 materials found in the literature [4].

In Figure 32d, the quality of the final fitting values is demonstrated. In Table 1, the EXAFS fitting parameters are compared to results for other ThO_2 materials found

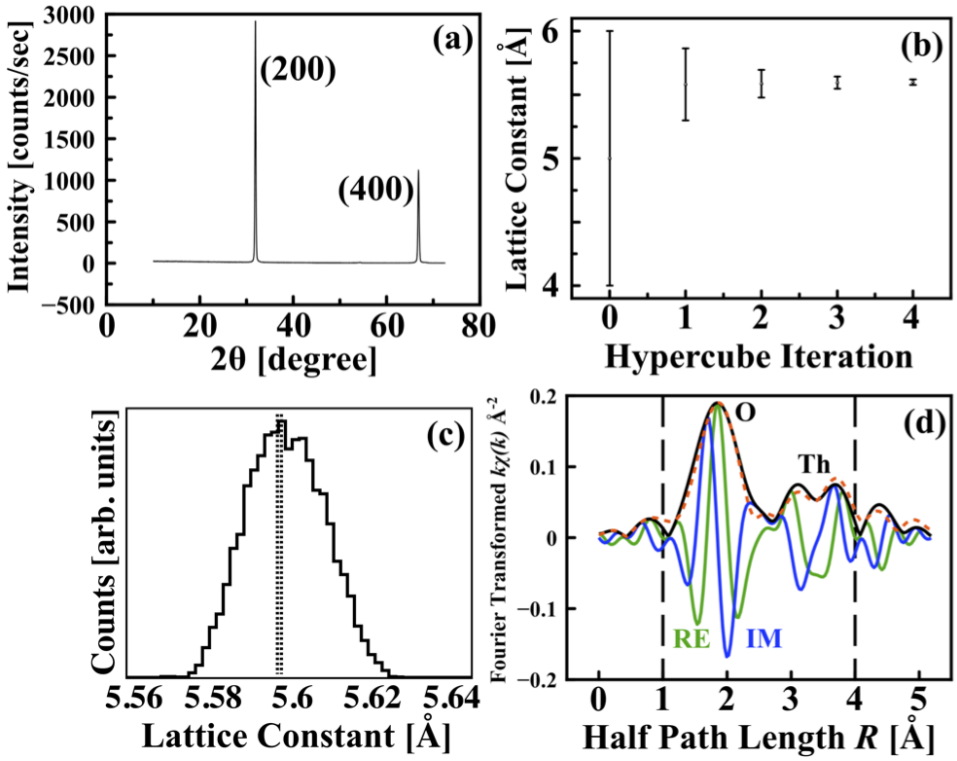

Figure 32. (a) XRD pattern of hydrothermally grown ThO_2 single crystals. (b) Lattice constant distribution for multiple iterations of Latin hypercube sampling code. Iteration 0 is uniform while 1-4 are normal. Error bars indicate FWHM. (c) Distribution of lattice constant after fourth iteration. Vertical dashed lines indicate values from XRD found in literature. (d) Result of Latin hypercube sampling. Experimental data (solid black), with real and imaginary parts (green and blue) as indicated. Theoretical model is dashed red line. Vertical lines indicate the fitting range.

in the literature. The fluorite structure is confirmed by XRD and again by EXAFS. Additionally, the Latin hypercube sampling procedure has been demonstrated as a means of significantly improving analysis time as well as accuracy by avoiding false minima and severely restricting the ability to introduce experimenter bias.

Table 1. Values for the determined EXAFS parameters. For the results of "This work", the error given is the standard deviation of the parameter distributions determined by the Latin hypercube sampling.

Shell	S_0^2	N	ΔE_0	R	σ^2	Reference
	0.917	8.0	3.79 (0.41)	2.425 (0.004)	0.004 (0.001)	This work
	1.00	6.8 (1.0)	-17.07	2.42 (0.02)	0.068	[18]
Th-O		8.0		2.424 (0.003)	0.005 (0.001)	[19]
		8.0 (1.0)	0.0 (4.0)	2.42 (0.020)	0.005 (0.005)	[20]
		5.7 (0.8)		2.45 (0.015)	0.005	[21]
	0.917	12.0	3.79 (0.41)	3.960 (0.007)	0.005 (0.001)	This work
Th-Th	1.0	10.0 (1.5)	-17.07	3.97 (0.02)	0.0581	[18]
		12.0		3.959 (0.003)		[19]

4.4 O vacancy point defects

The fluorite structure was confirmed by fitting the experimental EXAFS data in R-space and transforming the k-weighted EXAFS $k\chi(k)$ from 2.9 to 8.0 Å^{-1}. However, by extending the k-space transform into higher wave numbers, a distortion is revealed as a splitting of the O shell.

In Figure 33, the solid black line is the experimental data Fourier transformed from 2.9 to 12.0 Å^{-1}, resulting in sharper peaks as compared to Figure 32d due to the increase in Δk for the transform. The O shell at 2.425 Å has now resolved into two peaks, one at 2.425 Å and another at a shorter distance.

Recently, an O-shell splitting has been observed in work with ThO_2(aq) [22]. In that work, the O splitting was due to a competition of hydrolysis and ligation in the presence of carboxylates, changing the bonding environment of the Th cation. Similarly, the O-splitting in this single crystal research is hypothesized to be due to defect

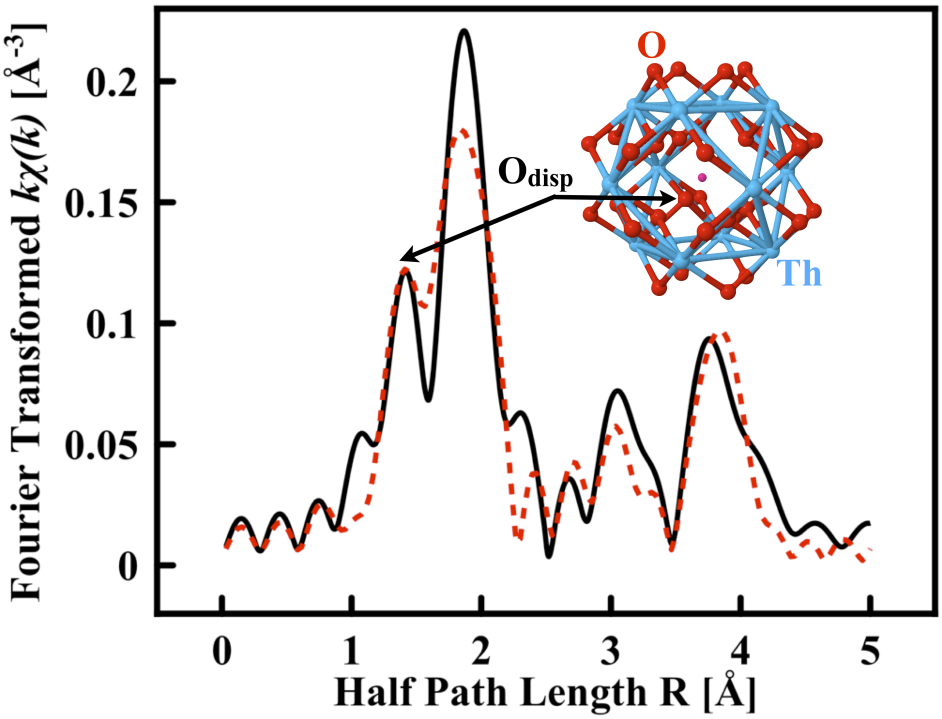

Figure 33. Experimental EXAFS data (solid black) compared with theoretical model (dashed red). Inset: Structural model for the Th-centric model.

O-coordination conditions around the Th atom in some of the unit cells. In particular, spectroscopic measurements made with ultraviolet and inverse photoemission spectroscopy (Chapter 3), suggest that the single crystals are n-type, with significant band tailing. This may be achieved by the presence of O vacancies in the fluorite lattice, serving as electron traps.

In the inset of Figure 33, a model is constructed, in which one corner of the simple cubic O lattice about the absorbing Th is allowed to shift. The Latin hypercube sampling routine was then used to map out the parameter space within the constraints of the fluorite structure previously established in Figure 32. The model with the best set of parameters (chosen by R-factor) has been plotted with a red dashed line in Figure 33, corresponding to an O shell distance of 1.82 $\pm$ 0.01 (FWHM). The agreement of the model with the experimental data is close ($R = 0.87$) in Figure 33.

This result only considers the defect model in Figure 33 and ignores the possibility that other vacancy-shift O combinations might be possible, which might improve the fit further. Different vacancy conditions are expected when moving from the surface to the bulk. The changing conditions are due to the different bonding environment on the surface as opposed to the bulk. Such O shifts are a mainstay of studies on the hyperstiochiometry uranium oxides, which typically form when UO_2 crystallizes into the fluorite structure. Often, O atoms are found shifted offsite or interstitially.

4.5 Conclusions

Large single crystals of ThO_2 have been synthesized by the hydrothermal growth technique [9]. The fluorite structure has been confirmed by both XRD and by EXAFS. The EXAFS was solved through a novel application of a Latin hypercube sampling method, which was more efficient than traditional non-linear least squares fitting methods. The analysis was successful in avoiding false minima in the fitting space

and eliminated researcher bias in parameter selection.

EXAFS is a local structure probe while XRD is a long range order measurement. While both agreed with the average fluorite structure, the EXAFS experiment confirmed the existence of local order distortions, particularly O atoms not on a traditional 1/4, 1/4, 1/4 unit cell site. With the knowledge that the single crystals are *n*-type, there are potentially a significant number of O point defects in the crystals that may act as electron traps and donor sites. These vacancies are accompanied by a change in Th-O bond length. With a decrease in bond length, there is an increased k in reciprocal space, which appears in the EXAFS oscillations.

4.6 Acknowledgements

This work was supported by the Defense Threat Reduction Agency (Grant No. HDTRA138584). The views expressed in this article are those of the authors and do not reflect the official policy or position of the Air Force, Department of Defense or the U.S. Government.

References

[1] J.-P. Dancausse, E. Gering, S. Heathman, and U. Benedict, *High Pressure Res.*, vol. 2, p. 381, 1990.

[2] U. Benedict, *J. Less-Common Metals*, vol. 128, p. 7, 1987.

[3] Eilat, Israel, 1983.

[4] J. S. Olsen, L. Gerward, V. Kanchana, and G. Vaitheeswaran, *J. Alloy. Compd.*, vol. 381, p. 37, 2004.

[5] V. Kanchana, G. Vatheeswaran, A. Svane, and A. Delin, *J. Phys: Condens. Matter*, vol. 18, p. 9615, 2006.

[6] M. Ali and P. Nagels, *Phys. Stat. Sol.*, vol. 21, p. 113, 1967.

[7] T. D. Kelly, J. C. Petrosky, J. W. McClory, T. W. Zens, D. Turner, J. M. Mann, J. W. Kolis, J. A. C. Santana, and P. A. Dowben, *MRS Online Proceedings Library*, p. 1576, 2013.

[8] M. Idiri, T. LeBihan, S. Heathman, and J. Rebizant, *Phys. Rev. B*, vol. 70, p. 014113, 2004.

[9] M. Mann and J. Kolis, *Journal of Crystal Growth*, vol. 312, p. 461, 2010.

[10] M. Mann, D. Thompson, K. Serivalsatit, T. M. Tritt, J. Ballato, and J. Kolis, *Crystal Growth and Design*, vol. 10, no. 2146, 2010.

[11] T. D. Kelly, L. Kong, D. A. Buchanan, A. T. Brant, J. C. Petrosky, J. W. McClory, V. T. Adamiv, Y. V. Burak, and P. A. Dowben, *Phys. Status Solidi B*, vol. 250, p. 1376, 2013.

[12] J. Liu, G. Luo, W.-N. Mei, O. Kizilkaya, E. D. Shepherd, J. I. Brand, and P. A. Dowben, *J. Phys. D: Appl. Phys.*, vol. 43, p. 085403, 2010.

[13] G. Bunker, *Introduction to XAFS: a Practical Guide to X-ray Absorption Fine Structure Spectroscopy.* Cambridge University, 2010.

[14] Y. Iwasawa, *X-ray Absorption Fine Structure for Catalysts and Surfaces.* World Scientific Publishing, 1996.

[15] S. D. Conradson, "XAFS: A Technique to Probe Local Structure," *Los Alamos Science*, no. 26, 2000.

[16] M. Newville, *J. Synchrotron Rad.*, vol. 8, p. 96, 2001.

[17] J. J. Rehr and R. C. Albers, "Theoretical Approaches to X-ray Absorption Fine Structure," *Reviews of Modern Physics*, vol. 72, no. 3, p. 621, July 2000.

[18] A. Bismondo, P. D. Bernardo, P. Zanonato, J. Jiang, and L. Rao, *J. Chem. Soc. Dalton Trans.*, p. 469, 2003.

[19] S. Hubert, J. Purans, G. Heisbourg, and N. Dacheux, "Local stucture of actinide dioxide and solid solutions $Th_{1-x}U_xO_2$ and $Th_{1-x}Pu_xO_2$," *Inorganic Chemistry*, vol. 45, pp. 3887–3894, 2006.

[20] Z. Wu and F. Farges, *Physica B*, vol. 266, p. 282, 1999.

[21] E. Östhols, A. Manceau, F. Farges, , and L. Charlet, *J. Colloid Interface Sci.*, vol. 194, p. 10, 1997.

[22] C. Hennig, S. Takao, K. Takao, S. Weiss, W. Kraus, F. Emmerling, M. Meyer, and A. C. Scheinost, *J. Phys. Conf. Ser.*, vol. 430, p. 012116, 2013.

V. Surface to Core-Level Shift of Hydrothermally Grown ThO_2 Single Crystals

5.1 Introduction

X-ray photoemission research has been accomplished on the actinides for the last few decades, with many studies focused primarily on U and Pu due to their importance in nuclear energy applications and the subsequent need to address waste disposal [1]. These studies generally focus on the characteristic $5f$ electrons in order to understand their role in the bonding mechanisms and how they influence electronic, magnetic, and optical characteristics.

ThO_2 is of particular interest due to the worldwide reemerging attention in the Th fuel cycle. The compound is also known for having the highest melting point of known refractory oxides [2, 3], making it useful as an alloy in high temperature applications and possibly as a high temperature neutron voltaic, despite its insulator qualities (band gap ≈ 6 eV).

Any possible application to electronic devices requires knowledge of the surface and bulk electronic structure. Photoemission spectroscopy lends itself well to such research, as it directly probes the electronic density and binding energies of a material. Thus, it is not too surprising that some photoemission studies have been made on ThO_2, with varying material quality and ligand environments [4–11]. From these studies, it is apparent that features such as the intensity of the $4f$ shake-up satellite and the core level binding energies have a significant dependence upon the material quality. For example, the shake-up satellite for Th metal oxidized to ThO_2 is almost nonexistent [4] while for solid solutions of $U_xTh_{1-x}O_2$ sintered pellets [5] the satellite intensity shows little to no correlation with fractional x.

Thus, in order to obtain baseline measurements for the bulk and surface electronic

properties, it is imperative that large single crystals of ThO_2 be obtained. However, due to the high melting point of ThO_2, obtaining large single crystals in a controlled manner is very difficult through traditional crystal growth techniques. Recently, it has been shown that the hydrothermal growth method is suitable for growing such crystals [12, 13].

5.2 Methodology

Before the XPS research in this chapter was conducted, the crystals were cleaned through a process involving ether and picric acid. An organic solution of mixed crown ether was prepared. The 15 mM crown ether solution was comprised of 0.033 g 15-crown-5 ($C_{10}H_{20}O_5$) and 0.040 g 18-crown-6 ($C_{12}H_{24}O_6$) dissolved in 10 mL of dichloromethane. A 12 mM aqueous solution of picric acid was also prepared by dissolving 0.055 g of picric acid in 20 mL of 18 MΩ water. The 10 mL crown ether/CH_2Cl_2 solution was mixed with 10 mL of the picric acid/H_2O solution in a vial. The ThO_2 crystal was added to the vial containing the 2 solutions, along with a magnetic stir bar.

The mixture was stirred vigorously for 16 hours, over which time the crown ether would scavenge any alkali cation contaminants from the surface of the crystal, with the picrate acting as a counter-ion for the complexes to remain soluble in the organic phase. The picric acid was also used in a limiting amount so that any anion contaminants could act as a counter-ion for the crown ether and be removed. After cleaning, the crystals were baked in a vacuum desiccator for approximately 16 hours at 180 ^{o}C.

X-ray photoemission spectroscopy (XPS) experiments were conducted under UHV as in Chapter 3 for UPS and IPES. Aluminum Kα emission was used for photoemission excitation. The excitation source used was a dual x-ray anode that was able to produce either Al-Kα or Mg-Kα x-rays. The Al anode was used in this research.

Photoelectrons were measured with a hemispherical analyzer with a system resolution of 100 meV [14, 15]. The binding energies were referenced with respect to the Fermi level (E_F) of a reference Au foil, and reported as E-E_F, making occupied state binding energies negative.

In x-ray production, a metal target is used as a x-ray source. The metal anode (such as Al) is bombarded with electrons (cathode) created by thermionic emission. The thermal electrons scatter inelastically with electrons in the Al foil, ejecting the Al $1s$ atomic electron. The $1s$ core hole is filled by $2p$ electrons, and the excess energy is emitted either through Auger electrons or fluorescence. In this research, the Al-Kα fluorescence results in a 1486.6 eV excitation source. The x-ray flux is maximized by accelerating the thermal electrons from the cathode to an energy an order of magnitude greater than the emission energy [16, 17]. For Al-Kα, this is 14 keV. Hence, for the experimental setup, the potential at the anode was set to 15 keV.

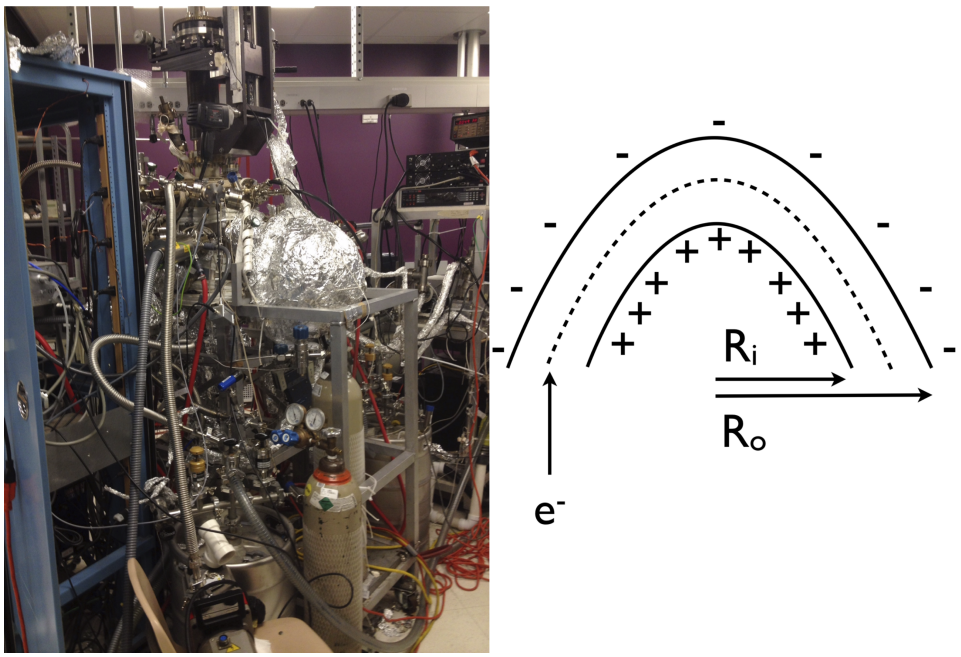

Figure 34. Back view of the photoemission vacuum chamber used in this research. The foil-covered dome is the electron analyzer. Beside the picture, a schematic of the analyzer process is shown.

The photoelectrons for both the UPS measurements (Chapter 3) and the x-ray measurements (this chapter and Chapter 6) were measured with a concentric hemispherical analyzer (or spherical deflection analyzer) as in Figure 34. The photoelectron's kinetic energy is measured by controlling the potentials between the inner and outer surface (R_i and R_o) of the analyzer [16, 17]. An electron will follow the middle dashed path of Figure 34 with an energy E_{KE} for a potential on the outer surface given by (57) and the inner surface by (58) with the equations derived in [17].

$$V_o = E_{KE}\left[2 - \frac{R_i}{R_o}\right] \tag{57}$$

$$V_i = E_{KE}\left[2 - \frac{R_o}{R_i}\right] \tag{58}$$

The energy resolution of the experiment is a function of the photon source, the line width of the photoelectric process, and the electron analyzer. Treating all three processes as Gaussian, the total energy resolution is

$$\Delta E = \left[(\Delta E_{\text{photon}})^2 + (\Delta E_{\text{photoelectron}})^2 + (\Delta E_{\text{analyzer}})^2\right]^{1/2}. \tag{59}$$

During the system work function calibration, the FWHM of a Au metal foil resulted in a total resolved energy resolution of 0.1 eV, where the dominating factor is the width of the Al-K_α.

By varying the sample surface angle with respect to the electron analyzer, the measured photoelectrons will be more or less representative of the bulk versus surface structure. In general, photoemission is a surface sensitive technique. This is due to the mean free path of the photoelectrons in the sample as they transport to the surface. In Figure 35, an atom at a depth d below the sample surface emits a photoelectron. This figure demonstrates a variety of inelastic collisions which may occur during transport,

often resulting in electrons which do not reach the analyzer for detection, as described by step two of the three-step photoemission model in Chapter 2.

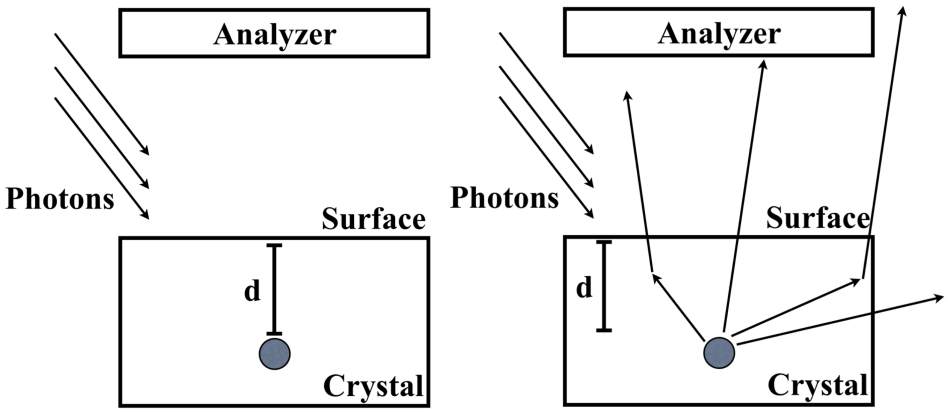

Figure 35. Schematic of the probing depth for photoemission.

Photoelectrons which are created "deep" within the crystal may not reach the surface. For the electron mean free path λ_e, the probability of escaping without inelastic collision at a depth d may be approximated by the Beer-Lambert law, where the mean free path is a function of the photoelectron's kinetic energy. The mean free path dependence upon the electron kinetic energy was observed in Figure 7 of Chapter 2. Given the mean free path of the photoelectron, probabilistically 95% of the electrons will have inelastically scattered within the distance $3\lambda_e$.

The Bethe-Bloch equation describes the energy loss of charged particles in matter [18]. A modification of the formula to include free electron plasmon losses (important for clean metal surfaces in XPS) results in the TPP-2M (Tanuma, Penn, and Powell) relation (60) [19]. In this equation, E is the kinetic energy, E_{pl} the free electron plasmon energy, and ρ the mass density. The other parameters β, C, and D are determined by empirically fitting data. All three depend upon the plasmon energy whereas β also depends upon the band gap of the material.

$$\lambda_e = E_0 \left[E_{pl}^2 \left[\beta \ln \left(0.191 \rho^{-0.5} E_0 \right) - (C/E_0) + \left(D/E_0^2 \right) \right] \right] \tag{60}$$

The paper by the authors who developed the relation did not extend calculations beyond Bi (Z=83). However, they did present results for Ta and Y_2O_3, both heavy atoms/compounds. The mean free path of a 1500 eV photoelectron is approximately 26 Å in Ta and 28 Å in Y_2O_3. ThO_2 may be estimated to be in this range, having a comparable mass and comparable number of valence electrons $N_v = 4+12 = 16$ (Ta = 8, $Y_2O_3 = 24$). From Figure 7 in Chapter 2, the estimated mean free path was 20 Å. Thus, the expected mean free path for photoelectrons of kinetic energy 1486.6 eV is between 2-3 nm.

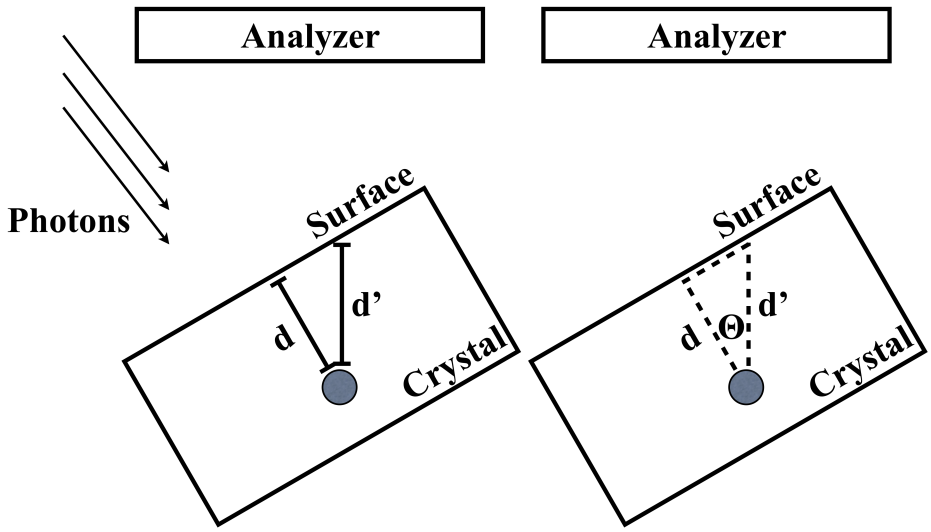

Figure 36. Angular resolution of the surface component of the crystal surface by tilting the sample with respect to the analyzer.

Since this is the sampling depth for electrons which absorb the Al-Kα photon and have 0 eV binding energy, the bound electrons within the material such as the Th $4f$ shell (330 eV binding energy with respect to the Fermi level) will have even less kinetic energy with which to reach the analyzer. Regardless, even the best case of 3 nm clearly results in a very surface sensitive spectroscopic technique. The experiment may be made even more surface sensitive by tilting the sample with respect to the analyzer and measuring photoelectrons away from the surface normal. In Figure 36,

the new distance that the photoelectrons must transport is:

$$d' = d \sec \theta. \tag{61}$$

After the experimental XPS spectra are obtained by the angular method described above, they are analyzed to extract the peak features. The XPS data are analyzed by treating the background as linear and fitting the peaks with a Gaussian-Lorentzian convolution. An example is provided in Figure 37 for the photoemission measurement of O $1s$ from a ThO_2 single crystal measured at normal incidence. Three peaks fit the experimental data, with the main peak corresponding to the O $1s$ photoemission and the other two to other elements bonded to the O.

Besides, the main photoemission peak, other peaks may appear (usually at higher binding energy) that are called satellite peaks (Appendix B). In general, there are three types of satellite peaks which appear: shake-up, shake-down, and plasmon, although others are possible. A shake-up satellite appears at a greater binding energy corresponding to a quanta of energy delivered to a valence electron which promotes it to a higher lying electronic orbital. A shake-down satellite is similar, except that a valence electron is promoted into the continuum. Plasmon peaks appear when there is a high DOS near the Fermi edge. They are characteristic of many nearly equally spaced peaks with decreasing intensity.

5.3 Carbon for charging calibration

ThO_2 is an insulator and experiences charging effects shifting spectra to higher binding energies. Some charging accounting methods include (1) the use of a flood gun, (2) depositing a thin conducting foil such as Au to be used as a reference, or (3) calibrating off the adventitious carbon peak that appears on almost all samples when

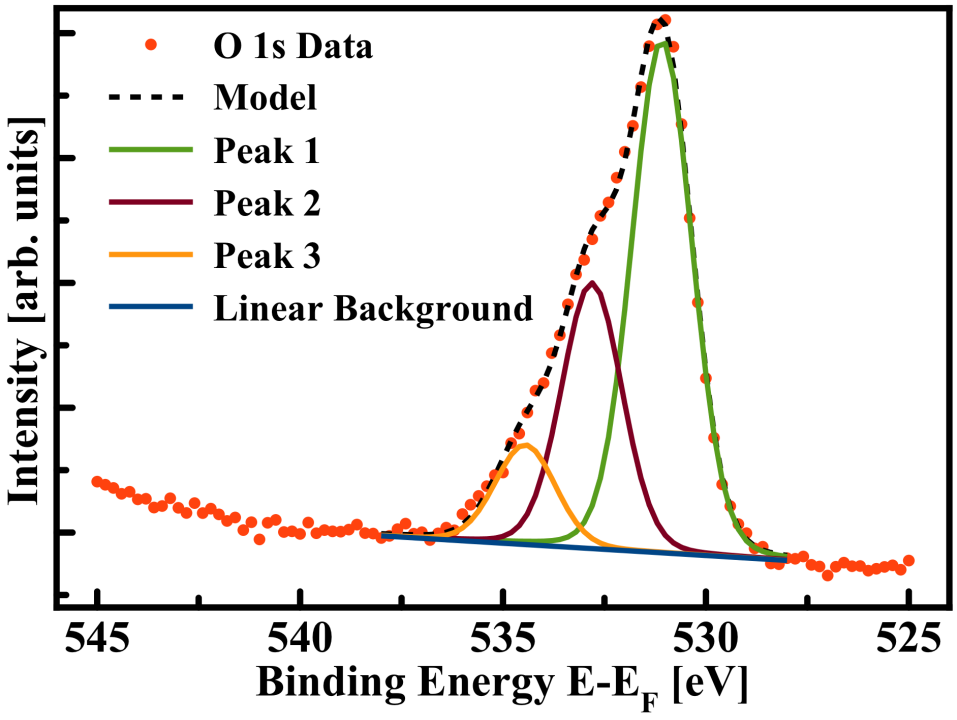

Figure 37. XPS spectrum of O 1*s* from a ThO_2 single crystal surface. Data are the closed circles. Blue line is the linear background subtraction, and three peaks with 90%-10% Gaussian-Lorentzian shape are fit to the data.

exposed to air. In this research, the C 1*s* peak was used for calibration to a value of 285.0 eV.

In Figure 38a, the XPS spectra over the angles 0°, 10°, 20°, 30°, and 40° are plotted. Peaks are marked with vertical, solid lines to represent A) carbonyl C=O contamination, B) alcohol/ether type bonds C-OH, and C) adventitious C and hydrocarbons. In Figure 38b, the most bulk (0°) and most surface sensitive (40°) angles are drawn normalized to the C 1*s* peak height. The growing surface contribution to the spectra is apparent.

Each data set has its binding energy independently adjusted for the C 1*s* binding energy with respect to 285.0 eV. For example, for the 0° emission angle, the binding energies measured were 285.23 and 286.88 eV for the main hydrocarbon and C-OH peaks respectively. The entire data set (including O and Th peaks) was then adjusted

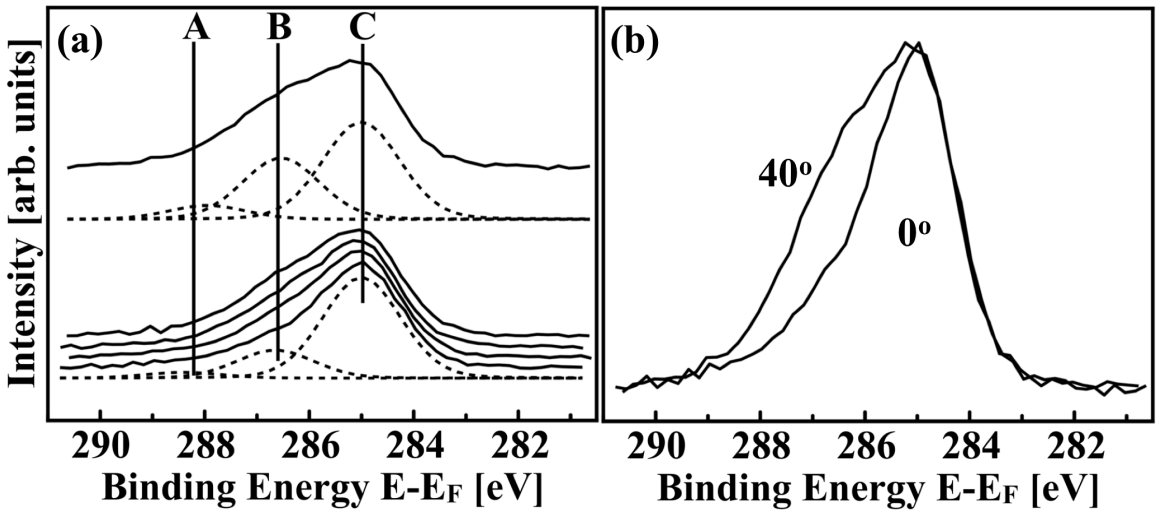

Figure 38. (a) XPS in the C 1s region as a function of take-off angle. Angles with respect to sample normal are 0°, 10°, 20°, 30°, and 40° from bottom to top. The peaks are labelled (A) C=O, (B) alcohols, and (C) adventitious C contributions. Dashed lines indicate the Gaussian-Lorentzian peak contributions for 0° (bottom) and 40° (top). (b) The bulk and surface sensitive spectra for take-off angles 0° and 40° respectively. Spectra have been normalized to C 1s peak.

by -0.23 eV, resulting in 285.0 and 286.65 eV. For a 285.0 eV calibration, the alcohol peak is generally between 286.5-286.7 eV [20], in close agreement with our result. It should be acknowledged that C 1s calibration in literature may be as low as 284.5 eV although the values 284.8 or 285.0 eV are the most common, with 284.8 eV the value used by NIST [16, 21–23].

5.4 Oxygen surface to bulk core-level shift

The results for the O bulk to surface measurements are plotted in Figure 39 as was done for C in Figure 38. An unmistakable surface sensitivity is apparent with the surface-weighted component of the spectra growing with increasing take-off angle. The main O 1s peak is found at approximately 530.9 eV, while the O-H and O-C peaks are 532.6 and 534.2 eV, agreeing well with other reported literature on ThO_2 materials.

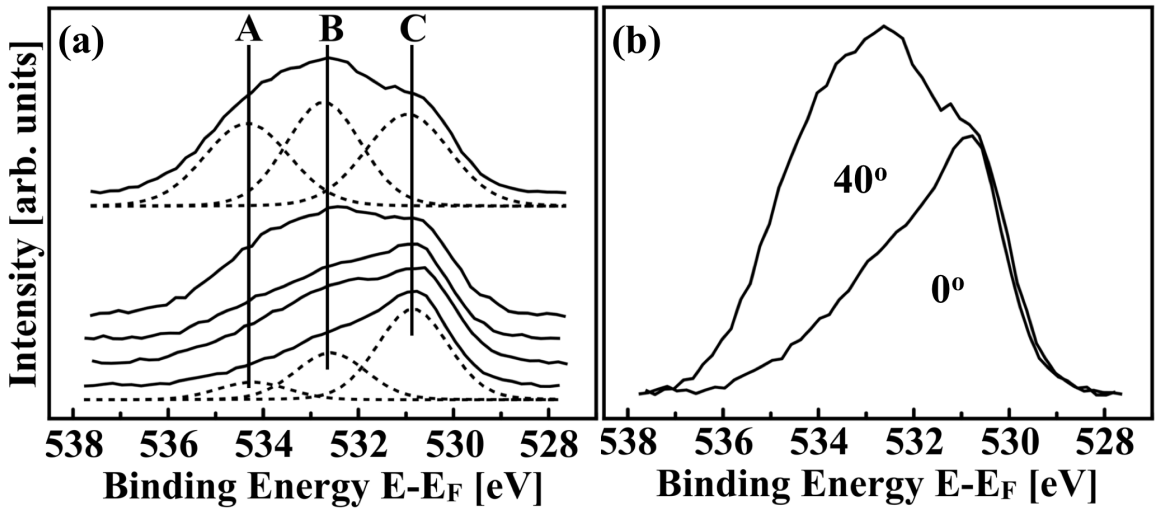

Figure 39. a) X-ray photoemission spectroscopy for ThO_2 in the O 1s region as a function of take-off angle. Angles with respect to sample normal are 40°, 30°, 20°, 10°, and 0° from top to bottom. The peaks are labelled for carbon-oxygen (A), hydroxyls (B), and (C) primary O 1s contributions. Dashed lines indicate the Gaussian-Lorentzian peak contributions for 0° (bottom) and 40° (top). Binding energies are referenced with respect to the Fermi level E_F. (b) The bulk and surface sensitive spectra for take-off angles 0° and 40° respectively. Spectra have been normalized to O 1s peak height to highlight the surface to core level shift.

5.5 Thorium surface to bulk core-level shift

The identification process of a shake-up satellite requires identifying the two electronic levels that result in the electronic excitation; in this case, the transitions from the valence band to an empty conduction band. In Figure 40a, the Th 4f region has been scanned with increasing grazing angle from bottom to top as in the case of C and O. A satellite feature has been strongly resolved. However, from fits in Figure 40a and the spectra in Figure 40b, the satellite is not well-separated from the main peaks as has been the case in all examined literature. In fact, the satellite features may be resolved into three components at 348.1, 350.8, and 352.8 eV. The satellite at 352.8 eV is approximately 7.1 eV above the main 4f peak, in agreement with other experiments.

The other two peaks are 5.1 and 2.4 eV greater in binding energy between the

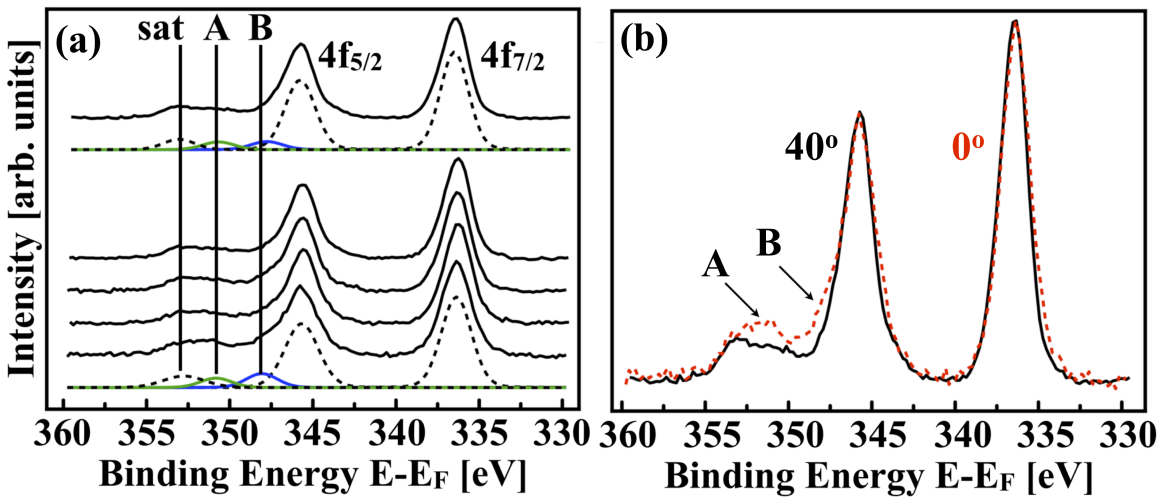

Figure 40. (a) X-ray photoemission spectroscopy for ThO_2 in the Th $4f$ region as a function of take-off angle. Angles with respect to sample normal are 40°, 30°, 20°, 10°, and 0° from top to bottom. The labelled peaks are the shake-up satellite (sat), two surface-bulk peaks (A) and (B), and the main photoemission 4f peaks. Dashed lines indicate the Gaussian-Lorentzian peak contributions for 0° (bottom) and 40° (top). Binding energies are referenced with respect to the Fermi level E_F. (b) The bulk and surface sensitive spectra for take-off angles 0° and 40° respectively. Spectra have been normalized to the Th $4f_{7/2}$ peak height to highlight the surface to core level shift. The red dashed-line is for 0° emission, while the solid black line is emission at 40°. Peaks labelled A and B correspond to those in (a).

345.7 and 352.8 eV peaks respectively. In recent experiments on the valence and conduction bands using ultraviolet photoemission spectroscopy and inverse photoemission spectroscopy, it was discovered that there was significant band tailing. The band gap was found to be between 6 to 7 eV, while an optical band gap was estimated from the tailing to be approximately 4.8 ± 0.4 eV, a characteristic of wide band gap compounds with many dopants or impurity/defect sites [24, 25].

The primary satellite line at 352.8 eV corresponds well to the reported band gap of the material, with the main peak attributed to charge transfer from the O ligand into the shifted $5f$ level to fill the hole; whereas, the satellite peak would result from charge transfer from the ligand into a higher band, screening the $5f$ hole. This process is well-documented in transition metals, with Cu halides and Cu oxides as in [26–29] and Appendix B.

Furthermore, the peak at 530.8 eV could correspond to a transition across the optical band gap due to impurities and defects in the crystal. The last peak with a difference of 2.4 eV is most likely due to surface states and the bonding with O, OH, C, and CH on the surface as in [30].

Considering Figure 40b, the intensity of the new satellite peaks depends upon the bulk and surface structure. The peaks are more intense when the bulk is probed compared to the surface. However, the strength of the underlying Th $4f$ signal with its 352.8 eV satellite remains relatively equivalent from surface to bulk. This suggests that the oxygen coordination environment influences the satellites heavily. If the peaks are the result of transferring across impurity gaps, then the presence of anti-Frenkel defects and O vacancies in the crystal could explain both the band tailings and the strength of the satellite peaks (Figure 40, peaks A and B) in the bulk versus the surface XPS spectra, as more defects of this type would be expected in the bulk.

However, the normalized main peaks' FWHM steadily decreases from bulk to surface (2.14 eV in bulk and 1.99 eV on the surface for $4f_{7/2}$). The main line is slightly more intense in the bulk than on the surface. This would agree with a changing O coordination environment and fewer Th-O bonds. In this case, the satellites could have reduced intensity if the ligands are not shielding as effectively on the surface so that they allow the creation of two-hole core states. This could be further influenced by the presence of the O-H and O-C bonds observed in Figure 39.

5.6 Conclusions

Large single crystals of ThO_2 have been investigated for their surface and bulk properties using x-ray photoemission spectroscopy. A strong satellite was observed for the main satellite peak at 352.8 eV that was relatively insensitive from bulk to

surface. However, two new peaks were observed at 350.8 and 348.1 eV that could be due to donor-like defects in the crystal lattice.

One possible solution to extracting the origin of these peaks would be to use resonant photoemission spectroscopy across the Th $4f$ edge. If the peaks are due to transitions between energy levels, then Auger-like emissions from the resonance technique should enhance the peaks. If the satellite peaks are the result of a shake up, then this implies that the operational band gap for the hydrothermally grown ThO_2 may be carefully engineered through the introduction of defect and impurity states by controlling the growth conditions, both in the bulk and on the surface.

5.7 Acknowledgements

This work was supported by the Defense Threat Reduction Agency (Grant No. HDTRA138584) and the Nebraska Materials Research Science and Engineering Center: Quantum and Spin Phenomena in Nanomagnetic Structures (NSF - DMR-0820521). The views expressed in this article are those of the authors and do not reflect the official policy or position of the Air Force, Department of Defense or the U.S. Government.

References

[1] I. A. E. Agency, "IAEA Nuclear Energy Series No. NF-T-3.8," IAEA, Tech. Rep., June 2011.

[2] J. Castilow, T. W. Zens, J. M. Mann, J. W. Kolis, C. D. McMillen, and J. Petrosky, *MRS Online Proceedings Library*, 2013.

[3] R. Riedel and I. Chen, Eds., *Ceramics Science and Technology*. Weinheim: WILEY-VCH Verlag GmbH and Co. KGaA, 2008, vol. 1.

[4] B. W. Veal, D. J. Lam, H. Diamond, and H. R. Hoekstra, "X-ray photoelectron-spectroscopy study of oxides of the transuranium elements Np, Pu, Am, Cm, Bk, and Cf," *Physical Review B*, vol. 15, p. 2929, 1977.

[5] S. Anthonysamy, G. Panneerselvam, S. Bera, S. V. Narasimhan, and P. R. V. Rao, *J. Nucl. Mat.*, vol. 281, p. 15, 2000.

[6] S. Dash, A. Singh, P. K. Ajikumar, H. Subramanian, M. Rajalakshmi, A. K. Tyagi, A. K. Arora, S. V. Narasimhan, and B. Raj, "Synthesis and characterization of nanocrystalline thoria obtained from thermally decomposed thorium carbonate," *Journal of Nuclear Materials*, vol. 303, pp. 156–168, 2002.

[7] M. O. Krause, R. G. Haire, O. Keski-Rahkonen, and J. R. Peterson, *Journal of Electron Spectroscopy and Related Phenomenon*, vol. 47, p. 215, 1988.

[8] G. C. Allen, S. Hubert, and E. Simoni, *J. Chem. Soc. Faraday Trans.*, vol. 91, p. 2767, 1995.

[9] R. J. Thorn, *J. Phys. Chem. Solids*, vol. 43, p. 571, 1982.

[10] G. M. Bancroft, T. K. Sham, and S. Larsson, *Chem. Phys. Lett.*, vol. 46, p. 551, 1977.

[11] J. J. Pireaux, J. Riga, E. Thibaut, C. Tenret-Noël, R. Caudano, and J. J. Verbist, *Chem. Phys.*, vol. 22, p. 113, 1977.

[12] M. Mann, D. Thompson, K. Serivalsatit, T. M. Tritt, J. Ballato, and J. Kolis, *Crystal Growth and Design*, vol. 10, no. 2146, 2010.

[13] M. Mann and J. Kolis, *Journal of Crystal Growth*, vol. 312, p. 461, 2010.

[14] J. Zhang, D. N. McIlroy, P. A. Dowben, H. Zeng, G. Vidali, D. Heskett, and M. Onellion, *J. Phys. Cond. Matter*, vol. 7, p. 7185, 1995.

[15] D. N. McIlroy, J. Zhang, P. A. Dowben, and D. Heskett, "Mat. Sci. Eng. A," vol. 217/218, p. 64, 1996.

[16] P. van der Heide, *X-ray Photoelectron Spectroscopy: An Introduction to Principles and Practices.* Boboken: John Wiley and Sons, 2012.

[17] S. Hüfner, *Photemission Spectroscopy: Principles and Application*, 3rd ed. New York: Springer, 2003.

[18] T. Kelly, "Temperature Studies of the CMS Pixel Detector's Capacitor Calibration Mechanism," Master's thesis, University of Nebraska-Lincoln, Dec 2009.

[19] S. Tanuma, C. J. Powell, and D. R. Penn, "Calculation of electron inelastic mean free paths (IMFPs) VII. Reliability of the TPP-2M IMFP predictive equation," *Surf. Interface Anal.*, vol. 35, p. 268, 2003.

[20] J. C. Rivière and S. Myhra, Eds., *Handbook of Surface and Interface Analysis: Methods for Problem-Solving.* Boca Raton: CRC Press, 2009.

[21] C. A. Tolman, W. M. Riggs, W. J. Linn, C. M. King, and R. C. Wendt, *Inorg. Chem.*, vol. 12, p. 2770, 1973.

[22] P. Swift, *Surf. Interface Anal.*, vol. 4, p. 47, 1982.

[23] *NIST X-ray Photoelectron Spectroscopy Database Version 4.1.* Gaithersburg: National Institute of Standards and Technology, 2012.

[24] P. V. Mieghem, *Reviews of Modern Physics*, vol. 64, p. 755, 1980.

[25] Y. B. Losovyj, I. Ketsman, A. Sokolov, K. D. Belashchenko, P. A. Dowben, J. Tang, and Z. Wang, *Appl. Phys. Lett.*, vol. 91, p. 132908, 2007.

[26] M. S. Hegde, *Bull. Mater. Sci.*, vol. 2, p. 271, 1980.

[27] K. S. Kim and N. Winograd, *hem. Phys. Lett.*, vol. 31, p. 312, 1975.

[28] S. Hüfner, *Solid State Com.*, vol. 47, p. 943, 1983.

[29] F. de Groot and A. Kotani, *Core Level Spectroscopy of Solids.* CRC Press Taylor and Francis Group, 2008.

[30] M. Breysse, B. Claudel, L. Faure, and M. Guenin, *J. of Coll. Inter. Sci.*, vol. 70, p. 201, 1979.

VI. The Debye Temperature of Hydrothermally Grown ThO_2 Single Crystals

6.1 Introduction

This work was previously published in [1] and has been reprinted with permission per Cambridge University Press guidelines. Actinides and their oxides are important for the nuclear fuel cycle and other new energy sources [2]. In particular, there is growing interest in a Th fuel cycle due to the natural abundance, refractory nature, and potentially limited radioactive waste formation [3]. While refractory suggests high temperature stability, a low Debye temperature translates into low barriers to surface and grain boundary segregation of impurities, as well as a possible propensity for phase separation, as in the case of Gd-Ni [4]. A Debye temperature of ≈ 600 K or more generally implies that surface segregation must be thermally activated, or that significant radiation damage and vacancy creation must occur prior to facile surface and grain boundary segregation of impurities.

While the technique of hydrothermal crystal growth is not new, hydrothermally grown single crystals of ThO_2 are an excellent route for obtaining large single crystals of actinide oxides, sufficient for an accurate determination of the effective Debye temperature as well as possible differences in the surface and the bulk Debye temperatures [5]. The XPS determined Debye temperature is also useful in elemental specific studies in order to help ascertain if dopants occupying similar sites within a host matrix form similar types of bonds [6]. Additionally, the changes in the effective Debye temperature are a useful signature in quantifying and identifying phonon mediated transitions [7] from temperature dependent photoemission studies [8].

The investigations here are aimed at addressing whether ThO_2 is robust as a single crystal, especially with regard to impurity and vacancy diffusion, in spite of

prior measurements that suggest that the Debye temperature of ThO_2 is in fact quite low, in the region of 259 to 290 K [9].

6.2 Experiment

ThO_2 single crystals were prepared by the hydrothermal technique in supercritical cesium fluoride mineralizer solutions. Due to the corrosive nature of the mineralizer solution, the reaction was performed in a sealed silver ampoule (Stern Leach, 99.99%) with an inner diameter of 3/8" and an overall length of 8". Thorium oxide (Strem, 99.99%) powder weighing 1.3 g and 4 mL of 6 M CsF (Alfa Aesar, 99.99%) were added to the silver ampoule, which was then welded shut. The ampoule was placed in a 27 mL Inconel autoclave with excess water added to the remaining volume of the vessel. This excess water acts as counter pressure to prevent the ampoule from rupturing during the growth cycle. Once the autoclave was sealed, two band heaters were applied with a top and bottom temperature of 690 and 750^o C respectively. The result is 20 kpsi of pressure on the ampoule. The applied conditions were sufficient to spontaneously nucleate single crystals of ThO_2 from a supersaturated mineralizer solution. Crystal formation occurred over an 11 day growth period, at which time the autoclave was allowed to cool to room temperature. The silver ampoule was retrieved from the autoclave and the contents flushed onto filter paper with deionized water. Further growth information is detailed in [10, 11].

The XPS was conducted under ultra high vacuum (10^{-10} Torr) using an aluminum anode with a Kα of 1.486 keV. All the photoemission spectra reported here were taken with this photon energy, with the photoelectron energy distribution curves measured using a hemispherical electron energy analyzer from Thermo VG Scientific, model VG 100 with a pass energy of 100 eV in 0.1 eV steps. The Th $4f$ core level binding energies are references to the Fermi level or chemical potential, calibrated using a Au

foil. The temperature was monitored using a type K thermocouple and cross-checked using an infrared pyrometer.

6.3 Core level binding energies and valency

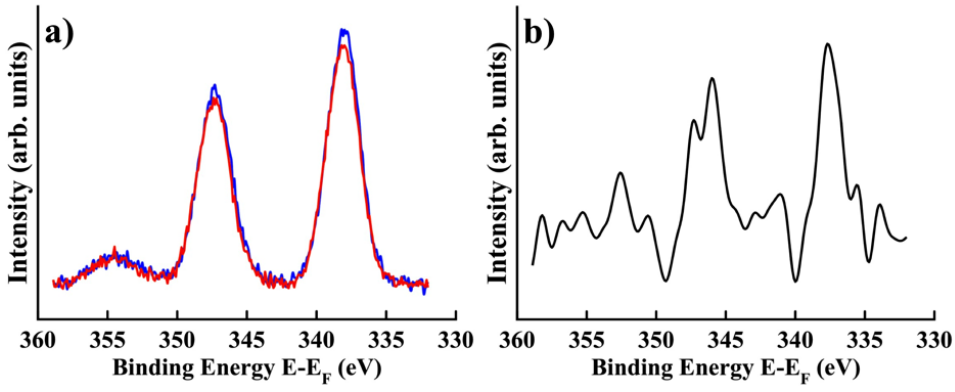

Figure 41. a) XPS of the Th $4f$ levels at 294 (blue) and 354 K (red). b) The difference between the two spectra in a). This difference has been smoothed to more accurately show the peaks. The binding energies of each peak in the figures are at 337.2 eV ($4f_{7/2}$), 346.4 eV ($4f_{5/2}$) and 353.4 (satellite).

The Th $4f$ core level binding energies taken at a temperature of 294 $\pm$ 2 K are plotted in Figure 41a. Both core level $4f$ spin-orbit component core level features are readily apparent with binding energies of 337.2 eV ($4f_{7/2}$) and 346.4 eV ($4f_{5/2}$). The intensity ratio of $4f_{5/2}$ to $4f_{7/2}$ is 0.76, close to the expected 0.75 for the angular momentum degeneracy. The metallic Th $4f_{7/2}$ binding energy ranges from 333.1 eV [12–14] to 333.8 eV [15]. The shift of the Th core level peak into a higher binding energy, providing evidence of an oxidize Th, is as expected: the previously reported value of the $4f_{7/2}$ binding energy for ThO_2 is 337.70 eV [16], close to our measured value, although some values for the $4f_{7/2}$ binding energy for ThO_2 are somewhat smaller [17, 18].

Additionally, there is a shake-up satellite peak at a binding energy of approximately 353.4eV. Satellite features are well known [8, 17–19] and a shake-up satellite

of about 7 eV is consistent with a band gap of about 6 eV for this oxide [19]. The presence of the satellite feature implies that there is the possibility of more than one final electronic state for the XPS process [8, 17–19]. In this case, if one assumes a metal-ligand picture, then the main line would occur due to a charge transfer from the O ligands, while the satellite peak results from a final state much like the initial state. This is the view approached by Allen et al. [18] for studies on various thorium binary compounds, with some variability due to changes in crystal symmetry for the various compounds studied in that work.

6.4 Effective Debye Temperature

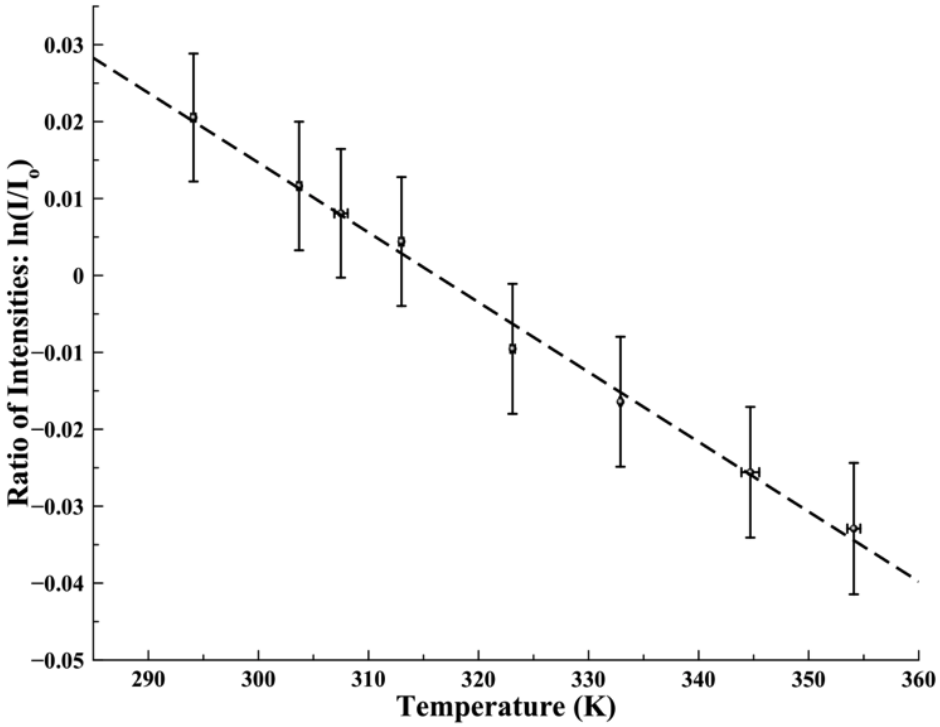

Figure 42. The natural logarithmic ratio of intensities for the $4f_{7/2}$ peak as a function temperature. A linear background was subtracted. The reference intensity I_o is the intensity for the first measurement made at 294.1 K.

The Debye temperature must be significant because the diminution of the XPS

intensities with temperature is quite slight as shown in Figure 41. In Figure 41a, the intensity of the lowest temperature (blue) is plotted with the intensity of the highest temperature (red). In order to magnify the difference, a smoothed-difference between the two spectra is plotted in Figure 41b. After background subtraction, as in Figure 41, the relative core level intensities, relative to the $4f_{7/2}$ intensity at 294.1 K, have been plotted in Figure 42. The errors in the relative intensities are propagated errors, largely dominated by counting statistics, while errors in the temperature will be largely systematic. A linear background has been removed from the intensities before the natural logarithmic ratio is determined.

The observed decrease in intensity with increasing temperature is generally attributed to an increase in the atomic vibrational motion normal to the sample surface and represented by the Debye-Waller factor W (62). By measuring the natural logarithmic ratio of intensity as a function of temperature, the slope can be determined and the effective Debye temperature extracted as has been done in many papers and texts previously [5, 6, 8, 20]. In fact we can extract a Debye temperature from the photoemission intensity as in (62) and (63), where I_o is the reference photoemission intensity, W is the XPS *Debye-Waller* factor, Δk is the change in momentum, m is the element mass, k_B is Boltzmann's constant, and θ_D is the Debye temperature.

$$I = I_o e^{-2W} \tag{62}$$

$$W = \frac{3\hbar^2 T \left(\Delta k\right)^2}{2mk_B\Theta_D^2}. \tag{63}$$

The results of our experimental determination of the effective Debye temperature are tabulated in Table 2. There is a slightly different Debye temperature determined for the $4f_{5/2}$ compared to $4f_{7/2}$, though this is primarily attributed to a small overlap between the Gaussian peaks used to fit the $4f_{5/2}$ and satellite peaks. The present

conclusion is that the two Debye temperatures are essentially in agreement, with more confidence arising from the values obtained from $4f_{7/2}$ core level intensities due to the greater coefficient of determination (R^2) in Table 2. The two Debye temperatures can be considered in agreement with much more confidence in the values attributed for the $4f_{7/2}$ peak. This is, of course, the thorium weighted effective Debye temperature and does not include a strong weight from the oxygen ligand nor does this value include anharmonic contributions.

Table 2. The fitting results for the two core 4f level and satellite peaks. Any values given in parentheses are standard deviations and provided to ascertain parameter uncertainty.

	Debye-Waller factor W	Δk $\left(\mathring{A}^{-1}\right)$	Debye temp Θ_D (K)	Fit R^2
$4f_{7/2}$	0.0009 (0.00003)	17.1	468 (8)	0.9906
$4f_{5/2}$	0.0008 (0.0001)	17.1	502 (34)	0.8209
satellite	0.0045 (0.0005)	17.0	205 (12)	0.9642

A lower Debye temperature for the satellite peak is more in line with the thermal Debye temperature associated with heat capacity [9], but in fact our value here is in agreement with a recent density functional theory (DFT) calculation using the LDA+U methodology [21] where a Debye temperature of 402.6 K for the ThO_2 fluorite structure was estimated. That is, the agreement with our measurement is closer to the calculated value than that obtained through the heat capacity measurement. Furthermore, the heat capacity measurement could be off by as much as $3^{1/3}$ according to physical arguments made within the heat capacity paper's text [9]. Our data tends to suggest that overall, for good single crystals, the Debye temperature is in fact significant.

The Th $4f$ core level binding energies and effective Debye temperature have been investigated using temperature dependent x-ray photoemission spectroscopy. Two Th $4f$ peaks are observed with binding energies that are in good agreement with the values expected for ThO_2 and accompanied by a satellite feature consistent with

a shake-up. The experimentally determined Debye temperature is 468 ± 32 K but is a value strongly weighted for thorium alone and neglects the possibility of the influence of a contamination layer crystalized on the surface. Nonetheless, the results determined experimentally here are in good agreement with the results of a recent DFT calculation (402.6 K) for the ThO_2 fluorite structure.

6.4.1 Acknowledgements.

This work was supported by the Defense Threat Reduction Agency (Grant No. HDTRA1-07-1-0008) and by the National Science Foundation (NSF) through Materials Research Science and Engineering Center (NSF Grant No. 0820521). The views expressed in this article are those of the authors and do not reflect the official policy or position of the Air Force, Department of Defense, or the U.S. Government.

References

[1] T. D. Kelly, J. C. Petrosky, J. W. McClory, T. W. Zens, D. Turner, J. M. Mann, J. W. Kolis, J. A. C. Santana, and P. A. Dowben, *MRS Online Proceedings Library*, p. 1576, 2013.

[2] M. Numakura, N. Sato, C. Bessada, Y. Okamoto, H. Akatsuka, A. Nezu, Y. Shimohara, K. Tajima, H. Kawano, T. Nakahagi, and H. Matsuura, *Prog. in Nuc. Energy*, vol. 53, p. 994, 2011.

[3] *IAEA-TECDOC-1450*. Vienna, Austria: International Atomic Energy Agency, 2005.

[4] D. LaGraffe, P. Dowben, and M. Onellion, *J. Vac. Sci. Technol.*, vol. A8, p. 2738, 1990.

[5] N. Wu, D. Wisbey, T. Komesu, Z. X. Yu, M. Manno, L. Wang, C. Leighton, , and P. A. Dowben, *Physics Letters A*, vol. 372, p. 2484, 2008.

[6] S. R. McHale, J. W. McClory, J. C. Petrosky, J. Wu, R. Palai, P. A. Dowben, and I. Ketsman, *Materials Letters*, vol. 65, p. 1476, 2011.

[7] C. N. Borca, B. Xu, T. Komesu, H.-K. Jeong, M. T. Liu, S. H. Liou, and P. A. Dowben, *Surface Science*, vol. 512, p. L346, 2002.

[8] S. Hüfner, *Photemission Spectroscopy: Principles and Application*, 3rd ed. New York: Springer, 2003.

[9] M. Ali and P. Nagels, *Phys. Stat. Sol.*, vol. 21, p. 113, 1967.

[10] M. Mann, D. Thompson, K. Serivalsatit, T. M. Tritt, J. Ballato, and J. Kolis, *Crystal Growth and Design*, vol. 10, no. 2146, 2010.

[11] M. Mann and J. Kolis, *Journal of Crystal Growth*, vol. 312, p. 461, 2010.

[12] J. C. Fuggle, A. F. Burr, L. M. Watson, D. J. Fabian, and W. Lang, *J. Phys. F: Metals Physics*, vol. 4, p. 335, 1974.

[13] W.-D. Schneider and C. Laubschat, *Phys. Rev. B*, vol. 23, p. 997, 1981.

[14] W. McLean, C. A. Colmenares, R. Smith, and G. A. Somorjai, *Phys. Rev. B*, vol. 25, p. 8, 1982.

[15] C.-S. Huang, M. Houalla, D. M. Hercules, C. L. Kibby, and L. Petrakis, *J. Phys. Chem.*, vol. 93, p. 4540, 1989.

[16] M. O. Krause, R. G. Haire, O. Keski-Rahkonen, and J. R. Peterson, *Journal of Electron Spectroscopy and Related Phenomenon*, vol. 47, p. 215, 1988.

[17] B. W. Veal, D. J. Lam, H. Diamond, and H. R. Hoekstra, *Phys. Rev. B*, vol. 15, p. 2929, 1976.

[18] G. C. Allen, S. Hubert, and E. Simoni, *J. Chem. Soc. Faraday Trans.*, vol. 91, p. 2767, 1995.

[19] W. P. Ellis, A. M. Boring, J. W. Allen, L. E. Cox, R. D. Cowan, B. B. Pate, A. J. Arko, and I. Lindau, *Solid State Commun*, vol. 72, p. 725, 1989.

[20] E. Ferrari, L. Galli, E. Miniussi, M. Morri, M. Panighel, M. Ricci, P. Lacovig, S. Lizzit, and A. Baraldi, *Phys. Rev. B*, vol. 82, p. 195420, 2010.

[21] P. Zhang, B. Wang, and X. Zhao, *Phys. Rev. B*, vol. 82, p. 144110, 2010.

VII. Conclusions

7.1 Summary of findings

Actinide single crystals are important to the fabrication of next generation electronic devices that could have useful radiation hardness properties and serve as efficient neutron detectors. However, obtaining single crystals is difficult due to the reactivity of the actinides with the atmosphere and other materials in contact, particularly C, O, and F. ThO_2 crystals are obtainable by the solar furnace method and by the skull melting technique, though these techniques do not easily lend themselves to controlled growth conditions, such as adding dopants and minimizing defects within the crystals during the growth process. However, hydrothermal synthesis has proven to allow controlled growth conditions [1, 2], growing single crystalline ThO_2 and even doped U:ThO_2 alloys.

As these crystals were the first of their kind, this dissertation focused on extracting their geometric and electronic structure. Not only do these results allow for further crystal growth to be pursued in an informed and purposeful direction, but they provide insight into the nature of ThO_2 in single crystalline form and the manner in which their properties differ when compared to the other forms found in literature (powders, colloids, pellets, etc).

From ultraviolet photoemission and inverse photoemission studies, the ThO_2 band gap is determined to be between 6.0-7.0 eV. This places it firmly into the insulator classification, agreeing with most measurements for ThO_2 found in the literature. Of particular interest is that deep band tailings (due to impurities and or point defects in the crystals) allow for band gap narrowing and result in a band gap of approximately 4.8 eV. Due to the growth technique used, this result offers promise of band gap engineering by controlling the mineralizer type and concentration, temperature,

and dopant presence during the hydrothermal growth process. Since ThO_2 already has applications in optics, such as an additive to lenses for controlling the index of refraction, being able to narrow the band gap could have further implications in other optics applications such as lasers [3].

The unoccupied DOS was confirmed to be of $5f/6d$ character, as expected. This was confirmed by x-ray absorption near edge structure, inverse photoemission spectroscopy, and real space Green's function calculations. However, it is also calculated that there is hybridization with the O $2p$ and O $2s$, an indication that the purely ionic model is not correct for ThO_2 and that the $5f$ electrons are not completely empty. In fact, the presence of a shake-up satellite confirms this result, where an f-f transition (keeping with monopole transition rules) would only be possible if there was initially $5f$ character in the valence band.

The long range order is found to be highly single crystalline from x-ray diffraction spectroscopy. However, from extended x-ray absorption fine structure spectroscopy, a split-O shell is observed which has not been found in literature for pure ThO_2. This split shell is interpreted as a mix of the fluorite unit cell and a defect unit cell with O vacancies and most likely anti-Frenkel point defects. These point defects are the shifting of an O anion from a lattice site, leaving a hole behind that serves as an electron trap and a donor site.

From x-ray photoemission spectroscopy, the surface and bulk characteristics are found to be very different, particularly in the presence of O, C, and H. Surface to core-level studies show a shift between the surface and the bulk. There are two novel shake-up satellite features in the spectra which have not been observed in ThO_2 before. Additionally, the quality of the crystals are good enough that these satellite features are able to be resolved between the bulk and surface. The bulk defects appear to be mostly due to point defects (and possibly impurities), while the surface states

are heavily influenced by the ambient environment.

From x-ray photoemission studies as a function of temperature, the Debye temperature has been measured. The surface Debye temperature is similar to that reported in the literature for non-single crystal ThO_2. The soft surface is most likely due to C and H which bound to the surface when exposed to the air. However, in the bulk, the crystal is found to be very rigid. This rigidity implies an innate radiation hardness and a more covalent bonding character as predicted from the x-ray absorption near edge structure and FEFF calculations.

7.2 Future Work

As this research was fundamental and foundational, there are many experiments which could be conducted to further the work. Many of the experiments which are a natural extension of this work involve parameterizing the measurements made here as a function of U doping in U:ThO_2 crystals. For example, the band gap could be measured as a function of $U_xTh_{1-x}O_2$ for variable x concentrations. It is expected that a functional form could be fit and derived moving from the 6-7 eV band gap of ThO_2 toward the 2-3 eV band gap of UO_2. This could also be done for the work function of the materials V_ϕ. Both of these parameters are essential for future device fabrications and these experiments would offer tremendous insight into the manner in which to proceed in constructing a neutron detector from UO_2 semiconductors.

The ThO_2 crystals were found to be n-type. Further investigation into the transport mechanisms could be made through Hall measurements. Measuring the Hall voltage can provide insight into the charge carrier types and concentrations from (64) where I is the current due to the applied voltage, B is the magnetic field along the sample surface, T is the sample thickness, q is the electronic charge, V_h is the Hall

voltage, and A is the sample surface area [4, 5].

$$n = -\frac{IBT}{qV_hA} \tag{64}$$

Much of the surface work measured by x-ray photoemission, ultraviolet photoemission, and inverse photoemission spectroscopies could be repeated with a system that allows for sputtering. In this research, no chamber or system was available at AFIT where this was possible. Due to concerns of contaminating chambers at other institutions, the sputtering routines were not used at those facilities. In this research, the influence of the atmospheric environment, particularly C and O, upon the measured electronic properties was addressed. The satellite peaks in the x-ray photoemission demonstrated a clear dependence between the surface and bulk environments. By sputtering, the precise nature of the satellite peaks may be extracted. If sputtering caused the lowest energy satellite at 348.1 eV to diminish or disappear, then it could be attributed to the O-H and C-H contamination bonds on the sample surface.

If sputtering was also combined with resonant photoemission studies, the results of this dissertation work could be expounded upon. Some resonant photoemission work has been done previously using the $5d$ core levels, however none could be found for the $4f$ core levels. Through resonant photoemission, the nature of the satellite features, particularly at 350.8 and 352.8 could be further investigated. Currently, this dissertation work interprets these peaks to be transitions due to the band gap and a narrowed gap due to impurity states. Additionally, resonant photoemission studies could further aid interpreting the degree of $5f$ and $6d$ hybridization within the single crystals.

A parameter study could be conducted by changing the growth conditions which produce the single crystals. By growing crystals at various pressures and tempera-

tures, different intrinsic defects could be grown into the crystals. By studying the band gap and the local geometric structure with x-ray absorption fine structure, the defects could be analyzed based upon the growth conditions. A more complicated study would combine this with the variable doping of U into the ThO_2 crystals.

Of course, these measurements and those mentioned previously could also be conducted for single crystals grown in a variety of orientations. The crystal orientation could be selected through appropriate choices of seed crystals which already have the orientations desired. This would also allow for band mapping at a synchrotron using angular resolved photoemission spectroscopy. As the literature reports both indirect and direct band gaps for ThO_2, band mapping in various orientations could also elucidate which type of band gap is the most appropriate description.

Lastly, the desired outcome of this work is ultimately the fabrication of U_xO_y semiconductors and neutron detectors. Studies on the device feasibility and crystal response to neutron radiation should be conducted at a fundamental level. Many of the measurements in this research should be repeated after the crystals are exposed to various neutron fluxes. This would not only provide insight into device aging, but it would allow for a study of the conduction mechanisms that dominate as a function of radiation fluence.

References

[1] M. Mann, D. Thompson, K. Serivalsatit, T. M. Tritt, J. Ballato, and J. Kolis, *Crystal Growth and Design*, vol. 10, no. 2146, 2010.

[2] M. Mann and J. Kolis, *Journal of Crystal Growth*, vol. 312, p. 416, 2010.

[3] P. V. Mieghem, *Reviews of Modern Physics*, vol. 64, p. 755, 1980.

[4] S. M. Sze, *Semiconductor Devices*, 2nd ed. John Wiley and Sons, 2002.

[5] N. Ashcroft and N. Mermin, *Solid State Physics*. Brooks Cole, 1976.

Appendix A. Extracting EXAFS from XAFS signals

The traditional procedure is demonstrated using Cu XAFS data as a procedural example. From the beamline, the data is normally provided in one of two formats: (1) photon counts as a function of monochromator angle or (2) photon counts as a function of photon energy. If the data is provided as the former, then the Bragg condition is used to convert the data into photon counts as a function of energy.

Using the Beer-Lambert's Law, the absorption coefficient is determined by taking the ratio of the transmitted, fluorescent, or electron yield to the initial reference counts. The Cu foil absorption coefficient is plotted in Figure 43. In the figure, there is a transmission of the synchrotron photons until the energy reaches the Cu K-edge ($\approx$ 8981 eV [1]). At the photoelectric edge, the electrons in the innermost orbital may be promoted to the continuum and any excess energy from the initial photon goes into the kinetic energy of the photoelectron. This is the same theory underlying the photoemission process from Chapter 2.

After the rising edge, a series of oscillations compose the x-ray absorption fine structure. These oscillations are isolated by subtracting the smoothly varying background due to the free atom absorption. The procedure is shown for the Cu data in Figure 44. First, a pre-edge line (green line) is fit to the data before the absorption edge. The pre-edge is fit with either a linear function or the Victoreen equation. This pre-edge line is extrapolated beyond the absorption edge into the higher energy regime.

The EXAFS structure is a modulation of the bare atom absorption (65), where $\mu(E)$ is the observed absorption spectrum, μ_0 represents the bare atom absorption, and $\chi(E)$ are the EXAFS oscillations. Rearranging Equation 65 to obtain $\chi(E)$ demonstrates that the EXAFS may be obtained from the data by subtracting out the bare atom (or background) absorption and normalizing.

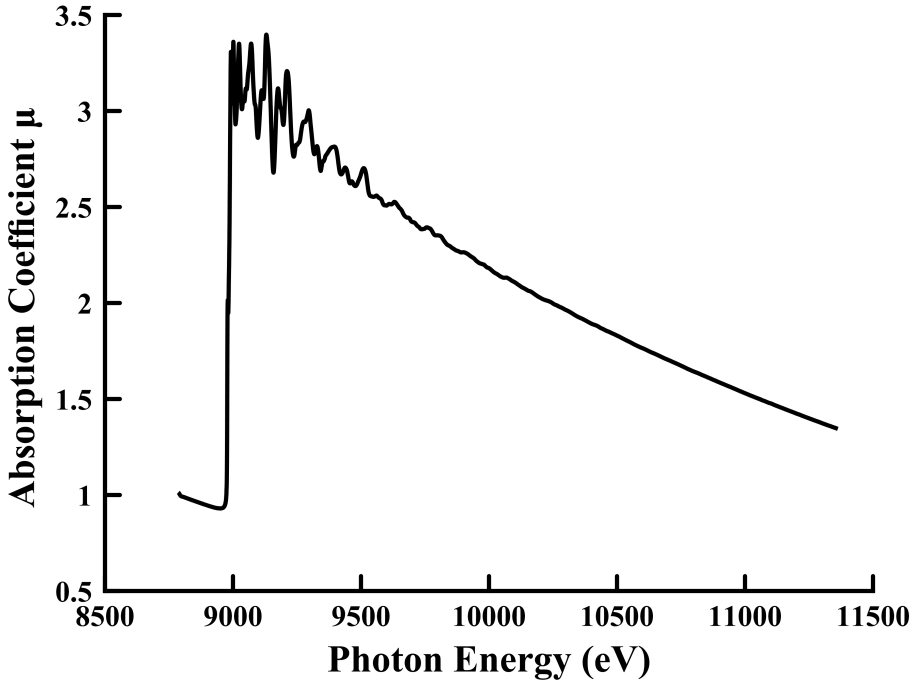

Figure 43. Experimental data for 99.999% Cu metal taken at 10 K. Data available at [2].

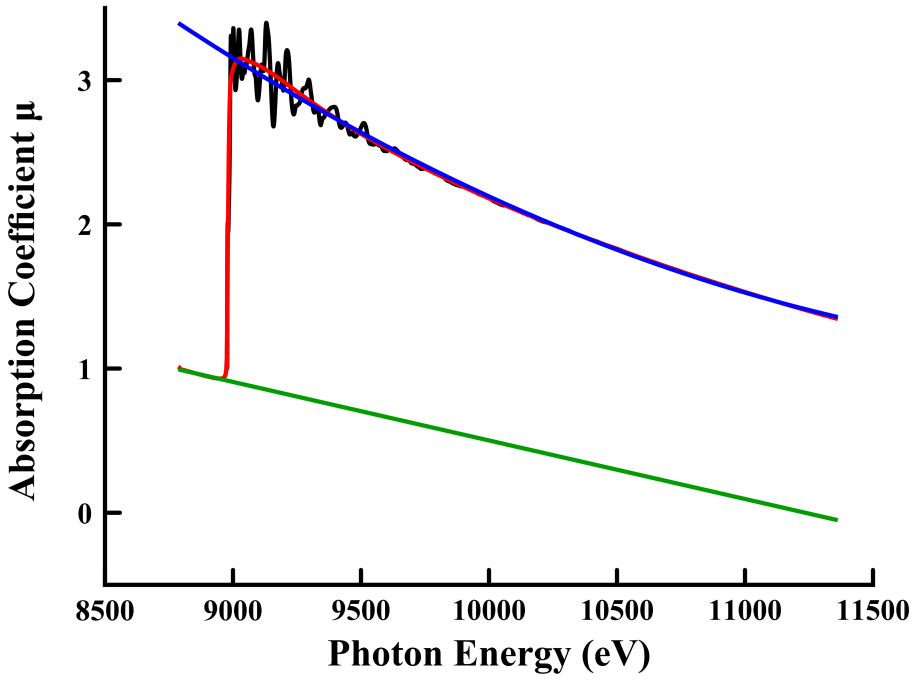

Figure 44. Isolating the EXAFS oscillations by subtracting out a smooth background function.

$$\mu(E) = \mu_0 \left[1 + \chi(E)\right] \tag{65}$$

In Figure 44, the background absorption is given by a red line. This background absorption may be obtained via several methods. One method uses experimental data. The data are smoothed many hundreds of times by considering 5-20 neighboring points at a time. The resulting smoothed spectra is then assumed to be a representation of the bare atom absorption background. However this method will be faulty if there are large, visible oscillations.

In the second method, the background is represented by a cubic polynomial fit to the post-edge region (blue line in Figure 44). The cubic polynomial is extrapolated through the energy origin E_o (discussed in the next paragraph) and into the pre-edge. This second method is used in this research, as the cubic spline prevents large oscillations from unequally weighting the background. The cubic spline is implemented by choosing equidistant spline knots across the post-edge region.

Ideally, the absorption edge would be vertical, and the photoelectric edge would be a delta function at the absorption threshold. However, experimental convolution and lifetime broadening result in a width to the photoelectric edge as in Figure 43. Thus, determining the photoelectric origin ambiguous. It is customary to take the derivative of the rising edge and use the inflection point as an estimate of the origin, as is done for the Cu data in Figure 45. Since the photoelectric origin was chosen arbitrarily, this origin is a free parameter in the fitting routines (labeled as E_o). With E_o estimated, the absorption spectrum is converted from energy to wave vector (k-space).

After removing the background and converting to k-space, the EXAFS oscillations are isolated. In Figure 46, two versions of the extracted Cu data are shown. In the

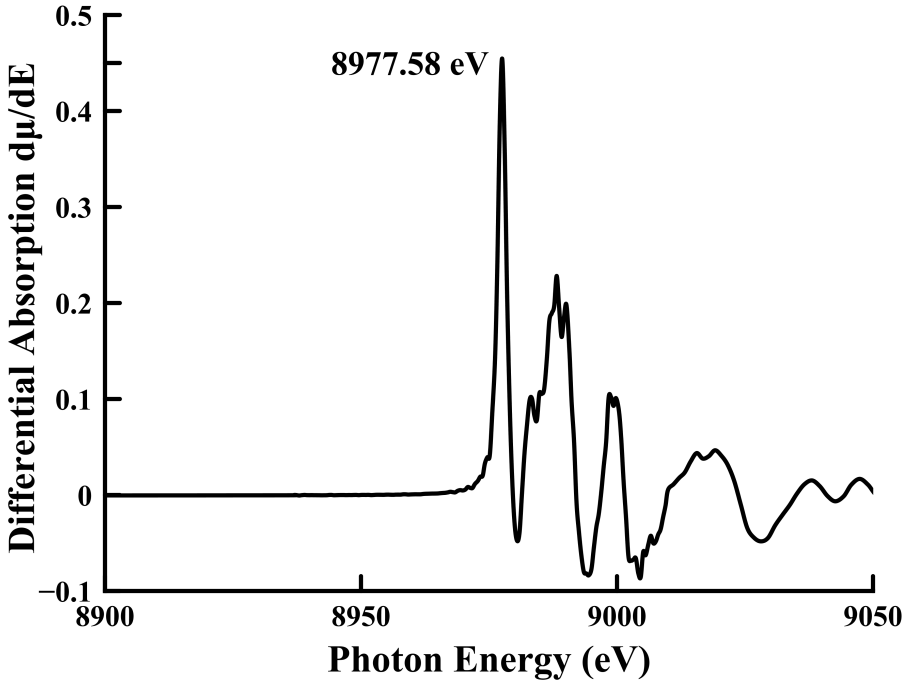

Figure 45. Using the inflection point along the rising edge to make an educated guess of the energy origin.

top panel, the raw experimental EXAFS signal is plotted. In order to emphasize the influence of low Z and high Z atoms (e.g. O versus Th), study the influence of distorted structures versus undistorted (e.g. amorphous or Jahn-Teller), and minimize the influence of the ambiguity in choosing E_0, the EXAFS signal is weighted by k^n with n = 1, 2, or 3. A linear k-weight is shown in the bottom panel of Figure 46.

The extracted EXAFS signal is Fourier transformed and checked for spurious peaks, usually below 1.0 Å. In Figure 47, the k-weighted Fourier transform has been made with both a good and bad background subtraction. A bad background subtraction results from choosing an E_0 value of of the photoelectric edge, having the interpolation follow the EXAFS oscillations instead of extrapolating smoothly through the oscillations, and failing to smoothly connect the spline to the pre-edge.

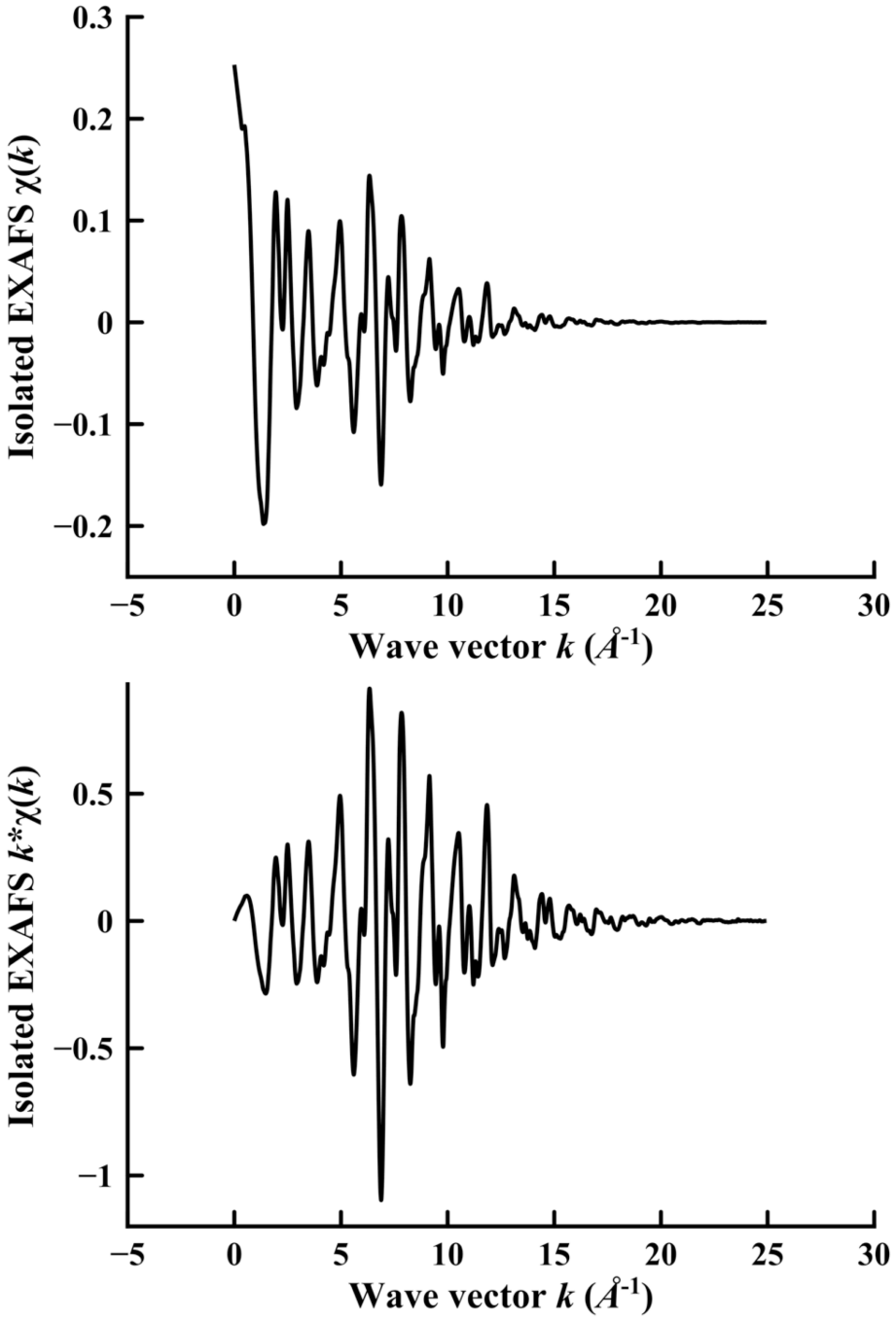

Figure 46. The top panel is the extracted Cu EXAFS signal. The bottom panel is the k-weighted EXAFS.

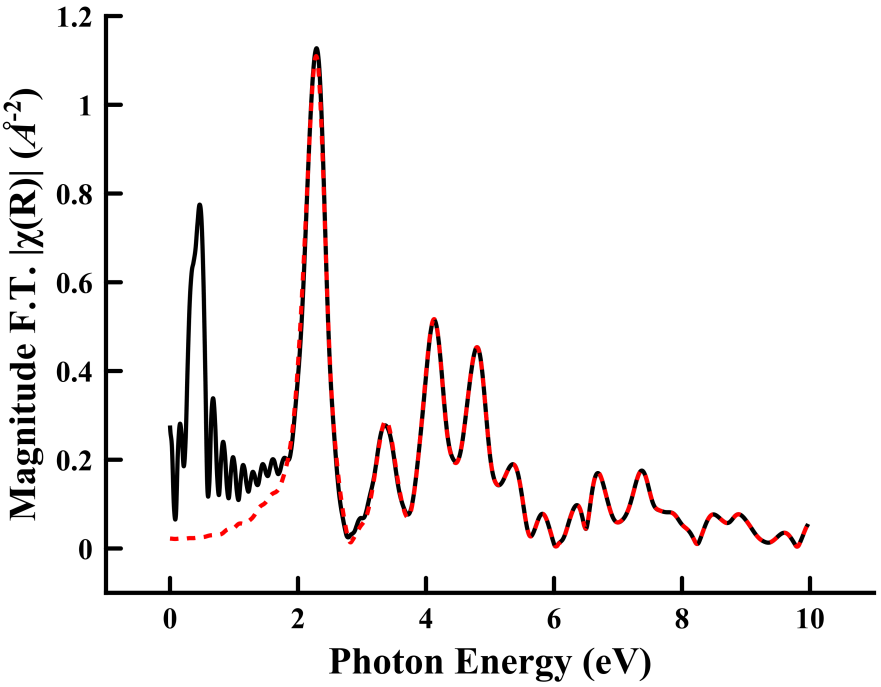

Figure 47. A bad background subtraction (solid black) and a good background subtraction (dotted red) for k-weighted Fourier transformed EXAFS.

Appendix B. Charge transfer shake-up satellite in CuO

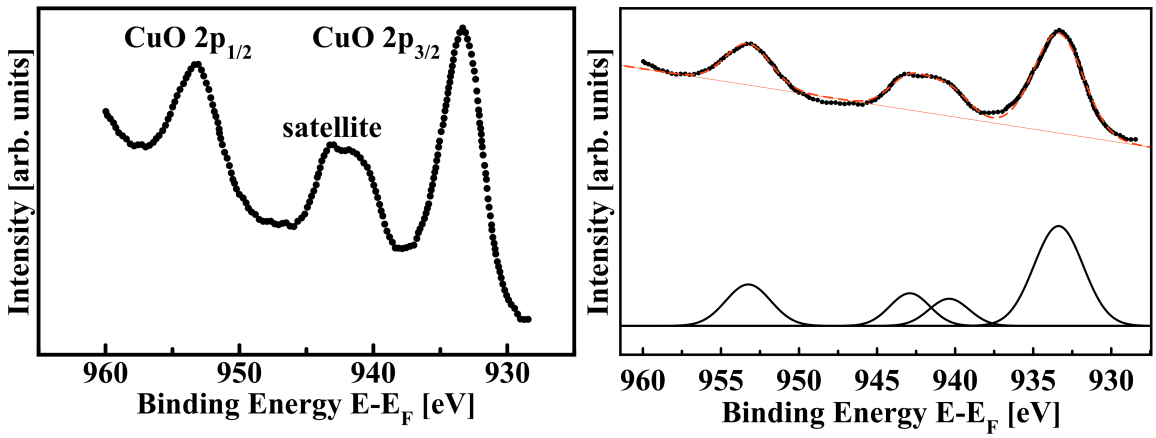

Figure 48. CuO data extracted and plotted from [3] in order to demonstrate the shake-up satellite effect. The right subfigure shows the peaks fit with Gaussians and a linear background.

In Figure 48, CuO data has been obtained by Mg-Kα XPS [3]. The copper peaks have been labeled for the Cu $2p$ emission. Both initial and final state effects are present. The initial state effect results in two peaks, one at $2p_{3/2}$ and the other $2p_{1/2}$. This doublet is due spin-orbit splitting. The total angular momentum quantum number associated with the peak is given by (66). Given that electrons are fermions with spin 1/2, then for the angular momentum quantum number $L = p = 1$, the total angular momenta for the electron bound in the Cu $2p$ orbital is $J = 3/2$ and $J = 1/2$. The degeneracies for each orbital are calculated from 67. The peak areas should have a ratio close to $\mathrm{D}(2\mathrm{p}_{1/2})$ / $\mathrm{D}(2\mathrm{p}_{3/2}) = 2$ / $4 = 1/2$.

$$J = L \pm S \tag{66}$$

$$D = 2J + 1 \tag{67}$$

The final state effects result in the presence of satellite peaks in addition to the main peaks. The final states result because photoelectron spectroscopy is a final

state measurement. The ground state for the photoelectric process is (photon+bound electron) while the excited state is (core-hole+photoelectron). If there is more than one way for the excited state to occur, then satellite peaks will appear. In this case, the CuO peaks exhibit shake-up satellites. The ground state of CuO has Cu in the +2 charge state and the electronic configuration $2p^6 3d^9$. The ligand is an O atom with the configuration $2p^6$. The Cu core electrons will be represented by c and the ligand electrons by L, so that the total configuration is written $c3d^9L$ as in Hüfner's discussion on Cu halides [4].

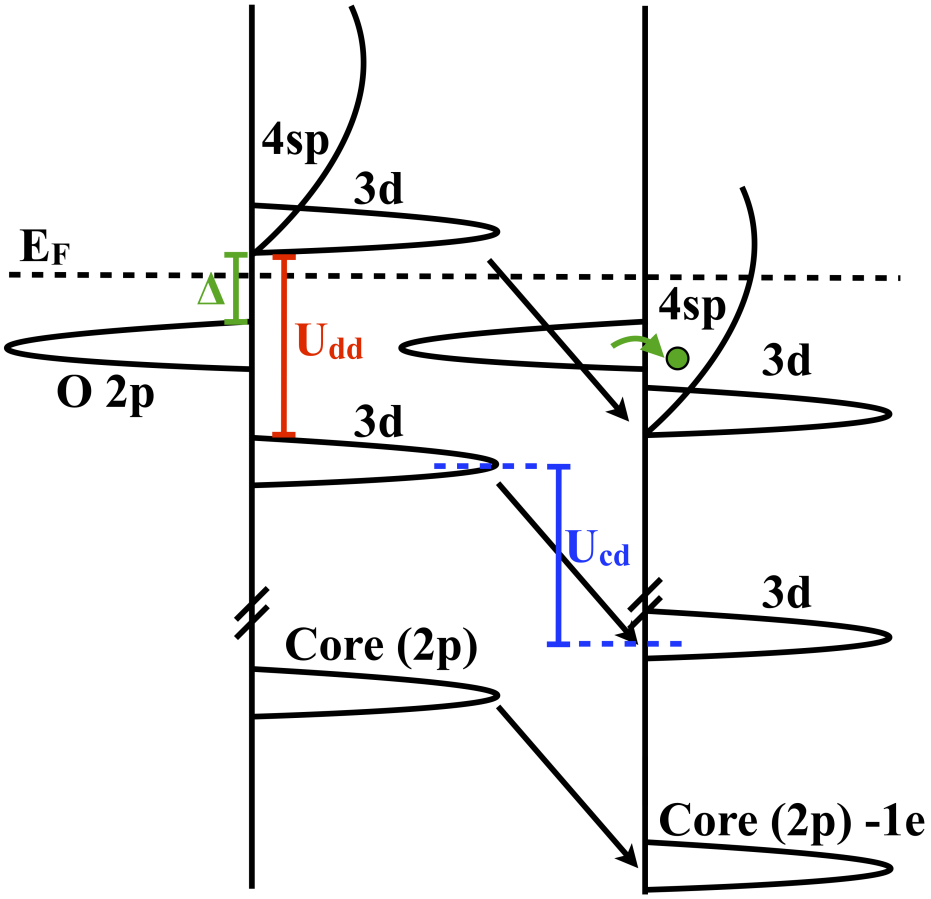

Figure 49. Final state of CuO with core-hole and $4sp$ band filled with electron from O $2p$.

Following a similar schematic and procedure in [4, 5], in Figure 49 the energy

difference between the ligand and the bottom of the unoccupied 3d orbital, Δ, is 4 eV. The gap between the occupied and unoccupied Cu $3d$ states is given by U_{dd}. After absorbing a photon and emitting a photoelectron, there is a core-hole which causes the electrons to shift down in energy as they are now less screened from the positive nucleus of the Cu atom. This causes the Cu $4sp$ band to overlap with the O $2p$ and an electron transfers from the ligand to the metal ion. The final state configuration is then $c^{-1}3d^9L$. However, instead of transferring to the delocalized $4sp$ band, the ligand could also transfer an electron to the nearby empty $3d$ band. This results then in the configuration $c^{-1}3d^{10}L^{-1}$. The main peak corresponds to the configuration $c^{-1}3d^{10}L^{-1}$ (the total electrons on Cu are back to 9), whereas the satellite peak is $c^{-1}3d^9L$. The gap U_{dd} is approximately 7 eV, the difference between the main peak and satellite peak shown in Figure 48. The result of the physics described is that the shake-up satellite is effectively separated from the main peak by the quanta of energy necessary to promote a valence electron into an unoccupied state and removing that energy from the kinetic energy available to the emitted photoelectron.

References

[1] J. H. Hubbell and S. M. Seltzer, "Tables of X-Ray Mass Attenuation Coefficients and Mass Energy-Absorption Coeofficients from 1 keV to 20 MeV for Elements Z = 1 to 92 and 48 Additional Substances of Dosimetric Interest," *Radiation Research*, vol. 136, p. 147, 1993.

[2] [Online]. Available: http://cars9.uchicago.edu/~ravel/course/exercises.html

[3] Q. Liu, H. Liu, Y. Liang, Z. Xu, and G. Yin, "Large-scale synthesis of single-crystalline CuO nanoplelets by a hydrothermal process," *Materials Research Bulletin*, vol. 41, p. 697, 2006.

[4] S. Hüfner, *Photemission Spectroscopy: Principles and Application*, 3rd ed. New York: Springer, 2003.

[5] P. van der Heide, *X-ray Photoelectron Spectroscopy: An Introduction to Principles and Practices*. Boboken: John Wiley and Sons, 2012.

REPORT DOCUMENTATION PAGE

Form Approved
OMB No. 0704-0188

PLEASE DO NOT RETURN YOUR FORM TO THE ABOVE ORGANIZATION.

1. REPORT DATE *(DD-MM-YYYY)*	2. REPORT TYPE	3. DATES COVERED *(From - To)*
26-12-2013	Doctoral Dissertation	September 2010-December 2013

4. TITLE AND SUBTITLE
Electronic and Physical Characterization of Hydrothermally Grown Single Crystal ThO2

5a. CONTRACT NUMBER

5b. GRANT NUMBER
See Block #13

5c. PROGRAM ELEMENT NUMBER

6. AUTHOR(S)
Kelly II, Tony D.

5d. PROJECT NUMBER

5e. TASK NUMBER

5f. WORK UNIT NUMBER

7. PERFORMING ORGANIZATION NAME(S) AND ADDRESS(ES)
Air Force Institute of Technology
Graduate School of Engineering and Management (AFIT/EN)
2950 Hobson Way
WPAFB OH 45433-7765

8. PERFORMING ORGANIZATION REPORT NUMBER
AFIT-ENP-DS-13-D-02

9. SPONSORING/MONITORING AGENCY NAME(S) AND ADDRESS(ES)
Basic and Applied Sciences
Defense Threat Reduction Agency
8725 John J Kingman Rd Stop 6201
Fort Belvoir VA 22060-6201

10. SPONSOR/MONITOR'S ACRONYM(S)
DTRA

11. SPONSOR/MONITOR'S REPORT NUMBER(S)

12. DISTRIBUTION/AVAILABILITY STATEMENT
Approved for public release; distribution unlimited

13. SUPPLEMENTARY NOTES
DTRA Grant# 11-2884M and HDTRA124030
Department of Homeland security Grant# HSHQDC-08-X-00641/P00001

14. ABSTRACT
Actinide single crystals are important to the fabrication of next generation electronic devices that could possibly have radiation hardness properties and serve as efficient neutron detectors. However, obtaining single crystals is difficult due to the reactivity of the actinides with the atmosphere and surroundings. ThO2 single crystals were obtained previous to this work by hydrothermal synthesis. As these crystals were the first of their kind, the geometric and electric structure of the crystals needed to be extracted. The valence and conduction bands were studied in order to ascertain the band gap using ultraviolet photoemission spectroscopy (UPS) and inverse photoemission spectroscopy (IPES). The unoccupied structure was further characterized using x-ray absorption near edge structure (XANES) and relativistic, real-space Green's functions calculations. The local structure around the Th atoms was investigated using extended x-ray absorption fine structure (EXAFS). A novel Latin hypercube sampling code was developed to extract the local order structure. X-ray photoemission spectroscopy (XPS) was used to measure a surface-to-bulk level shift and extract two new shake-up satellite structures in the 4f region. A temperature dependent XPS study extracted the Debye coefficients.

15. SUBJECT TERMS
thorium dioxide, ultraviolet photoemission spectroscopy, inverse photoemission spectroscopy, x-ray absorption near edge structure, extended x-ray absorption fine structure, nuclear materials

16. SECURITY CLASSIFICATION OF:			17. LIMITATION OF ABSTRACT	18. NUMBER OF PAGES	19a. NAME OF RESPONSIBLE PERSON
a. REPORT	b. ABSTRACT	c. THIS PAGE			James C. Petrosky, PhD, (ENP)
					19b. TELEPHONE NUMBER *(Include area code)*
U	U	U	UU	145	(937) 255-3636 ext 7300 james.petrosky@afit.edu

Reset